Università degli Studi di Udine
Dottorato di Ricerca in
Scienze dell'Ingegneria Energetica e Ambientale
XXXIII Ciclo

Particle Capture and Pattern Evolution on Big Drops in Three-phase Turbulence

Arash Hajisharifi

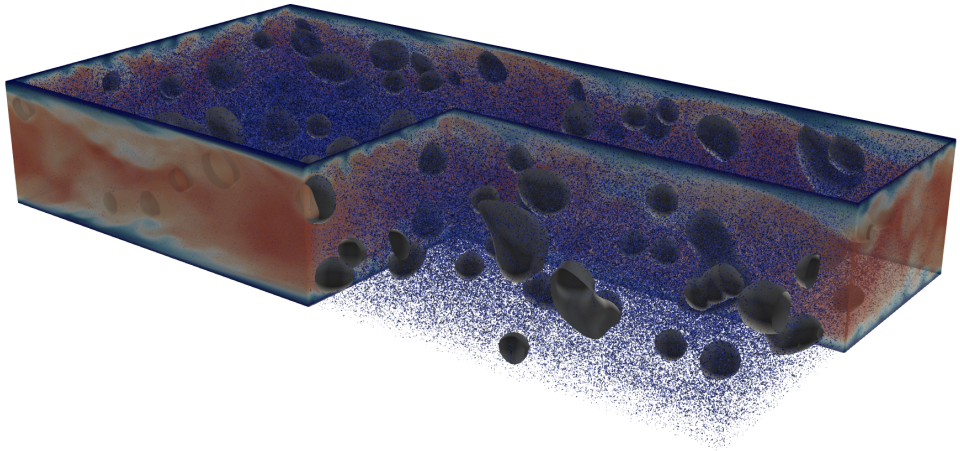

BOARD MEMBERS

Prof. Mauro Chinappi	Reviewer
Dr. Gregory Lecrivain	Reviewer
Prof. Chiara Galletti	Committee member
Prof. Stefania Scarsoglio	Committee member
Dr. Francesco Zonta	Committee member
Prof. Alfredo Soldati	Supervisor
Prof. Cristian Marchioli	Co-Supervisor
Prof. Alessandro Trovarelli	Doctorate Chair

Author's e-mail:
hajisharifi.arash@spes.uniud.it

Author's address:
Dipartimento Politecnico di Ingegneria e Architettura
Università degli Studi di Udine
Via delle Scienze 206
33100 Udine, Italy

Cover:
Instantaneous representation of the three-phase turbulent flow at $t^+ = 1500$. The carrier phase outside the droplets is rendered via fluid streaklines.

This thesis is dedicated to the memory of my father who never saw this adventure but initially encouraged me to start it and to the memory of my late mother, to someone who has always been for me and supported me during these years but could not see the end.

Acknowledgements

I would like to thank my PhD supervisors, Professor Alfredo Soldati, for giving me the opportunity to join his group and work on such an interesting topic and for all of his help and advice with this PhD. I am extremely grateful to Professor Cristian Marchioli, my PhD co-supervisor, for his invaluable advice, continuous support, and patience during my study. His knowledge, experience and overall insights in this field have helped me in all the time of research.
A special thank goes to the reviewers of my thesis, Professor Mauro Chinappi, Dr. Gregory Lecrivain for careful review of the thesis; their insightful observations, suggestions and feedback have been greatly appreciated. I would like to also thank committee members, Professor Chiara Galletti, Professor Stefania Scarsoglio and specially Dr. Francesco Zonta who supported me during my stay in Vienna.
Some special words of gratitude go to all of my friends and colleagues from the University of Udine and from the Institute of Fluid Mechanics and Heat Transfer at the TU Wien, Nicola, Michele, Davide and in particular Alessio and Giovanni for the useful discussions and guidance. Special thanks go to Mobin and Pejman who have always been a major source of support when things would get a bit discouraging and for their friendship.
Finally, I want to express my very profound gratitude to my wonderful family. Thanks for continuous encouragement and supports through the ups and downs of my academic career. Mom and Dad, you were wonderful parents. I miss you every day, but I am glad to know you saw this process through to its completion. My sisters, I could not ask for a better sisters and friends. The least I can do is thank you for being such a wonderful sister to me for as long as I can remember. My fiancée, thank you for your endless love and support in every step of my thesis and for showing me the beauty and opposite site of life and making my mind relax during the hard times. This accomplishment would not have been possible without you. I am forever grateful of having all of you, this dissertation stands as a testament to your unconditional love and encouragement.

Abstract

The process of particle capture and trapping by large deformable drops in turbulent channel flow are investigated in this thesis using an Eulerian-Lagrangian approach specifically developed for this three-phase flow. The Navier-Stokes equations are solved and the flow is simulated in the carrier fluid and inside the droplets; the drop interface dynamics are provided by a Phase Field Model and particle trajectories are calculated via Lagrangian tracking. Drops have the same density and viscosity of the carrier fluid in order to mimic a liquid-liquid dispersion of water and low-viscosity oil. Particles are modelled as neutrally-buoyant, sub-Kolmogorov spheres that interact with one another through collisions (excluded-volume interaction). Simulation results allow a detailed characterization of the particle dynamics during the interface capture and trapping stages. Particle capture is driven by the capillary forces of the interface in combination with near-interface turbulent motions: Particles are transported towards the interface by jet-like turbulent motions and, once close enough, are captured by interfacial forces in source of velocity regions (positive surface velocity divergence). These regions appear to be well correlated with high-enstrophy flow topologies that contribute to enstrophy production via vortex compression or stretching. Upon capture, particles sample preferentially regions of positive surface velocity divergence, which correlate with jet-like fluid motions directed towards the interface. At later times, however, particles are observed to move from these regions under the action of the tangential stresses to the areas where the surface divergence vanishes and form the two-dimensional cluster. Long-term trapping regions correlate well with the surface area characterized by higher-than-mean curvature.
This finding is important since the presence of tiny particles at the interface is known to affect locally the surface tension, particularly in the presence of concentration gradients: present results suggest that particle-induced modifications of the surface tension should be stronger where the curvature of the interface is higher.

Contents

1

Introduction

The process of particle capture and subsequent trapping by drops or bubbles in a turbulent flow is of relevance in a number of industrial applications requiring particulate abatement, e.g. via wet scrubbing [64, 100, 90], froth flotation [94, 143, 93] and emulsion Stabilization [21, 133, 56, 53]. The last three processes will be briefly explained below.
The very same process is also observed in environmental problems, such as accidental oil spills in which oil interacts with sediments to form oil-particle aggregates that may affect the transport of spilled oil and enhance oil biodegradation [155]. In these applications, particle capture occurs in two steps: First, particles move towards the drop/bubble surface under the influence of turbulence in the carrier liquid, possibly aided by external forces as in the case of electrostatic scrubbing [31, 132]; then particles stick the drop/bubble surface upon inertial impaction or turbulent diffusion. Particle behaviour upon impaction determines the overall attachment efficiency, which in turn affects the overall capture efficiency of the drop/bubble. In this context, a crucial physical property is surface tension, which controls drop/bubble deformability, drives particle adhesion and leads to the formation of a layer that may change the mechanical and mass transport properties of the interface [37, 33, 131].

Wet scrubbing

Wet scrubbing is an effective process to remove small particles from gaseous streams which is done in wet scrubbers. The scrubber brings particle-laden gas into contact with liquid droplets in which the small dust particles, produced from combustion or a chemical reaction will have very small size (less than 5 micrometres), are captured by wet scrubber's large liquid droplets (in the range of 150 to 500 micrometers). The operation mechanism of wet scrubbers is as follows; Scrubbing liquid (droplet) is introduced into the scrubber as a spray directed down. As the liquid drains through the vanes, it creates curtains of scrubbing liquid Fig. 1.1. Dust laden gas enters the scrubber tangentially and collides with the curtains initiating particle agglomeration. The coarser particles produced are washed down to the slurry outlet. The coarser droplets impinge on the mist eliminator vanes and the finer droplets are forced to drop out of suspension by gravitational and centrifugal forces acting on the gas stream as it exits through the top.
Droplets used in scrubbers collect particles using several collection mechanisms such

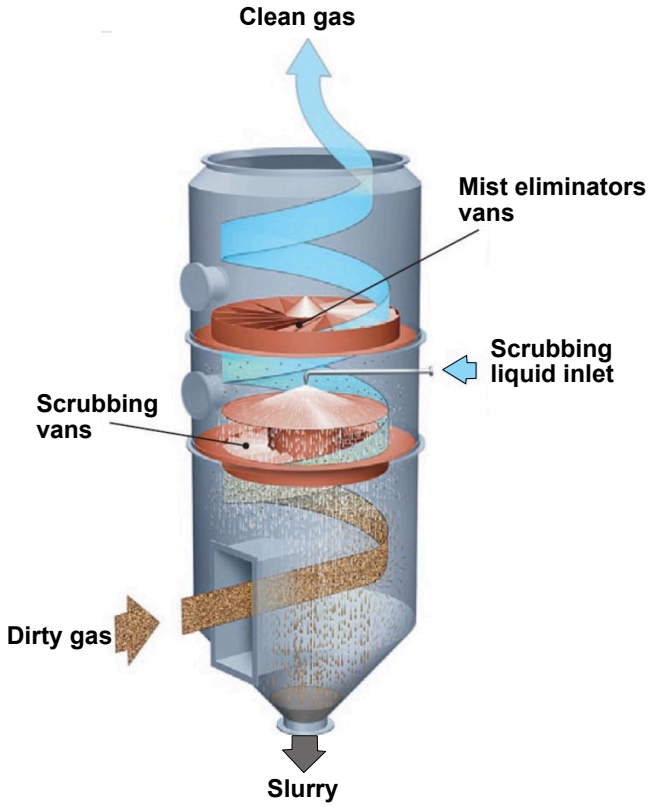

FIGURE 1.1 – Schematic of a gravitational wet scrubber [1]. As the particle-laden gas (Dirty gas) flows upward, particles collide with liquid droplets sprayed across the flow passage, and then liquid droplets containing the particles settle to the bottom of the scrubber as slurry.

as impaction, direct interception, diffusion, electrostatic attraction, condensation, centrifugal force and gravity among which the impaction and diffusion are the main ones.

Impaction is a very effective mean of capture for particle larger than 0.5 microns and diffusion is the primary capture mechanism for the very small particle in less than 0.1 micron range In the 0.1 to 0.5 micron range, both collection mechanisms can be active, but neither is especially effective.

Impaction occurs as a particle laden gas stream flows around an obstacle, droplet, and the particles follow a trajectory and collide with the droplet due to their inertia Fig. 1.2(a). This mechanism depends on the particle diameter and the relative velocity of particle and droplet; It increases as the particle diameter and relative velocity increase. The faster particles move, the higher the chance to hit the droplet and being captured. The droplet size is also important in this mechanism, the bigger the droplets the higher the probability that particles impact on them.

In diffusion, the particles are very tiny and they bumped by the gas Fig. 1.2(b). The

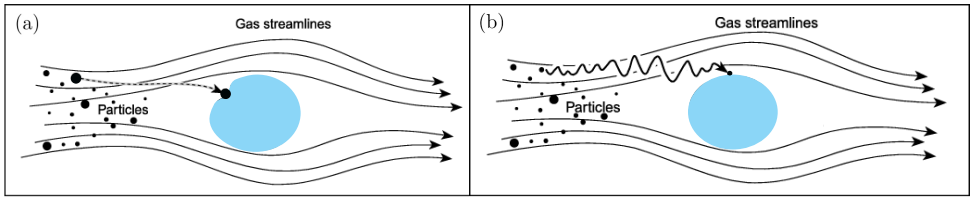

FIGURE 1.2 – Schematic of collection mechanism in wet scrubbers. panel (a) shows the impaction mechanism and the diffusion is shown in panel (b). Diffusion is used to remove the very tiny particles whereas impaction is mire efficient to caprure particles larger than 0.5 microns.

random movements due to these collisions cause the particles get close enough to the drops by which they are captured. The efficiency of this process can be increased by decreasing the particle size and increasing the gas temperature; increasing the gas temperature will increase the kinetic energy of gas molecules striking the small particles.
Scrubbing systems require very high particulate removal efficiency to be installed; Flux force/condensation conditions is used to aid the capture.

Froth flotation

Froth flotation is one the separation method that selectively separates particles based on their hydrophobicity or hydrophilicity of the material; used in mineral processing and water treatment industries. In this process froth stability plays a major role in flotation performance. The development of froth flotation has improved the recovery of valuable minerals, such as copper and lead-bearing minerals. The advantage of this process is that most of the minerals can be separated by this process. [17, 88, 152]. Then, the surface properties can be controlled and altered by the flotation reagent. Finally, this technique is highly appropriate for the separation of sulfide minerals. In the froth flotation process, the air bubble adhere to the particle due to their hydrophobicity nature. The particle and bubbles move toward the surface where a froth is then formed. This froth can be then removed from the surface. In this way, the hydrophilic materials are separated and remain in the liquid.
The process of froth flotation usually involves the following steps; the preparation of appropriate particle sizes of liberated components in the mixture of solids to be separated. Then, a proper condition that favor the adhesion of one or more components in the mixture of solids to the bubbles is needed to be created. The formation of a stable froth containing one or more components existing on the surface of the agitated mixture of particles (the pulp) which can be removed (recovered) would be the last step [24].

Emulsion Stabilization

An emulsion is a mixture of two or more liquids that are immiscible. it is generally either water-in-oil (w/o) or oil-in-water (o/w) emulsions. In the former water droplets are dispersed in the oil whereas the oil droplets are dispersed in an aqueous phase in the

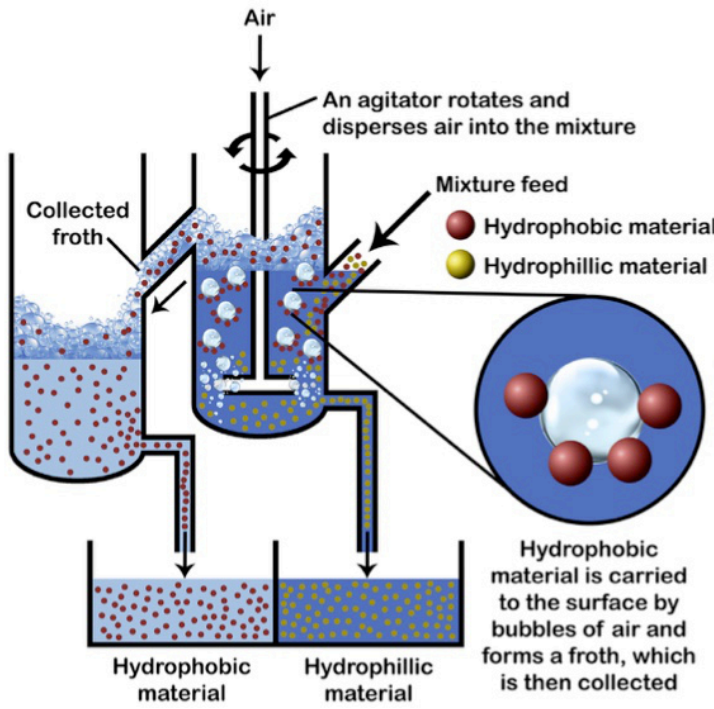

FIGURE 1.3 – The process of froth flotation. In this process the particles can be separated from the liquid phase due to the selective adhesion of air bubble to the particle surface based upon their hydrophobicity. The hydrophobic particles with the air bubbles attached are carried to the surface, thereby forming a froth which can be removed, while hydrophilic materials stay in the liquid phase [24].

latter; that is the target of this study. The droplets in an emulsion are referred to as the dispersed phase, while the surrounding liquid is referred to as the continuous phase [72, 138, 21]. Conventional oil-in-water or water-in-oil emulsion-based products are broadly used in our daily lives including milk, mayonnaise, salad dressings, cosmetic and pharmaceutical lotions, creams [117].

The Emulsions are thermodynamically unstable and tend to separate in a water and an oil phase during storage through a variety of instability mechanisms. These mechanism can be classified into four categories: Gravitational separation, droplet aggregation , Ostwald ripening, and droplet coalescence [72, 71]. All these instability mechanisms lead to droplet coalescence. It forms a larger layer of disperesed phase inside the continuous phase and leading, eventually, to the formation of separate oil and water phases.

Different compounds present at the oil–water interface can delay this coalescence at the oil–water interface; these materials which are so-called emulsifier used to stabilize emulsions. The emulsifiers increase the kinetic stability forming a more stable emulsion.

In these cases, different compounds, which are so-called emulsifiers, that are capable of

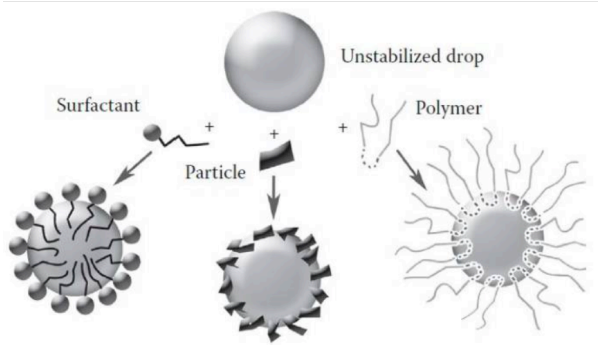

FIGURE 1.4 – Emulsion stabilization using surfactants, particles and polymers.as emulsifier to reduce the surface tension. They form stabilizing layer on the drop interface to prevent droplet coalescence and to attain reasonable stability [113].

adsorbing at the oil–water interface and protecting emulsion droplets from aggregation or coalescence are used. Emulsifiers, that could be the high molecular weight polymers, colloidal particles and surfactants Fig. 1.4, rapidly adsorb at the oil–water interface and significantly reduce the interfacial tension in order to facilitate drop brake-up [34]; increase the kinetic stability leading to form a more stable emulsion.
Solid particles can also used to stabilize the emulsion forming so-called Pickering emulsions. Surface wettability of particulate material used for Pickering emulsion describe their amphiphilicity which is measured by the three-phase contact angle of particles adsorbed at an oil–water interface. Irreversible adsorption of particles at the interfaces form an effective mechanical barrier against coalescence and stabilize the Pickering emulsions [146] .

Motivation

In all the mentioned applications, Particle capture and subsequent distribution on the interfaces of complex morphology are aspects of a multi-faceted multiphase flow problem, which must be investigated with a stepwise approach in order to unravel the physical mechanisms involved. Aim of this study is to elucidate the mechanisms that govern particle capture at the surface of a swarm of deformable drops transported by a turbulent flow, focusing in particular on the characterization of the flow events that bring particles to the surface. This interest is motivated by the need of detailed information about the near-interface flow field in usual engineering practice, e.g. for the development of physics-based models or correlations able to predict transfer rates across a liquid-liquid interface [48]. Currently, industrial CFD tools can only rely on mechanistic correlations to predict the capture efficiency of a full-scale equipment [48, 107].
To study the targeted three-phase turbulent flow, we use a computational approach that couples the direct numerical simulation (DNS) of the carrier fluid and drops with

an interface-capturing method for the evolution of the drop surface and a Lagrangian tracking method for the particle dynamics.

Three-phase computational models like the one adopted here pose computational challenges in terms of modelling the interactions among the different phases and the complex dynamics produced by a moving, deformable interface [40]. Drops introduce additional physical mechanisms into the flow due to their ability to deform but also to breakup and coalesce with other drops, thus changing the overall surface area available for particle capture. The problem is complicated further by the wide range of length scales involved, from the interface thickness - $\mathcal{O}(10^{-9})$ m - to the particle size - $\mathcal{O}(10^{-5})$ m - to the drop size - $\mathcal{O}(10^{-2})$ m. Because of these complexities, most of the numerical studies available in the literature focus on the role that surface physicochemical forces have in determining particle adsorption in no-flow or viscous flow conditions, when particle-drop interactions are not affected by the flow hydrodynamics. Examples include the study of the behaviour of a single particle trapped at a planar fluid interface [8, 97], the surface stress tensor modification for a pendant drop covered by a monolayer of particles in the low-Reynolds-number limit [50], or the attachment of a colloidal particle to the surface of an immersed bubble rising in still fluid [77], to name a few recent works. Also relevant is the study by [105], who developed a DEM-VOF method to reproduce drop formation and interface perturbations from a single particle. The same methodology was applied by [134] to study gas-solid-liquid-flows of relevance for sedimentation problems.

The particles considered in this study are very small and they are expected to act in a similar way to surfactant molecules. The effect of dissolved surfactants is reducing surface tension of the interface with respect to the clean interface (without surfactant) [128, 8] affecting the drop deformability and leads to coalescence and breakup processes. Unlike the effect of surfactants on the local modifications of the surface tension has been widely investigated [12, 127, 85, 76], the effect of particles has received comparatively little attention, in particular as far as particle loading and spatial distribution at the interface are concerned [51]. Most the the particle-laden interface system has been studied in the flow condition dominated by viscous forces [112, 80, 27]. Such systems can be found in foam and emulsion stabilisation problems [144] where particles are adsorbed to the air-water interface and increase the surface elasticity.

All of the above-mentioned studies have contributed to the physical understanding of particle-laden fluid interfaces, but do not consider turbulent flow conditions: Clearly, the flow hydrodynamics must be accounted for in turbulent systems, which are the focus of our investigation and (to the best of our knowledge) have not been examined before. Intuitively, one expects particles to be brought in the near-interface region by coherent jet-like fluid motions able to generate local deformations of the drop surface along the surface itself (via the tangential stress they generate) but also along the interface-normal direction (via the pressure fluctuations and normal stresses they induce). When strong enough, these deformations will produce a change in the topology of the flow surrounding each drop, as compared to the topology of an unladen flow [39], and will play a role in the particle adhesion process. To examine this role, we have concentrated our analysis on the fluid motions that occur in the proximity of the interface, where the smallest hydrodynamic length scales are typically located.

For this purpose, we consider a density-/viscosity-matched flow that allows uncoupling

of inertial effects associated with particle size from those due to differential density [78]. The choice of considering matched-viscosity and matched- density fluids are the followings; From an applicative point of view, the matched-density assumption appears to be fully justified by the fact that we are interested in a liquid-liquid dispersion while the matched-viscosity assumption appears to be relevant for situations in which the two fluids are water and low-viscosity silicone oil. For different combinations of immiscible fluids, the difference in viscosity would influence drop breakup and coalescence, thus introducing an additional complexity into the problem. As shown by Roccon et al. [109], drops coalesce and break following a complex dynamics that is primarily controlled by the interplay between turbulence fluctuations (measured by the Reynolds number), surface tension (measured by the Weber number), and the viscosity ratio. Qualitatively, an increase of drop viscosity decreases the break-up rate, very much like an increase of surface tension does. Eventually, however, a steady-state in the number of drops is always achieved regardless of the viscosity difference: This is exactly the condition in which particles are injected into the flow. Therefore, considering that the objective of our study is to highlight the effects of turbulence and surface tension on the particle capture process, we decided to start from a reasonable and well-controlled, albeit simplified, flow instance. Definitely, considering non-matched viscosities (and possibly non-matched densities) could represent a possible future development of the present study.
The diffusion of the particles considered here, which are in the order of micron in size, can be molecular or turbulent for which the turbulent diffusion has been considered. We neglected particle-particle interactions in the simulation presented in Chap. 3, while Excluded-Volume Effects are considered by enforcing the inter-particle collision to reproduce a more realistic particle behavior, in the simulations reported in Chap. 4, which are crucial in determining particle behavior on the interface during the trapping stage but are negligible prior to capture [51]. Even in this simplified case, the presence of an interface is crucial as it represents an elastic, compliant boundary that can modulate the overall energy and momentum transfer the carrier phase and the drops [127].

Thesis outline

- **Chap. 2: Methodology**
  The governing equations that define the dynamics of three-phase turbulent flows are introduced: An Eulerian-Lagrangian approach specifically developed for this three-phase system is used: The flow field in the carrier fluid and inside the droplets is obtained from Direct Numerical Simulation of the Navier-Stokes equations coupled with Phase Field Model (PFM) to describe the drop interface dynamics and particle trajectories are calculated via Lagrangian tracking. The models used to describe the particle-interface interaction and particle-particle collisions are presented in this chapter.

- **Chap. 3: Particle capture by drops in turbulent flow**
  The process of particle capture by the interface of large deformable droplet is investigated: the flow topology in near-drop region, where the particle get cap-

tured, is characterized by means of the statistical tools like surface divergence and the topology parameter. The time evolution of the number of captured particles is examined to introduce a predictive model to estimate the capture rate.

- **Chap. 4: Interface topology and evolution of particle patterns on big drops in turbulence**
  The preferential distribution of particle and its correlation with interface topology is investigated to describe the particle pattern and their distribution via the divergence of the velocity field on the surface. We also correlate the particle clusters with the interface local curvature. The effect of inter-particle collision is also taken into the account to analyze further the correlation and explore the evolution of the particle patterns on the drop surface in a more realistic fashion.

2

Methodology

The common approaches to describe a two-phase flow system will be reviewed throughout the first section, Sect. 2.1; in particular, the Phase Field (PF) method, the selected method for the simulations in this study, will be explained in more detail. The correction formulation of Phase Field is then introduced to limit the drawback of this approach. The following section, Sect. 2.2, is devoted to equations describe the dynamic of the turbulent flow and the coupling of the solution at the interface by imposing the specific boundary conditions. The jump condition imposed by the presence of the interface and the treatment of surface forces and of non-matched thermo-physical properties will be then explained. The particle motion and the governing equations described in Sect. 2.3. A model capable of describing the interaction between moving and deformable interface and particles is described in Sect. 2.3.1. The excluded-volume interactions between particles modelled as Inter-particle collisions Sect. 2.3.2. Once all the equations have been defined, all the relevant dimensionless parameters are introduced, together with the dimensional analysis, Sect. 2.4. The numerical method and pseudo-spectral discretization and the solution algorithm are explained in Sect. 2.5. The details on the Fortran 2003/2008 code and the parallelization strategy are given in Sect. 2.6.

2.1 Interface modelling

This section introduces some approaches adopted in the description of multiphase flows. The numerical methods used to describe the interfaces can be classified in two categories: interface tracking and interface capturing methods. Interface tracking approaches explicitly follow the position of the interface with Lagrangian markers, while interface capturing methods define the interface position as a prescribed value of a color function or phase- concentration field. The main feature differentiating these methods is indeed the definition of the interface: interface tracking methods explicitly track the interface through the advection of a set of marker points, while interface capturing ones use a marker function (representing, for example, the concentration of one of the phases) to define the local distribution of each phase and the interface is identified as a particular value of this function.

2.1.1 Front tracking

In Front Tracking Method, the interface between the fluids can be presented by connecting a set of Lagrangian marker points, defining the interface dynamic and position, that are moved by the local flow field. [11, 140, 141]. Each point is advected by the local flow field

$$\frac{\partial \mathbf{x}^i}{\partial t} = \mathbf{u}^i \tag{2.1}$$

where $\mathbf{x}^i$ is the position vector of the i-th marker point.
The position is updated according to the local flow velocity, $\mathbf{u}^i$, which is interpolated from the flow field computational grid to the marker point position. The interface is then reconstructed by linking together this set of points. Once the interface shape has been computed, the interface curvature and, thus, interfacial forces can be calculated. These forces act at the marker point position and have to be redistributed on the Eulerian grid on which the flow field is solved (smoothing operation). This method thus requires continuous interpolation between the two grids: from the Eulerian (flow field) grid to the Lagrangian marker points to get the advection velocity and from the Lagrangian marker points to the Eulerian grid to obtain the distributed interfacial forces. The main drawbacks of the Front Tracking method are the low accuracy in the interface curvature computation from the Lagrangian marker points and the need for additional models to describe interface topological changes, as coalescences or breakages of the interfaces.

2.1.2 Immersed boundary method

This method was proposed for the numerical simulation of flow patterns around heart valves by [99]. This method has been used widely in the simulation of flows past solid objects bounded by complex and possibly moving boundaries [59, 92] and finite-size particle laden flow [114, 22, 102] and the recent works involving fluid-fluid interfaces [69, 18, 129, 130]. In this method, the interface is represented by moving Lagrangian points; the feedback effect of the interface is taken into account by adding a forcing term to the Navier-Stokes equations. Immersed boundary methods, similarly to front tracking methods, become computationally complex when a large number of separate interfaces is simulated: a separate set of Lagrangian markers has to be tracked in space and time and collisions among different interfaces, and the eventual topological modifications of the interface, have to be accounted for. according with the available literature, topological modifications of the interface have not yet been tackled and are indeed among the possible future developments.

2.1.3 Volume of fluid

The main idea of the Volume Of Fluid (VOF) method is to capture the interface on the same grid used for the flow [54]. An Eulerian marker function, f, defined in the entire domain defines the concentration of one of the phases. This Eulerian marker function is advected by the flow field:

$$\frac{\partial f}{\partial t} + \mathbf{u} \cdot \nabla f = 0 \, . \tag{2.2}$$

The cell value, f_i, of the local concentration is the volume average of the concentration over the computational cell:

$$f_i = \frac{1}{V_i} \int_v f(\mathbf{x}) \mathrm{d}V \ . \tag{2.3}$$

The local marker function is initialized as a Heaviside function; to avoid numerical diffusion of the marker function over time, specific advection algorithms must be adopted [106]. The volume-averaged value in the neighbouring computational cells is used to reconstruct the shape of the interface front, thus avoiding numerical diffusion problems. Interface topological changes (coalescence and breakup) are implicitly handled by the volume-averaged marker function. It must be noted that this volume-averaged marker function, f_i, does not give an exact representation of the interface, which must be reconstructed (using for example a PLIC algorithm [108, 148]). Coalescence and breakage of the interface thus may not be properly resolved [38]. The main advantage of the VOF method is the exact mass conservation of each phase.

2.1.4 Level set

Osher and Sethian [95, 96] introduced for the first time the Level Set (LS) method which belongs to the interface capturing methods. The main idea is to define the interface as the 0-level of a smooth function ϕ; The time behaviour of ϕ can be obtained solving the following advection equation

$$\frac{\partial \phi}{\partial t} + \mathbf{u} \cdot \nabla \phi = 0 \tag{2.4}$$

In the original formulation ϕ is defined as the signed distance from the interface; due to numerical diffusion the marker function may lose its signed distance property. A reinitialization operation may be performed to restore the marker function profile: the iso-level $\phi = 0$ (interface) is kept fixed and the marker function is reinitialized to be the signed distance from the interface. This reinitialization procedure leads to mass leakages among the two phases. To reduce mass leakages the Level Set method is often coupled with a VoF approach [91] or different marker functions are used instead of the signed distance from the interface (conservative Level Set [30]). As for the VoF, the Level Set method is capable of handling merging and breakage of the interface without the need for any additional model. In addition, interface topological changes are accurately captured as the interface is exactly identified as the zero-level of a smooth function. It must be noted, however, that merging and breakage of the interface are not based on physical considerations, but on the local grid resolution. The computation of the curvature and, thus, of interfacial forces is extremely accurate, as it is based on the gradients of the smooth marker function.

2.1.5 Phase field method

The Phase Field (PF) method [13, 14, 15] belongs to the interface capturing methods. This method was initially developed to model the microstructure dynamics of alloys during spinodal decomposition. Later on, the method has been generalized to the

study of incompressible multiphase flow [2, 60] by adding an advection term and coupling the description of the interface to the Navier-Stokes equations. A marker function, ϕ, defines the dynamics of the interface; this function (order parameter) is usually referred to as phase field. The phase field corresponds to the local concentration of one of the phases; this variable changes smoothly across the interface (finite thickness interface). A Cahn-Hilliard equation describes the transport of the order parameter:

$$\frac{\partial \phi}{\partial t} + \mathbf{u} \cdot \nabla \phi = \nabla \cdot (\mathcal{M}_\phi \nabla \mu_\phi) \ . \tag{2.5}$$

With respect to the original Cahn-Hilliard equation, an advection term has been included ($\mathbf{u}$ is the velocity field). The diffusive term on the right hand side is the flux of the chemical potential gradient, with $\mathcal{M}_\phi$ being the mobility (Onsager) coefficient (relaxation time of the interface) and μ_ϕ the phase field chemical potential. Here, the mobility coefficient is set constant [5]. The chemical potential is obtained as the variational derivative of a Ginzburg-Landau free energy functional $\mathcal{F}[\phi, \nabla\phi]$ [5, 60]:

$$\mu_\phi = \frac{\delta \mathcal{F}[\phi, \nabla\phi]}{\delta \phi} \ . \tag{2.6}$$

When considering a mixture of two immiscible fluids, the free energy functional is the sum of two contributions, the first one accounting for the system bulk free energy (f_0), while the second one for the mixing free energy (f_i). The bulk free energy describes the tendency of the system to separate in two pure (stable) phases; the mixing free energy considers the energy stored within the interfacial layer, which, for a fluid-fluid system, corresponds to the surface tension.

$$\mathcal{F}[\phi, \nabla\phi] = \int_\Omega [f_0(\phi) + f_i(\nabla\phi)] \mathrm{d}\Omega \tag{2.7}$$

The first term, f_0, is double well potential, Fig. 2.1(a), with the two minima corresponding to the pure phases, $\phi = \pm\sqrt{\beta/\alpha}$.

$$f_0(\phi) = \frac{\alpha}{4} \left(\phi - \sqrt{\frac{\beta}{\alpha}} \right)^2 \left(\phi + \sqrt{\frac{\beta}{\alpha}} \right)^2 \tag{2.8}$$

The parameters α and β are positive constant corresponding to the bulk properties of the fluids. The mixing term, Fig. 2.1(b) is proportional to the gradient of the marker function, which is maximum at the interface and zero in the bulk of the phases.

$$f_i(\nabla\phi) = \frac{\kappa}{2} |\nabla\phi|^2 \tag{2.9}$$

The positive constant κ defines the magnitude of surface tension. The chemical potential, obtained by taking the variational derivative of the free energy functional, is:

$$\mu_\phi = \frac{\delta \mathcal{F}[\phi, \nabla\phi]}{\delta \phi} = \alpha\phi^3 - \beta\phi - \kappa\nabla^2\phi \ . \tag{2.10}$$

From the chemical potential the phase field equilibrium profile can be derived: at the equilibrium the chemical potential is constant in the entire domain, $\nabla\mu_\phi = 0$.

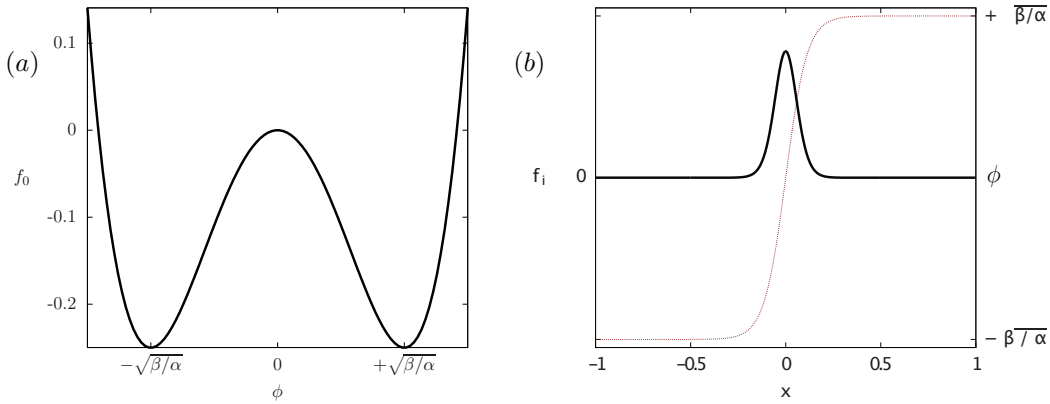

FIGURE 2.1 – Panel (a): double well potential, f_0. Panel (b): mixing free energy, f_i; the interface has been marked for reference with a thin dotted red line.

Imposing a constant phase field chemical potential throughout the entire domain, the equilibrium profile for a flat interface (Fig. 2.2(a)) results in:

$$\phi = \phi_+ \tanh\left(\frac{s}{\sqrt{2}\xi}\right) , \tag{2.11}$$

Where $\xi = \sqrt{k/\beta}$ is ratio which defines the interface thickness, $\phi_+ = \pm\sqrt{\alpha/\beta}$ is the value of ϕ in the bulk of the two phases and s a coordinate normal to the interface. From the equilibrium solution it can be seen how the phase field is constant in the bulk of the phases ($s \to \pm\infty$) and it undergoes a smooth transition following a hyperbolic tangent profile across the interface, whose thickness is proportional to the parameter ξ.

The main advantages of the phase field method include the implicit handling of topological changes at the interface (coalescences and breakages) and the accurate description of the interface and calculation of the interfacial curvature. Thanks to the chemical potential diffusive fluxes, reinitialization of the interface is not needed (as for the LS method): specific advection schemes are not necessary to keep the marker function profile. The main drawbacks of the phase field method are shrinkage, coarsening and misrepresentation of surface forces and thermo-physical properties. As for the Level Set method, also the phase field method suffers of mass leakages among the phases (shrinkage): when a double well potential is adopted together with a constant mobility, the phase field deviates from its equilibrium profile and the phase enclosed by the interface diffuses in the other phase to restore the equilibrium profile [35, 150]. Shrinkage could be avoided by adopting a non-constant mobility and a different bulk free energy functional (for example a logarithmic bulk free energy functional); this choice would however introduce severe numerical difficulties (including singularities in the free energy functional) in the solution of the equation, also reducing the stability of the numerical method. For these reasons a constant mobility together with a double well potential are usually preferred. The energy minimization criterion on which the method is based introduces coarsening phenomena: larger domains of one

phase grow at the expense of smaller domains of the same phase to reduce the system interfacial energy. The last drawback, misrepresentation of surface forces and thermo-physical properties, originates from the deviation of the phase field from its equilibrium profile: overshoots and undershoots of the phase field may generate unphysical values of surface tension forces and negative values of the thermo-physical properties. Thermo-physical properties (density and viscosity) are assumed to be a function of the phase field, thus undershoots and overshoots of the phase field could lead to negative/unphysical values of these properties. Further details on the treatment of non-matched thermo-physical properties among the phases are reported in Sect. 2.2. The following section addresses the problem of shrinkage, coarsening and misrepresentation of surface forces and thermo-physical properties: a profile-corrected [7, 79, 124] and a flux-corrected [153] phase field formulations are introduced to limit these drawbacks.

Mass conservation methods for the phase field

Shrinkage, coarsening and misrepresentation of surface forces and thermo-physical properties negatively affect the quality of the simulation [67]. Shrinkage and misrepresentation of interfacial forces and thermo-physical properties occur when the interfacial profile deviates from the hyperbolic tangent equilibrium profile; for example, turbulent fluctuations and shear at the interface can perturb the interfacial profile. To overcome the method drawbacks, the corrected formulations of the original phase field method have been proposed [7, 79, 153]. The original phase field method formulation for incompressible multiphase flows [2, 60] from now on will be referred to as classic formulation.

Surface tension forces are defined to match the exact surface tension of the sharp interface model [5, 60, 65, 66, 68, 149]: the integral of the system free energy density across the interface must be equal to the surface tension, σ.

$$\sigma = \frac{\beta\kappa}{\alpha}\int_{-\infty}^{+\infty}\mathcal{F}[\phi,\nabla\phi]\mathrm{d}x \tag{2.12}$$

The equilibrium profile, which minimizes the free energy, is used in the integration:

$$\sigma = \frac{2\sqrt{2}}{3}\frac{\beta\kappa}{\alpha\xi} = \frac{2\sqrt{2}}{3}\frac{\sqrt{\beta^3\kappa}}{\alpha}\,. \tag{2.13}$$

Indeed, the surface forces are calculated based on the equilibrium interfacial profile, Eq. (2.13): an out-of-equilibrium interfacial profile introduces an error in the calculation of these forces. Two corrected formulations have been proposed to restore the equilibrium profile, profile-corrected formulation [7, 79] and flux-corrected formulation [154]. The profile-corrected formulation introduces a penalty flux,f_p, that forces the interfacial profile towards its equilibrium profile; this penalty flux is proportional to the magnitude of the perturbation from the equilibrium defined as:

$$f_p = \frac{\lambda}{Pe_\phi}\left[\nabla^2\phi - \frac{1}{\sqrt{2}Ch}\nabla\cdot\left((1-\phi^2)\frac{\nabla\phi}{|\nabla\phi|}\right)\right]\,, \tag{2.14}$$

with the parameter λ set according to the scaling proposed b Zhang and Ye [153], Soligo et al. [124].
The flux-corrected phase field model builds on the profile-corrected formulation: in addition to the profile-correction penalty flux f_p, the component normal to the interface of the chemical potential gradient is canceled out by adding an additional flux f_f. This way, no diffusive fluxes normal to the interface appear, preventing shrinkage and coarsening. This flux reads as

$$f_f = -\frac{1}{Pe_\phi}\nabla \cdot \left[\left(\nabla\mu_\phi \cdot \frac{\nabla\phi}{|\nabla\phi|}\right)\frac{\nabla\phi}{|\nabla\phi|}\right] . \tag{2.15}$$

The normal to the interface is defined as $\mathbf{n} = \nabla\phi/|\nabla\phi|$ [135]. The flux f_f is the projection on the normal to the interface of the phase field chemical potential gradient. As the diffusive flux normal to the interface has been removed, shrinkage and coarsening phenomena strongly reduce. The generic penalty flux, f_c, used in the simulations corresponds to the sum of the fluxes mentioned above, $f_c = f_p + f_f$; added to the right hand side of the classic formulation of the phase field.

2.2 Flow field

The dynamics of the turbulent flow is described by Continuity and Navier-Stokes equations. The flow fields of the two phases are coupled at the interface where specific boundary conditions for the velocity and stress must be satisfied [6, 147]. The presence of moving and deformable interface is then accounted for in the Navier-Stokes equations with an interfacial term. The boundary condition for the velocity reads as:

$$\mathbf{u}_1 \cdot \mathbf{n} - \mathbf{u}_2 \cdot \mathbf{n} = 0 , \tag{2.16}$$

Where $\mathbf{u}_1$ and $\mathbf{u}_2$ are the velocity vectors at the two sides of the interface and $\mathbf{n}$ is the normal vector to the interface. The right hand side of the Eq. (2.16) is zero describing that there is no jump for velocity and it is continuous across the interface.
We also need to write a boundary condition connecting the state of stress in each fluid at the interface. This condition can be written as follows:

$$\mathbf{T}_1 \cdot \mathbf{n} - \mathbf{T}_2 \cdot \mathbf{n} = \mathcal{K}\sigma\mathbf{n} - \nabla_s\sigma , \tag{2.17}$$

Where $\mathbf{T}_1$ and $\mathbf{T}_2$ are the stress tensors in the two phases at the interface, σ is the surface tension, $\mathcal{K}$ is the mean curvature and ∇_s is the surface gradient operator. This equation imposes a jump condition in the stress tensor at the interface. The term $\mathcal{K}\sigma\mathbf{n}$ is normal component whereas the term $-\nabla_s\sigma$ is tangential component of the stress jump. The last term vanishes when surface tension is uniform.
The following section describes the commonly used approach to fulfill the jump conditions imposed by the Eq. (2.17).

Treatment of surface tension forces

The jump condition, which is introduced by the surface tension, for the stress along the normal and tangential direction of the interface is accounted considering a source

term in the right hand side of the NS equation. First term on the right hand side of Eq. (2.17), represents the normal stress jump, is proportional to the curvature $\mathcal{K}$ and to the value of the surface tension σ. When the surface tension is not uniform the tangential jump, second term, appears. The surface tension forces, $\mathbf{f}$, can be composed in a normal $\mathbf{f}_n$ and tangential $\mathbf{f}_t$ components [10, 61, 104] :

$$\mathbf{f} = \mathbf{f}_n + \mathbf{f}_t = -\mathcal{K}\sigma(\mathbf{x}_s)\delta(\mathbf{x}_s)\mathbf{n} + \nabla_s\sigma(\mathbf{x}_s)\delta(\mathbf{x}_s) \,, \tag{2.18}$$

Where $\mathbf{x}_s$ is the interface position, depending on the method used to describe it, the δ function can be discretized in different ways [104]. In the frame work of phase field method, $\mathbf{n}$, δ, and $\mathcal{K}$ are defined as [4, 135] :

$$\mathbf{n} = \frac{\nabla\phi}{|\nabla\phi|} \,, \qquad \delta = \frac{3|\nabla\phi|^2\xi}{\sqrt{8}\phi_+^2} \,, \qquad \mathcal{K} = \nabla\cdot\mathbf{n} \,, \tag{2.19}$$

The mean curvature is computed as:

$$\mathcal{K} = \nabla\cdot\frac{\nabla\phi}{|\nabla\phi|} = \frac{\nabla^2\phi}{|\nabla\phi|} - \frac{1}{|\nabla\phi|^2}\nabla\phi\cdot\nabla(|\nabla\phi|) \,. \tag{2.20}$$

The interfacial tension at the fluid-fluid interface depends on the temperature and the composition of the interface. If we assume these to be uniform, then the gradient of surface tension will vanish everywhere on the interface. This means that tangential stress is continuous across the interface because the jump in it is zero. As a result, the surface tension force equals to the normal component of the stress jump.

$$\mathbf{f} = \mathbf{f}_n = -\frac{3\sigma\xi}{\sqrt{8}\phi_+^2}\nabla^2\phi\nabla\phi \tag{2.21}$$

The same result can be obtained following the procedure proposed by [70]. In this formulation, the Korteweg stress tensor, τ_c, describe the normal stress introduced in the Navier-Stokes equations.

$$\mathbf{f}_n = \frac{3\sigma\xi}{\sqrt{8}\phi_+^2}\nabla\cdot\tau_c \tag{2.22}$$

$$\tau_c = (|\nabla\phi|^2\mathbf{I} - \nabla\phi\otimes\nabla\phi) \tag{2.23}$$

So the surface tension force can be written as:

$$\mathbf{f} = \frac{3\sigma\xi}{\sqrt{8}\phi_+^2}\nabla\cdot(|\nabla\phi|^2\mathbf{I} - \nabla\phi\otimes\nabla\phi) \tag{2.24}$$

The two formulations, Eq. 2.24 and Eq. 2.21, are equivalent.

Treatment of non-matched properties

The two phases can have different thermo-physical properties, in particular density [36] and viscosity [109]. Density and viscosity depend on the local concentration of each phase. In this context, the thermo-physical properties are defined as a linear function of the phase field: at the interface they undergo a smooth transition following

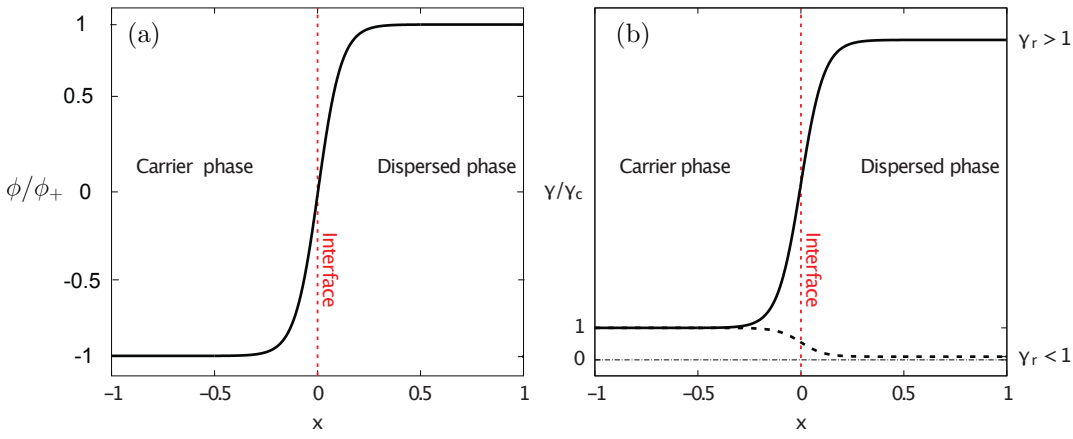

FIGURE 2.2 – In the panel (a) the equilibrium profile of ϕ for a planar interface is shown. In the panel (b) profile of a generic thermo-physical property γ across the interface (red dashed line) for two different property ratios γ_r is shown. The carrier phase thermo-physical property γ_c is taken as reference value. The interfacial layer is the region in which the phase field spans $\pm 96\%$ of its bulk value.

the phase field profile. This feature circumvents all the complications that could arise from jumps and discontinuities across the interface. The properties of the carrier phase are taken as reference quantities: the carrier phase density, ρ_c, and the carrier phase viscosity, η_c. The density and viscosity ratios among the two phases are respectively defined as:

$$\rho_r = \frac{\rho_d}{\rho_c} \quad , \qquad \eta_r = \frac{\eta_d}{\eta_c} \, , \tag{2.25}$$

with the subscripts d denoting the dispersed phase properties and c the carrier phase properties. In Fig. 2.2a the profile of ϕ for a planar interface, red dashed line, at equilibrium condition is depicted; ϕ goes under smooth transition in interfacial layer ($\pm 96\%$ of the phase field bulk value). Fig. 2.2b shows the profile of a generic thermo-physical property, either density or viscosity, across the interface which is identified by the red dashed line. Two different property ratios are displayed, $\gamma_r > 1$ (solid line) and $\gamma_r < 1$ (dashed line). As the property of the carrier phase (phase field bulk value $\phi = -\sqrt{\beta/\alpha}$) are taken as a reference, the value of the dimensionless thermo-physical property is equal to one in the bulk of the carrier phase.

$$\rho(\phi) = \rho_c \left[1 + \frac{\rho_r - 1}{2} \left(\frac{\phi}{\sqrt{\beta/\alpha}} + 1 \right) \right] \tag{2.26}$$

$$\eta(\phi) = \eta_c \left[1 + \frac{\eta_r - 1}{2} \left(\frac{\phi}{\sqrt{\beta/\alpha}} + 1 \right) \right] \tag{2.27}$$

Navier-Stokes and Continuity equation

The mass conservation (continuity equation) for incompressible flows results in a divergence-free flow:

$$\nabla \cdot \mathbf{u} = 0 \, . \tag{2.28}$$

And the final form of the Navier-Stokes for a divergence-free velocity field can be now obtained as follows.

$$\rho(\phi)\left(\frac{\partial \mathbf{u}}{\partial t} + \mathbf{u} \cdot \nabla \mathbf{u}\right) = -\nabla p + \nabla \cdot \left[\eta(\phi)(\nabla \mathbf{u} + \nabla \mathbf{u}^T)\right] + \rho(\phi)\mathbf{g} + \frac{3\sigma\xi}{\sqrt{8}\phi_+^2}\nabla \cdot \tau_c \, , \tag{2.29}$$

with $\mathbf{u} = (u, v, w)$ being the velocity field, t time, ∇p the pressure gradient, $\rho(\phi)$ and $\eta(\phi)$ respectively the local density and dynamic viscosity, $\mathbf{g}$ the gravity acceleration, τ_c the Korteweg tensor [70] defined in Eq. (2.23).

2.3 Particle tracking

The motion of the particles is described by a set of ordinary differential equations for the particle velocity and position, which stem from the balance of the forces acting on the particles. Particles are assumed to be neutrally-buoyant ($\rho_p = \rho_f$, no effect of gravity) and smaller in size than the Kolmogorov length scale. In this study, we considered two force contributions: The drag and capillary force, that are exerted on the particles when they interact with the interface thus allowing for particle adhesion. With the above assumptions the Lagrangian equations of motion for the particles, read as

$$\frac{\partial \mathbf{x_p}}{dt} = \mathbf{u_p} \, , \tag{2.30}$$

$$m_p \frac{\partial \mathbf{u}_p}{\partial t} = \mathbf{F}_\mathrm{D} + \mathbf{F}_\mathrm{C} \, , \tag{2.31}$$

Where $\mathbf{F}_\mathrm{D}$ is drag force and $\mathbf{F}_\mathrm{C}$ capillary force. $\mathbf{x_p}$ and $\mathbf{u_p}$ are the particle position and velocity, respectively; m_p is the particle mass.
The drag force reads as:

$$\mathbf{F}_\mathrm{Drag} = \frac{3}{4}\frac{\rho_f}{\rho_p}\frac{m_p}{d_p} C_D(\mathbf{u}_{@p} - \mathbf{u}_p)|\mathbf{u}_{@p} - \mathbf{u}_p| \, , \tag{2.32}$$

where d_p, ρ_p are particle diameter and density, ρ_f fluid density and $\mathbf{u_{@p}}$ is the fluid velocity at particle position (obtained using a sixth-order Lagrange polynomials interpolation scheme). The Stokes drag coefficient, C_D, introduced to correct the drag force using the Schiller-Naumann correlation [116] and defined as

$$C_D = \frac{24}{Re_p}(1 + 0.15 Re_p^{0.687}) \, . \tag{2.33}$$

Re_p is the particle Reynolds number

$$Re_p = |\mathbf{u}_{@p} - \mathbf{u}_p| d_p / \nu_f \ . \tag{2.34}$$

ν_f is fluid kinematic viscosity. Substituting Eq. (2.33) and Eq. (2.34) in Eq. (2.32), drag force reads as

$$\mathbf{F}_\mathrm{D} = 3\pi d_p \mu_f (\mathbf{u}_{@p} - \mathbf{u}_p)(1 + 0.15 Re_p^{0.687}) \ , \tag{2.35}$$

Where μ_f is the fluid dynamic viscosity. The capillary force is defined as'

$$\mathbf{F}_c = \mathcal{A}\pi\sigma\mathcal{D}\mathbf{n} \ , \tag{2.36}$$

where $\mathcal{A}$ is dimensionless parameter that characterises the magnitude of the capillary adhesion force (which incorporates the effect of the contact angle θ between the particle and the interface as well as the effect of the particle-to-drop size ratio) and $\mathbf{n}$ is the normal unit vector pointing from the particle center of mass to the zero-level set of ϕ. $\mathcal{D}$ is the interaction distance between the center of the particle and the nearest $\phi = 0$ point, which defines the range of action of the capillary force. The force itself and how it is modeled will be explained in detail in Subsect. 2.3.1.
Finally, The particle equation of motion can be written as

$$m_p \frac{\partial \mathbf{u}_p}{\partial t} = 3\pi d_p \mu_f (\mathbf{u}_{@p} - \mathbf{u}_p)(1 + 0.15 Re_p^{0.687}) + \mathcal{A}\pi\sigma\mathcal{D}\mathbf{n} \ . \tag{2.37}$$

Dividing both side of Eq. (2.37) by m_p and substitute the value of $m_p = \rho_p \pi d p_p^3/6$, it can be written as:

$$\frac{\partial \mathbf{u}_p}{\partial t} = \frac{(\mathbf{u}_{@p} - \mathbf{u}_p)}{\tau_p}(1 + 0.15 Re_p^{0.687}) + \frac{6\mathcal{A}\sigma\mathcal{D}\mathbf{n}}{\rho_p d_p^3} \ , \tag{2.38}$$

where $\tau_p = (d_p^2 \rho_p)/(18\mu_f)$ is the dimensional particle relaxation time. Particles are always in the Stokes regime. This was verified by measuring their Reynolds number throughout the simulation. Re_p is always significantly smaller than unity, and therefore the drag force acting on the particles follows the Stokes law.

2.3.1 Particle-interface interaction model

The interactions among the particle and interface pose computational challenges in term of modelling. In this section, some approaches adopted to model particle-interface interaction will be introduced. Among all approaches, the FIPI model has been chosen to be the proper model for our simulations since it is able to model the point-wise particles, which is the target of this study, and it could handle the interaction between large number of particles and deformbale interfaces.

Extended DLVO theory

The extended DLVO theory (XLDVO) is one of the approaches to model particle-interface interactions [46, 47]. In this theory the van der Waals, electrical double layer

and hydrophobic interaction energies have been taken into account to simulate the interactions. The van der Waals is a microscopic-scale attraction force generated from electrical interactions between two or more atoms or molecules [57]. The Hamaker approximation describe the van der Waals potential energy for the two spherical particles and bubble for short distances; This interaction between bubble and particle is repulsive.
The electrical double layer potential energy is determined based on the Hogg-Healy-Fuerstenau (HHF) equation, which assumes that the surface potentials of both particle and bubble remain constant as the separation distance decreases [55]. A single exponential form as a function of the strength of the hydrophobic interaction and the decay length has been adopted to describe the hydrophobic force in this approach [45]. This model can describe the interaction between particle and bubble/droplet for the stationary interface to which particles approach. The particle and bubble considered as two spheres and the model is limited to the simulation of finite particle numbers [46].

Boundary resolved models

The interaction of finite size particle and binary fluid can be modeled by Boundary-resolved model [118, 26, 44, 77]. In this model an additional surface term is added to the free energy of Cahn model. The surface term modeling the interaction at the interface between the solid and fluid reads as

$$\mathbf{F}_s[\psi(\mathbf{x}_s, t)] = \frac{1}{\beta} \int_s (-H\psi)\, ds \;, \tag{2.39}$$

where $\mathbf{x}_s$ is the position of solid surface, s is the total area of solid surface, and H is a constant parameter to control the wettability by which the arbitrary wettability at the solid surface can be tuned. H is zero when the surface has neutral wettability for both 'A' and 'B' molecules; when $H < 0$ or $H > 0$, the surface has a strong affinity for one of the molecules. In this method the sharp particle boundary is replaced with a diffuse interface across which a particle concentration field goes under smooth transition from unity (particle region) to zero (binary fluid region).
The advantage of this model is to obviate the need of dynamic mesh around the particle. The attachment of fine particles are normally modelled as point particles, therefore the deformation of the fluidic interface and the coupling between the solid and the binary fluid are neglected. The boundary-resolved simulation would overcome many of the shortcomings associated with point-particle models. This model can simulate properly the interaction among finite-size particles and interfaces but it could not handle the large number of particles.

FIPI model

When a spherical particle is adsorbed in a fluid interface, a capillary force acts on the particle along the three phase contact line (CL) resulting from surface tension. This force reads as [119]:

$$F_c = \oint_{CL} \sigma \mathbf{n_c}\, ds \;, \tag{2.40}$$

where $\mathbf{n_c}$ is the unit vector normal to the contact line pointing out of the particle and σ is the surface tension. In the present study, we will consider small particles. By small, we mean the particle size d_p is smaller than the smallest length scale of the fluid (Kolmogorov scale). The expression of the capillary force, corresponds to the case of small spherical particles adsorbed at a fluid interface, has been adopted in several previous studies to model particle-interface interactions [50, 134, 41].

In such cases, in which the boundary conditions on the particles are not explicitly enforced, Chuan and Botto [50] introduced a model, FIPI model, for capillary force on particle by knowing it is linear function of interface distortion [62], based on the distance from the particle center to the nearest zero-level fluid interface ($\mathcal{D}$). The dimensional expression of the force reads as

$$\mathbf{F}_c = \begin{cases} \mathcal{A}\pi\sigma\mathcal{D}\mathbf{n} & \text{if } \mathcal{D} \leq r_p \\ 0 & \text{if } \mathcal{D} > r_p \end{cases} \tag{2.41}$$

.

For each particle, $\mathcal{D}$ can be obtained directly by inverting the equilibrium profile of the phase field, ϕ_{eq}, from Eq. (2.11) which reads

$$\mathcal{D} = \left| \frac{\sqrt{2}}{2}\ \xi\ \log\left(\frac{1+\Phi}{1-\Phi}\right) \right| , \tag{2.42}$$

where $\Phi = \phi_{@p}/\phi+$, $\phi+ = \sqrt{\beta/\alpha}$ is the absolute value of ϕ in the bulk of the two phases and $\phi_{@p}$ is the value of the phase field variable interpolated at the particle position. This equation is used to compute the distance from the particle center to the interface when the particle is at the interfacial region ($|\Phi| < 1$).

The spatial distribution of $\mathbf{F}_c$ across the transition layer centered at the drop interface is shown in Fig. 2.3, together with the spatial distribution of the order parameter, ϕ. The order parameter goes under smooth transitions from -1 (corresponding to the carrier fluid) to $+1$ (corresponding to the drop) across a layer of thickness $\mathcal{T} = 4.1Ch$. From this figure and from Eq. (2.41), it is clear that $\mathbf{F}_c$ reproduces the effect of a potential well centered at the interface that favours particle adhesion and attachment to the surface of the drop as soon as the particle touches the interface. This force pushes the particles towards the interface and capture them. The capillary force F_c is zero everywhere but within a distance $\mathcal{D}$ from the interface, where its absolute value decreases linearly with the separation between the particle center and the interface. In this work, $\mathcal{D}/\mathcal{T} \simeq \mathcal{O}(10^{-1})$.

When $\mathcal{D} > r_p$, the particle is considered detached from the fluid interface and the capillary force is zero.

The value of the parameter $\mathcal{A}$ is chosen to satisfy the condition that the adsorption energy $E_{ads} = \pi\sigma r^2(1 - |\cos\theta|)^2$, corresponding to the difference between the energy of a particle fully displaced from the interface into the bulk phase and the energy of the particle settling at equilibrium at the interface, balances the desorption energy

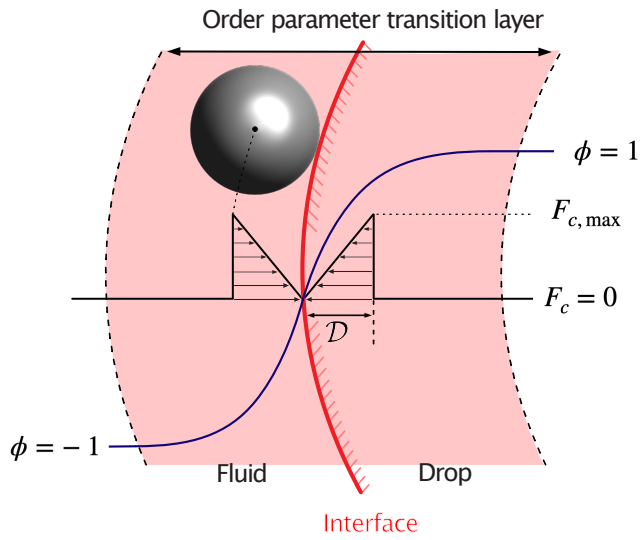

FIGURE 2.3 – Order parameter and capillary force spatial distribution. The order parameter ϕ transitions from $\phi = -1$ to $\phi = +1$, corresponding to the fluid and drop respectively, across the transition layer colored in light red. The capillary force F_c is zero everywhere except in the regions where $\mathcal{D} \leq r_p$. The maximum value is exerted when it touches the interface, $\mathcal{D} = r_p$ and it decreases linearly to zero when $\mathcal{D} = 0$.

$E_{des} = \frac{1}{2}\mathcal{A}\pi\sigma r^2$, corresponding to the energy required for particle detachment from the interface [41, 51].

2.3.2 Particle-particle collision

An elastic collision algorithm based on the proactive approach is used to model Inter-particle collision. In this method the collisions are detected at the beginning of each time step and the time to collision t_{ij} is calculated for each colliding pair. The particles are advanced in time using these small tiny sub-interval t_{ij} of the normal time step. This method allows for multiple collision, i.e. a particle can collide more than once within each time step, and the particles can not overlap , leading to a more realistic particle behaviour and determining accurately the collisions.
The drawback of this approach is the required computational cost for collision detection and particle advancement. The number of multiple collision may increase exponentially, thus the number of required sub-intervals to advance the particles increases. To reduce and make feasible the computational cost required to search for possible collisions and speed-up the particle tracking within each time step the neighbour approach proposed by Sundaram and Collins [136, 137] has been adopted. In this approach two arrays, neighbour list and linked list, are created. The former that contains the index of neighbouring cell is created at initial time step and the latter containing the list of neighbouring particles within the same cell is updated at the beginning of the each time step. Using these arrays, restricts the search of possible

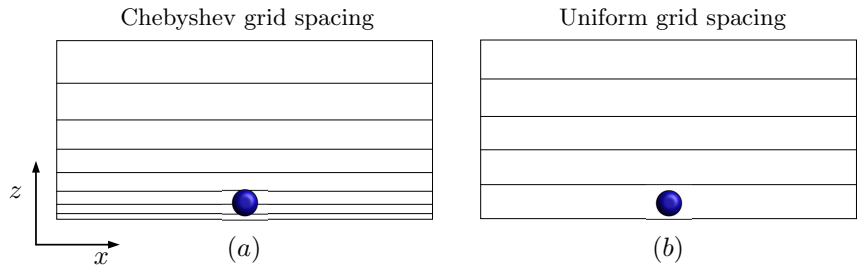

FIGURE 2.4 – Searching lattices considering Chebyshev polynomial (a) and uniform mesh (b). The grids generated by Chebyshev polynomial (a) are finer near to wall and coarser in channel center. To satisfy the only criteria for seeking the colliding pair, the cell size must be bigger than the particle radius plus 1% of the radius, $r_p + 1\%$ [145] .

collision only to the cell containing the calling particle and 26 neighbouring cells and makes the algorithm much faster. If the search involved all the particles, the computational costs would be equal to N_p^2 where N_p is the total number of particles released in entire domain. The introduction of these two arrays decreases the required computational costs to $N_p \cdot \log(N_p)$ which is clear time saving.
The *neighbouring list* method is based on the creation of the "searching lattices". The domain is dived into special mesh at the beginning of the simulation with certain number of cells in each direction. There are no fixed rules in the choice of the cell numbers. It is clear that if the number is low, there will be few big cells containing a high number of particles; consequently, the searching process is slow. On the contrary, if the number of cells is too high, the memory problem to store the working array will occur. The only criteria has to satisfy is the cell size with respect to the particle size; it must be bigger than particle radius plus 1% of the radius in each direction [145]. This is to assure that if a particle center locates between two adjacent cells, it is still possible for algorithm to detect the colliding pair. This mesh grid is uniform in all directions unlike the Eulerian grids on which the equations are discretized and solved. The Eulerian grids are not uniform in wall normal direction; it is refined close to wall due to the Chebyshev polynomial distribution. The minimum grid spacing in z direction could be smaller than the particle radius, as we see in Fig. 2.4, and the only criterion may not be satisfied. Therefore to avoid the possible problem, a uniform division also in wall normal direction has been adopted.

The next step is to identify the cell index of the created lattices; with a number so that the search for possible collisions can be restricted to the 26 neighboring cells of the one containing the particle depicted in red boundary (colored in blue) in Fig. 2.5. A detailed overview of the algorithm used to detect collision events is reported in Appendix A

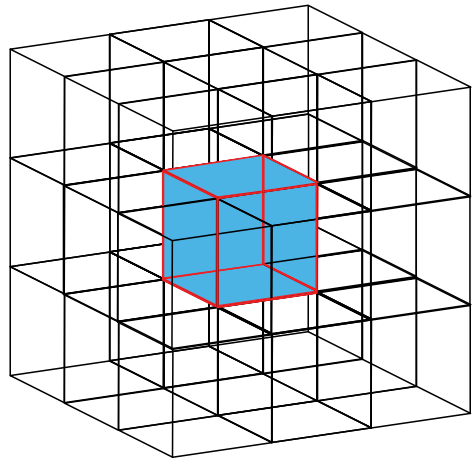

FIGURE 2.5 – Searching lattices to find the collision events for a sample particle located in middle cell (blue cell). This cell is surrounded by 26 cells and thus the search for possible collisions will be restricted to these neighbouring cells.

2.4 Dimensional analysis

All the equations presented so far are in dimensional form; the non-dimensionalizing procedure will be now introduced. Dimensionless quantities will be indicated using a superscript *. A flat channel geometry is adopted in all the simulations presented in this work, Fig. 2.6. The channel is bounded by two solid walls at $z = \pm h$, with h being the channel half height. Friction velocity is the reference velocity in such pressure driven flow system.

$$u_\tau = \sqrt{\tau_w/\rho_c} \tag{2.43}$$

where τ_w is the shear stress at the wall and ρ_c the reference density. From the velocity and the length scale, the time scale can be derived:

$$\mathbf{x}^* = \frac{\mathbf{x}}{h} \quad , \qquad \mathbf{u}^* = \frac{\mathbf{u}}{u_\tau} \quad , \qquad t^* = \frac{u_\tau}{h} t \; , \tag{2.44}$$

with $\mathbf{x} = (x, y, z)$ being the position, $\mathbf{u} = (u, v, w)$ the fluid velocity and t time. The value of the phase field in the bulk of the phases, $\sqrt{\beta/\alpha}$ is used to make the phase field dimensionless.

$$\phi^* = \frac{\phi}{\sqrt{\beta/\alpha}} \tag{2.45}$$

The thermo-physical properties of the carrier fluid (subscript c) have been taken as reference quantities.

$$\rho^*(\phi^*) = \frac{\rho(\phi)}{\rho_c} = 1 + \frac{\rho_r - 1}{2} (\phi^* + 1) \tag{2.46}$$

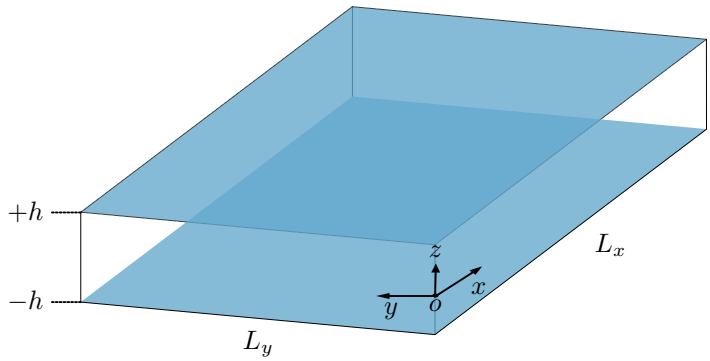

FIGURE 2.6 – Sketch channel used in the simulations. The channel is bounded closed channel by solid walls at $z = \pm h$ and its dimensions are L_x in the streamwise direction (x), L_y in the spanwise direction (y) and $2h$ in the wall-normal direction (z). The reference frame is centered in o, located at the channel mid-plane.

$$\eta^*(\phi^*) = \frac{\eta(\phi)}{\eta_c} = 1 + \frac{\eta_r - 1}{2}\left(\phi^* + 1\right) \ , \tag{2.47}$$

where ρ_r and η_r are the density and viscosity ratios among the two phases.
The dimensionless continuity equation results in:

$$\nabla \cdot \mathbf{u}^* = 0 \ . \tag{2.48}$$

The dimensionless Korteweg stress tensor, τ_c^* is:

$$\tau_c^* = (|\nabla\phi^*|^2\mathbf{I} - \nabla\phi^* \otimes \nabla\phi^*) = \frac{\beta/\alpha}{h^2}\tau_c \ . \tag{2.49}$$

By defining two dimensionless quantities, We and Ch, the dimensionless surface force term becomes:

$$\frac{3\sigma\xi}{\sqrt{8}}\frac{\sigma}{\rho_c u_\tau^2 h}\frac{\sqrt{k/\beta}}{h}\nabla\cdot\tau_c^* = \frac{3}{\sqrt{8}}\frac{Ch}{We}\nabla\cdot\tau_c^* \ . \tag{2.50}$$

The Cahn number, Ch, is the dimensionless interface thickness; it is defined as the ratio ξ/h. The Weber number, We, is the ratio of inertia forces over surface tension forces:

$$We = \frac{\rho_c u_\tau^2 h}{\sigma} \ , \tag{2.51}$$

where σ the reference surface tension .
The dimensionless Navier-Stokes equation is:

$$\begin{aligned}\rho^*(\phi^*)\left(\frac{\partial\mathbf{u}^*}{\partial t^*} + \mathbf{u}^*\cdot\nabla\mathbf{u}^*\right) = &-\nabla p^* + \frac{1}{Re_\tau}\nabla\cdot\left[\eta^*(\phi^*)\left(\nabla\mathbf{u}^* + \nabla\mathbf{u}^{*^T}\right)\right] + \\ &+ \frac{1}{Fr^2}\rho^*(\phi^*)\mathbf{g}^* + \frac{3}{\sqrt{8}}\frac{Ch}{We}\nabla\cdot\tau_c^* \ .\end{aligned} \tag{2.52}$$

The dimensionless pressure is defined as $p^* = p/(\rho_c u_\tau^2)$. The shear Reynolds number, Re_τ is the ratio of inertial over viscous forces:

$$Re_\tau = \frac{\rho_c u_\tau h}{\eta_c} \; ; \tag{2.53}$$

it is defined using the carrier phase properties as reference quantities. The Froude number, Fr is defined as:

$$Fr = \frac{u_\tau}{\sqrt{gh}} \; , \tag{2.54}$$

where g is the modulo of the gravity vector and $\mathbf{g}^*$ is the gravity unit vector.
The dimensionless transport equation for the phase field is:

$$\frac{\partial \phi^*}{\partial t^*} + \mathbf{u}^* \cdot \nabla \phi^* = \frac{1}{Pe} \nabla^2 \mu_\phi^* \; . \tag{2.55}$$

The Péclet number, Pe, is the ratio of convective over diffusive phenomena of the phase field. The dimensionless phase field equilibrium profile is $\phi^* = \tanh(s^*/\sqrt{2}Ch)$, with s^* being a dimensionless coordinate normal to the interface. The chemical potential is made dimensionless by a factor $\sqrt{\beta^3/\alpha}$.

$$\mu_\phi = \sqrt{\frac{\beta^3}{\alpha}} \mu_\phi^* = \sqrt{\frac{\beta^3}{\alpha}} \left({\phi^*}^3 - \phi^* - Ch^2 \nabla^2 \phi^* \right) \tag{2.56}$$

The phase field Péclet number is defined as:

$$Pe_\phi = \frac{u_\tau h}{\beta m_\phi} \, , \tag{2.57}$$

where m_ϕ is the constant mobility coefficient for the phase field.

Lagrangian equation of motion made dimensionless using wall unit scaling system (Please refer to Appendix B for further detail on this scaling) in which the velocity and length and time scales are:

$$\mathbf{x} = \frac{\nu}{u_\tau} \mathbf{x}^+ \, , \quad \mathbf{u} = u_\tau \mathbf{u}^+ \, , \quad t = \frac{\nu}{u_\tau^2} t^+ \tag{2.58}$$

using Eq. (2.38) and defining a dimensionless number, St, the dimensionless equation of particle motion becomes:

$$\frac{\partial \mathbf{x}_p^+}{dt^+} = \mathbf{u}_p^+ \quad , \tag{2.59}$$

$$\frac{\partial \mathbf{u}_p^+}{\partial t^+} = \frac{(\mathbf{u}_{@p}^+ - \mathbf{u}_p^+)}{St} (1 + 0.15 Re_p^{0.687}) + \frac{6A}{\rho_p/\rho_f} \frac{Re_\tau}{We} \frac{\mathcal{D}^+}{{d_p^+}^3} \quad , \tag{2.60}$$

$St = \tau_p/\tau_f$ is the Stokes number, ratio of the particle relaxation time τ_p to the carrier fluid characteristic time $\tau_f = \nu_f/{u_\tau}^2$. d_p^+ is the dimesionless particle diameter and

$\mathcal{D}^+$ is the dimesionless distance between particle center and interface.

In the following the dimensionless notation $^*,^+$ will be dropped for ease of reading; from now on, all equations presented are however dimensionless.
The dimensionless equations are (in order: continuity, Navier-Stokes, density, viscosity, phase field transport, chemical potential and Lagrangian equation of particle motion):

$$\nabla \cdot \mathbf{u} = 0 \; ; \tag{2.61}$$

$$\begin{aligned} \rho(\phi)\left(\frac{\partial \mathbf{u}}{\partial t} + \mathbf{u}\cdot\nabla\mathbf{u}\right) = &-\nabla p + \frac{1}{Re_\tau}\nabla\cdot\left[\eta(\phi)\left(\nabla\mathbf{u} + \nabla\mathbf{u}^T\right)\right] + \\ &+ \frac{\rho(\phi)\mathbf{g}}{Fr^2} + \frac{3}{\sqrt{8}}\frac{Ch}{We}\nabla\cdot\tau_c \; ; \end{aligned} \tag{2.62}$$

$$\rho(\phi) = 1 + \frac{\rho_r - 1}{2}\left(\phi + 1\right) \; ; \tag{2.63}$$

$$\eta(\phi) = 1 + \frac{\eta_r - 1}{2}\left(\phi + 1\right) \; ; \tag{2.64}$$

$$\frac{\partial \phi}{\partial t} + \mathbf{u}\cdot\nabla\phi = \frac{1}{Pe}\nabla^2\mu_\phi \; ; \tag{2.65}$$

$$\mu_\phi = \phi^3 - \phi - Ch^2\nabla^2\phi \; ; \tag{2.66}$$

$$\frac{\partial \mathbf{x}_p}{dt} = \mathbf{u}_p \quad , \tag{2.67}$$

$$\frac{\partial \mathbf{u}_p}{\partial t} = \frac{(\mathbf{u}_{@p} - \mathbf{u}_p)}{St}(1 + 0.15Re_p^{0.687}) + \frac{6A}{\rho_p/\rho_f}\frac{Re_\tau}{We}\frac{\mathcal{D}}{{d_p}^3} \quad , \tag{2.68}$$

The shear Reynolds number and the Weber number are phenomenological parameters, which determine the setup of the problem analyzed. The Cahn number, which sets the interface thickness with respect to the channel size, is determined based on the computational grid. First, the grid spacing and problem size are selected in order to properly resolve the flow configuration studied, then the Ch number is chosen so that there are at least five grid points across the interface. Then, the Péclet number, Pe, is set according to the scaling $Pe = 1/Ch$ [83, 124, 151].
We remark that, in this study, only particles with tiny inertia are considered. For these particles, unsteady forces, such as added mass and lift, can be neglected with respect to drag without introducing major inaccuracies in the description of particle motion. The ratio of the added mass force to the drag force scales as

$$F_{AM}/F_D \sim St \cdot (\rho_f/\rho_p) \; . \tag{2.69}$$

while the ratio of the lift force to the drag force scales as

$$F_L/F_D \simeq \sqrt{\nu_f \left(\frac{\rho_f}{\rho_p}\right) St} \cdot \sqrt{\frac{\partial u_i^+}{\partial x_j^+}} \,. \tag{2.70}$$

Since particle inertia is small in our problem, it compensates the effect of large velocity gradients and, therefore, minor modifications of particle trajectories within the carrier fluid should be expected from inclusion of these two forces in Eq. (2.31). In fact, particles behave nearly as fluid tracers as long as they are brought about by the carrier fluid. Once they reach the near-interface region, the capillary force is expected to be dominant over the other forces (drag, in particular), thus favoring particle adhesion. However, this process may be significantly affected by the turbulence in the bulk of the carrier fluid, which tends to deform continuously the interface and modify the topology of the flow structures with which the particles interact as they approach the drop. Our aim is precisely to highlight the role played by these local flow structures and quantify their effect on particle adhesion.

2.5 Numerical method

The dimensionless system of equations is solved in a closed-channel configuration, with two solid walls at $z = \pm 1$, as shown in Fig. 2.6. A velocity-vorticity approach is adopted to solve the flow field: the Navier-Stokes and continuity equations are replaced by a second-order equation for the wall-normal component of the vorticity (curl of the Navier-Stokes equation), a fourth-order equation for the wall-normal component of velocity (twice the curl of the Navier-Stokes equation), the definition of the wall-normal vorticity and the continuity equation itself. With this approach time-consuming Poisson solvers for the calculation of the pressure field can be avoided. The transport equations for the phase field is directly solved, Eq. (2.65). A more compact notation is now introduced; all non-linear terms that will be time-integrated using an explicit scheme are collected in a non-linear term. The various non-linear terms are $\mathbf{S}$ and S_ϕ, respectively for the Navier-Stokes, phase field transport equation.

$$\begin{aligned}\mathbf{S} = \begin{bmatrix} S_x \\ S_y \\ S_z \end{bmatrix} = &- \mathbf{u}\cdot\nabla\mathbf{u} - \frac{\rho_r - 1}{2}(\phi+1)\left(\frac{\partial \mathbf{u}}{\partial t} + \mathbf{u}\cdot\nabla\mathbf{u}\right) - \Pi + \\ &+ \frac{1}{Re_\tau}\nabla\cdot\left[\frac{\eta_r - 1}{2}(\phi+1)\left(\nabla\mathbf{u} + \nabla\mathbf{u}^T\right)\right] + \\ &+ \frac{\rho(\phi)\mathbf{g}}{Fr^2} + \frac{3}{\sqrt{8}}\frac{Ch}{We}\nabla\cdot\tau_c\end{aligned} \tag{2.71}$$

$$S_\phi = -\mathbf{u}\cdot\nabla\phi + \frac{1}{Pe}\left[\nabla^2\phi^3 - (1+s)\nabla^2\phi + f_c\right] \tag{2.72}$$

The pressure gradient has been split in two components, a constant mean pressure gradient, Π, and a fluctuating component, $\nabla p'$ [121]. A splitting coefficient, s, appears in the phase field transport equation; the splitting of the Laplace operator improves the stability of the numerical scheme [5, 149]. This splitting coefficient is defined as:

$$s = \sqrt{\frac{4Pe\,Ch^2}{\Delta t}}\,, \tag{2.73}$$

with Δt being the integration time step. For the sake of completeness, also the contribution from the corrected phase field formulations, f_c, has been included in the phase field transport equation. In a more compact form, the complete system of equations thus results in:

$$\nabla\cdot\mathbf{u} = 0\,; \tag{2.74}$$

$$\frac{\partial\mathbf{u}}{\partial t} = \mathbf{S} - \nabla p' + \frac{1}{Re_\tau}\nabla^2\mathbf{u}\,; \tag{2.75}$$

$$\frac{\partial\phi}{\partial t} = S_\phi + \frac{s}{Pe}\nabla^2\phi - \frac{Ch^2}{Pe}\nabla^4\phi\,; \tag{2.76}$$

The Navier-Stokes equation is solved in a velocity-vorticity formulation. First, by taking the curl of the Navier-Stokes equation, a transport equation for the vorticity,

$\boldsymbol{\omega}$ is obtained:

$$\frac{\partial \boldsymbol{\omega}}{\partial t} = \nabla \times \mathbf{S} + \frac{1}{Re_\tau}\nabla^2 \boldsymbol{\omega} \, . \tag{2.77}$$

The wall-normal component of this equation gives the wall-normal component of the vorticity vector, ω_z. Then, a fourth-order equation for the velocity can be obtained by taking the curl of Eq. (2.77) (twice the curl of the Navier-Stokes equation).

$$\frac{\partial(\nabla^2 \mathbf{u})}{\partial t} = \nabla^2 \mathbf{S} - \nabla(\nabla \cdot \mathbf{S}) + \frac{1}{Re_\tau}\nabla^4 \mathbf{u} \tag{2.78}$$

The wall-normal projection of this equation results in a fourth-order equation for the wall-normal velocity.
The final system of equations solved results in:

$$\begin{cases} \nabla \cdot \mathbf{u} = 0 \\ \boldsymbol{\omega} \cdot \mathbf{n}_z = (\nabla \times \mathbf{u}) \cdot \mathbf{n}_z \\ \dfrac{\partial(\nabla^2 \mathbf{u})}{\partial t} \cdot \mathbf{n}_z = \left[\nabla^2 \mathbf{S} - \nabla(\nabla \cdot \mathbf{S}) + \dfrac{1}{Re_\tau}\nabla^4 \mathbf{u}\right] \cdot \mathbf{n}_z \\ \dfrac{\partial \boldsymbol{\omega}}{\partial t} \cdot \mathbf{n}_z = \left(\nabla \times \mathbf{S} + \dfrac{1}{Re_\tau}\nabla^2 \boldsymbol{\omega}\right) \cdot \mathbf{n}_z \\ \dfrac{\partial \phi}{\partial t} = S_\phi + \dfrac{s}{Pe_\phi}\nabla^2 \phi - \dfrac{Ch^2}{Pe_\phi}\nabla^4 \phi \end{cases} \tag{2.79}$$

The symbol $\mathbf{n}_z$ represents the wall-normal direction unit vector (z axis). This dimensionless system of equations has been spatially-discretized using a pseudo-spectral approach [16, 58, 101] with Fourier discretization in the streamwise (x) and spanwise (y) directions and Chebyshev polynomials in the wall-normal (z) direction. The adoption of Fourier series in the x and y directions implicitly enforces periodic boundary conditions on all variables along these directions. All variables are Eulerian and are solved on the same computational grid. Variables are interpolated in modal space from one grid to the other by adding/removing high wavenumber modes and renormalizing the modes. A uniform grid spacing is adopted in the streamwise and spanwise directions (Fourier discretization), while in the wall-normal direction Chebyshev-Gauss-Lobatto points were chosen, thus leading to a much finer grid close to the channel walls. The points (x_i, y_j, z_k) of the Cartesian grid are defined as:

$$\begin{aligned} x_i &= (i-1)\frac{L_x}{N_x - 1} && i = 1, \ldots, N_x \\ y_j &= (j-1)\frac{L_y}{N_y - 1} && j = 1, \ldots, N_y \\ z_k &= \cos\left(\frac{k-1}{N_z - 1}\pi\right) && k = 1, \ldots, N_z \end{aligned} \, . \tag{2.80}$$

The number of grid points in each direction is N_x (x direction), N_y (y direction) and N_z (z direction).

The time-advancement is performed adopting a IMplicit-EXplicit scheme (IMEX); the terms $\mathbf{S}$, S_ϕ are integrated explicitly with an Adams-Bashforth scheme, while the other terms implicitly. A Crank-Nicolson scheme is used to integrate the implicit terms of the second order equation for the wall-normal vorticity and of the fourth order equation for the wall-normal velocity. The implicit part of the Cahn-Hilliard equation is integrated with an implicit Euler scheme; this choice reduces the unphysical high frequency oscillations that could arise from the steep gradients of the equations [5, 149]. At the first time step an explicit Euler scheme is used for the explicit part of all the equations. At the generic time step n (current time step) the time-discretized system of equations is:

$$\begin{cases} \nabla \cdot \mathbf{u}^{n+1} = 0 \\ \boldsymbol{\omega}^{n+1} \cdot \mathbf{n}_z = (\nabla \times \mathbf{u}^{n+1}) \cdot \mathbf{n}_z \\ \dfrac{\nabla^2 \mathbf{u}^{n+1} - \nabla^2 \mathbf{u}^n}{\Delta t} \cdot \mathbf{n}_z = \left[\dfrac{3[\nabla^2 \mathbf{S}^n - \nabla(\nabla \cdot \mathbf{S}^n)] - [\nabla^2 \mathbf{S}^{n-1} - \nabla(\nabla \cdot \mathbf{S}^{n-1})]}{2} + \right. \\ \qquad\qquad \left. + \dfrac{1}{Re_\tau} \dfrac{\nabla^4 \mathbf{u}^{n+1} + \nabla^4 \mathbf{u}^n}{2} \right] \cdot \mathbf{n}_z \\ \dfrac{\boldsymbol{\omega}^{n+1} - \boldsymbol{\omega}^n}{\Delta t} \cdot \mathbf{n}_z = \left(\dfrac{3\nabla \times \mathbf{S}^n - \nabla \times \mathbf{S}^{n-1}}{2} + \dfrac{1}{Re_\tau} \dfrac{\nabla^2 \boldsymbol{\omega}^{n+1} + \nabla^2 \boldsymbol{\omega}^n}{2} \right) \cdot \mathbf{n}_z \\ \dfrac{\phi^{n+1} - \phi^n}{\Delta t} = \dfrac{3S_\phi^n - S_\phi^{n-1}}{2} + \dfrac{s}{Pe} \nabla^2 \phi^{n+1} - \dfrac{Ch^2}{Pe} \nabla^4 \phi^{n+1} \end{cases} \tag{2.81}$$

2.5.1 Pseudo-spectral discretization

All equations are solved in modal space; Fourier and Chebyshev transforms are employed to switch from a physical to a modal representation of variables. A generic variable, $f(x, y, z, t)$, in physical space can be represented in modal space as a function of Fourier wavenumbers and Chebyshev polynomials, T_k.

$$f(x, y, z, t) = \sum_{i=0}^{N_x/2} \sum_{j=-N_y/2+1}^{N_y/2} \sum_{k=0}^{N_z-1} \hat{f}(k_{x,i}, k_{y,j}, k, t) T_k(z) e^{\iota(k_{x,i}x + k_{y,j}y)} \tag{2.82}$$

The Fourier coefficient $\hat{f}(k_{x,i}, k_{y,j}, k, t)$ depends on the wavenumbers, $k_{x,i}$ and $k_{y,j}$, on the k^{th} Chebyshev polynomial and on time ($\iota = \sqrt{-1}$ is the imaginary unit). The x and y Fourier wavenumbers are defined as:

$$k_{x,i} = \frac{2\pi(i-1)}{L_x} \qquad i = 1, \ldots, N_x/2 + 1 \,, \tag{2.83}$$

$$k_{y,j} = \begin{cases} \dfrac{2\pi(j-1)\pi}{L_y} & j = 1, \ldots, N_y/2 + 1 \\ -\dfrac{2\pi(N_y - j + 1)}{L_y} & j = N_y/2 + 2, \ldots, N_y \end{cases} . \tag{2.84}$$

Chebyshev polynomials and their derivatives are defined recursively:

$$\begin{aligned} T_0(z) &= 1 & \frac{\partial T_0(z)}{\partial z} &= 0 \\ T_1(z) &= z & \frac{\partial T_1(z)}{\partial z} &= 1 \\ &\vdots & &\vdots \\ T_n(z) &= 2zT_{n-1}(z) - T_{n-2}(z) & \frac{\partial T_n(z)}{\partial z} &= \frac{\partial T_{n-2}(z)}{\partial z} + 2nT_{n-1} \end{aligned} \quad . \tag{2.85}$$

One of the main advantages of spectral and pseudo-spectral method is the accuracy in the calculation of derivatives: spatial derivatives in modal space are exact. However, a truncation error is introduced when truncating the infinite Fourier and Chebyshev series to a finite sum of interpolating functions; nevertheless this truncation error is extremely small.
Derivatives in the homogeneous directions (x and y) can be immediately computed from Eq. (2.82):

$$\frac{\partial f(x,y,z,t)}{\partial x} = \sum_{i=0}^{N_x/2} \sum_{j=-N_y/2+1}^{N_y/2} \sum_{k=0}^{N_z-1} \iota k_{x,i} \hat{f} T_k e^{\iota(k_{x,i}x + k_{y,j}y)} \quad , \quad , \tag{2.86}$$

$$\frac{\partial f(x,y,z,t)}{\partial y} = \sum_{i=0}^{N_x/2} \sum_{j=-N_y/2+1}^{N_y/2} \sum_{k=0}^{N_z-1} \iota k_{y,j} \hat{f} T_k e^{\iota(k_{x,i}x + k_{y,j}y)} \quad . \quad , \tag{2.87}$$

Once defined the variables in modal space, the system of equations Eq. (2.81) can be transformed in modal space. As Fourier modes are all orthogonal, the problem can be split in $(N_x/2+1) \times N_y$ independent subproblems, one for every wavenumber couple $(k_{x,i}, k_{y,j})$. To shorten the notation, in the following the symbol $\hat{f}$ will correspond to the Chebyshev discretization of Fourier modes at a generic wavenumber couple:

$$\hat{f} = \hat{f}_{i,j} = \sum_{k=0}^{N_z-1} \hat{f}(k_{x,i}, k_{y,j}, k, t) T_k(z) e^{\iota(k_{x,i}x + k_{y,j}y)} \quad , \tag{2.88}$$

for each couple $(i,j) \in ([1, N_x/2+1], [-N_y/2+1, N_y/2])$. With this compact notation,

the system of equation results in:

$$
\begin{cases}
\iota k_{x,i}\hat{u}^{n+1} + \iota k_{y,j}\hat{v}^{n+1} + \dfrac{\partial \hat{w}^{n+1}}{\partial z} = 0 \\
\hat{\omega}_z^{n+1} = \iota k_{x,i}\hat{v}^{n+1} - \iota k_{y,j}\hat{u}^{n+1} \\
\dfrac{1}{\Delta t}\left(\dfrac{\partial^2 \hat{w}^{n+1}}{\partial z^2} - k_{i,j}^2\hat{w}^{n+1} - \dfrac{\partial^2 \hat{w}^{n}}{\partial z^2} + k_{i,j}^2\hat{w}^{n}\right) = \\
\qquad = \dfrac{3}{2}\left(-k_{i,j}^2\hat{S}_z^n - \iota k_{x,i}\dfrac{\partial \hat{S}_x^n}{\partial z} - \iota k_{y,j}\dfrac{\partial \hat{S}_y^n}{\partial z}\right) - \\
\qquad - \dfrac{1}{2}\left(-k_{i,j}^2\hat{S}_z^{n-1} - \iota k_{x,i}\dfrac{\partial \hat{S}_x^{n-1}}{\partial z} - \iota k_{y,j}\dfrac{\partial \hat{S}_y^{n-1}}{\partial z}\right) + \\
\qquad + \dfrac{1}{2Re_\tau}\left(k_{i,j}^4\hat{w}^{n+1} + \dfrac{\partial^4 \hat{w}^{n+1}}{\partial z^4} - 2k_{i,j}^2\dfrac{\partial^2 \hat{w}^{n+1}}{\partial z^2}\right) + \\
\qquad + \dfrac{1}{2Re_\tau}\left(k_{i,j}^4\hat{w}^{n} + \dfrac{\partial^4 \hat{w}^{n}}{\partial z^4} - 2k_{i,j}^2\dfrac{\partial^2 \hat{w}^{n}}{\partial z^2}\right) \\
\dfrac{\hat{\omega}_z^{n+1} - \hat{\omega}_z^{n}}{\Delta t} = \dfrac{3}{2}\left(\iota k_{x,i}\hat{S}_y^n - \iota k_{y,j}\hat{S}_x^n\right) - \dfrac{1}{2}\left(\iota k_{x,i}\hat{S}_y^{n-1} - \iota k_{y,j}\hat{S}_x^{n-1}\right) + \\
\qquad + \dfrac{1}{2Re_\tau}\left(\dfrac{\partial^2 \hat{\omega}_z^{n+1}}{\partial z^2} - k_{i,j}^2\hat{\omega}_z^{n+1} + \dfrac{\partial^2 \hat{\omega}_z^{n}}{\partial z^2} - k_{i,j}^2\hat{\omega}_z^{n}\right) \\
\dfrac{\hat{\phi}^{n+1} - \hat{\phi}^{n}}{\Delta t} = \dfrac{3\hat{S}_\phi^n - \hat{S}_\phi^{n-1}}{2} + \dfrac{s}{Pe}\left(\dfrac{\partial^2 \hat{\phi}^{n+1}}{\partial z^2} - k_{i,j}^2\hat{\phi}^{n+1}\right) - \\
\qquad - \dfrac{Ch^2}{Pe}\left(k_{i,j}^4\hat{\phi}^{n+1} + \dfrac{\partial^4 \hat{\phi}^{n+1}}{\partial z^4} - 2k_{i,j}^2\dfrac{\partial^2 \hat{\phi}^{n+1}}{\partial z^2}\right)
\end{cases}
. \tag{2.89}
$$

The coefficient $k_{i,j}^2$ is the sum of the square of the corresponding wavenumbers: $k_{i,j}^2 = k_{x,i}^2 + k_{y,j}^2$. All terms, which are already known (current, n, and previous, $n-1$, time step), can be collected in a history term.

$$
H_x^n = \Delta t\left[\frac{3\hat{S}_x^n - \hat{S}_x^{n-1}}{2} + \frac{1}{2Re_\tau}\frac{\partial^2 \hat{u}^n}{\partial z^2} + \left(\frac{1}{\Delta t} - \frac{k_{i,j}^2}{2Re_\tau}\right)\hat{u}^n\right] \tag{2.90}
$$

$$
H_y^n = \Delta t\left[\frac{3\hat{S}_y^n - \hat{S}_y^{n-1}}{2} + \frac{1}{2Re_\tau}\frac{\partial^2 \hat{v}^n}{\partial z^2} + \left(\frac{1}{\Delta t} - \frac{k_{i,j}^2}{2Re_\tau}\right)\hat{v}^n\right] \tag{2.91}
$$

$$
H^n = \frac{\partial}{\partial z}(\iota k_{x,i}H_x^n + \iota k_{y,j}H_y^n) + k_{i,j}^2 H_z^n \tag{2.92}
$$

$$
H_\phi^n = \frac{\Delta t}{2}(3\hat{S}_\phi^n - \hat{S}_\phi^{n-1}) + \hat{\phi}^n \tag{2.93}
$$

Exploiting the history terms and taking the unknowns (time step $n+1$) at the left hand side, we obtain for each couple (i,j):

$$\begin{cases} \iota k_{x,i}\hat{u}^{n+1} + \iota k_{y,j}\hat{v}^{n+1} + \dfrac{\partial \hat{w}^{n+1}}{\partial z} = 0 \\ \hat{\omega}_z^{n+1} = \iota k_{x,i}\hat{v}^{n+1} - \iota k_{y,j}\hat{u}^{n+1} \\ \left(\dfrac{\partial^2}{\partial z^2} - \beta^2\right)\left(\dfrac{\partial^2}{\partial z^2} - k_{i,j}^2\right)\hat{w}^{n+1} = \dfrac{H^n}{\gamma} \\ \left(\dfrac{\partial^2}{\partial z^2} - \beta^2\right)\hat{\omega}_z^{n+1} = -\dfrac{\iota k_{x,i}H_y^n - \iota k_{y,j}H_x^n}{\gamma} \\ \left(\dfrac{\partial^2}{\partial z^2} - \beta_\phi^2\right)\left(\dfrac{\partial^2}{\partial z^2} - \beta_\phi^2\right)\hat{\phi}^{n+1} = \dfrac{H_\phi^n}{\gamma_\phi} \end{cases} . \tag{2.94}$$

The parameters γ, γ_ϕ and β, β_ϕ are defined as:

$$\gamma = \frac{\Delta t}{2Re_\tau} \quad , \quad \beta^2 = \frac{1+\gamma k_{i,j}^2}{\gamma} , \tag{2.95}$$

$$\gamma_\phi = \frac{Ch^2\Delta t}{Pe} \quad , \quad \beta_\phi^2 = \frac{s}{2Ch^2} + k_{i,j}^2 \tag{2.96}$$

Chebyshev-Tau method

The Chebyshev-Tau method is employed to solve all the independent problems for each Fourier wavenumber couple. This method can be applied to solve one-dimensional second order equations with mixed boundary conditions. The Chebyshev polynomials are chosen as test functions together with the weights $(1-z^2)^{-1/2}$. This choice allows to exploit the orthogonality of the polynomials.

$$\int_{-1}^{+1} T_j(z)T_k(z)\frac{1}{\sqrt{1-z^2}}\mathrm{d}z = \begin{cases} 0 & \text{if } j \neq k \\ \pi & \text{if } j = k = 0 \\ \pi/2 & \text{if } j = k \neq 0 \end{cases} \tag{2.97}$$

In total $N_z - 2$ test function are employed; the boundary conditions at $z = \pm 1$ close the problem.
The Chebyshev-Tau method will be now presented for a generic one-dimensional Helmholtz equation:

$$\frac{\partial^2 u}{\partial z^2} - \alpha^2 u = F . \tag{2.98}$$

The functions u and F can be written as truncated Chebyshev series:

$$u = \sum_{n=0}^{N_z-1} a_n T_n(z) , \tag{2.99}$$

$$F = \sum_{n=0}^{N_z-1} b_n T_n(z) . \tag{2.100}$$

The equation is then integrated twice in z from -1 to z. The following property of Chebyshev polynomials is exploited:

$$\int_{-1}^{z} \sum_{n=0}^{N_z-1} c_n T_n(s)\mathrm{d}s = \sum_{n=1}^{N_z} l_n T_n(z) \ . \tag{2.101}$$

The coefficients l_n can be expressed in terms of the coefficients c_n:

$$\begin{cases} l_n = \dfrac{1}{2(Nz-1)}(c_{n-1} - c_{n+1}) \quad \text{for } n = 1, \dots, N_z - 2 \\ l_{N_z-1} = \dfrac{c_{N_z-1}}{2(N_z-1)} \\ l_{N_z} = \dfrac{c_{N_z-1}}{2N_z} \end{cases} . \tag{2.102}$$

Upon integration over z twice we get:

$$\sum_{n=0}^{N_z-1} a_n T_n(z) - AT_1(z) - BT_0(z) - \alpha^2 \sum_{n=2}^{N_z+1} m_n T_n(z) = \sum_{n=2}^{N_z+1} f_n T_n(z) \ . \tag{2.103}$$

where the coefficients m_n and f_n are obtained exploiting twice Eq. (2.102). The coefficient A and B are:

$$A = \left.\frac{\partial u}{\partial z}\right|_{z=-1} \quad , \qquad B = \left.\frac{\partial u}{\partial z}\right|_{z=-1} + u(z=-1) \ . \tag{2.104}$$

To get a more compact notation the coefficient $h_n = a_n - \beta^2 m_n - f_n$ is introduced.

$$(a_0 - B)T_0(z) + (a_1 - A)T_1(z) + \sum_{n=2}^{N_z-1} h_n T_n(z) - \sum_{n=N_z}^{N_z+1} (\beta^2 m_n - f_n)T_n(z) = 0 \tag{2.105}$$

The Chebyshev-Tau method solves the differential equation in weak form, so the integral over the domain of the equation multiplied by a test function f must be zero for each test function. By choosing the Chebyshev polynomials $T_2, \dots, T_{N_z-1}$ as test functions with the weight $(1-z^2)^{-1/2}$, the orthogonality of Chebyshev polynomials can be exploited. The missing two equations are obtained from the boundary conditions:

$$p_1 \sum_{n=0}^{N_z-1} a_n T_n(-1) + q_1 \sum_{n=0}^{N_z-1} a_n \left.\frac{\partial T_n}{\partial z}\right|_{z=-1} = r_1 \ , \tag{2.106}$$

$$p_2 \sum_{n=0}^{N_z-1} a_n T_n(+1) + q_2 \sum_{n=0}^{N_z-1} a_n \left.\frac{\partial T_n}{\partial z}\right|_{z=+1} = r_2 \ . \tag{2.107}$$

In a more compact form, $d_n = p_1 T_n + q_1 \partial T_n/\partial z$ and $e_n = p_2 T_n + q_2 \partial T_n/\partial z$. Using the relation reported in Eq. (2.102) the coefficient m_n can be expressed as a linear

function of a_n coefficients, while f_n as a linear function of b_n; this way a linear system of equations for the unknown coefficents a_n is obtained.

$$\begin{bmatrix} d_1 & d_2 & d_3 & d_4 & d_5 & d_6 & d_7 & d_8 & ... & d_{N_z} \\ e_1 & e_2 & e_3 & e_4 & e_5 & e_6 & e_7 & e_8 & ... & e_{N_z} \\ s_1 & 0 & v_1 & 0 & t_1 & 0 & 0 & 0 & ... & 0 \\ 0 & s_2 & 0 & v_2 & 0 & t_2 & 0 & 0 & ... & 0 \\ 0 & 0 & s_3 & 0 & v_3 & 0 & t_3 & 0 & ... & 0 \\ \vdots & \vdots & \vdots & \vdots & \vdots & \vdots & \vdots & \vdots & \ddots & \vdots \\ 0 & 0 & 0 & 0 & 0 & 0 & 0 & 0 & ... & v_{N_z-2} \end{bmatrix} \begin{bmatrix} a_0 \\ a_1 \\ a_2 \\ a_3 \\ a_4 \\ \vdots \\ a_{N_z-1} \end{bmatrix} = \begin{bmatrix} r_1 \\ r_2 \\ g_1 \\ g_2 \\ g_3 \\ \vdots \\ g_{N_z-2} \end{bmatrix} \tag{2.108}$$

The coefficients of the matrix are:

$$s_{n-2} = -\alpha^2 n \qquad n = 3, \dots, N_z \,, \tag{2.109}$$

$$v_{n-2} = 4n(n-1)(n-2) + 2(n-1)\alpha^2 \qquad n = 3, \dots, N_z \,, \tag{2.110}$$

$$t_{n-2} = -\alpha^2 (n-2) \qquad n = 3, \dots, N_z - 2 \,, \tag{2.111}$$

$$g_n = \begin{cases} g_{n-2} = nb_{n-2} - 2(n-1)b_n + (n+2)b_{n+2} & n = 3, \dots, N_z - 2 \\ g_{N_z-3} = (N_z-3)b_{N_z-5} - 2(N_z-4)b_{N_z-3} & \\ g_{N_z-2} = (N_z-2)b_{N_z-4} - 2(N_z-3)b_{N_z-2} & \end{cases} . \tag{2.112}$$

The coefficient matrix has the first two rows full (from the boundary conditions) and from the third to the last (N_z) row is a tridiagonal matrix. This system can be readily solved using a Gauss-Jordan elimination algorithm followed by forward substitution. The Chebyshev-Tau method is applied to the fourth order equation for the velocity, the second order equation for the vorticity and the fourth order equation for the phase field. In the following it will be shown how to get from the problem equations to an Helmholtz form, as in Eq. (2.98). Then, the Chebyshev-Tau method applies to each Helmholtz-like equation as shown in the previous steps.

Boundary conditions

Due to the Fourier discretization in the streamwise and spanwise directions (x and y), periodic boundary conditions are implicitly enforced in these directions. A closed channel setup is being considered: two solid walls bound the channel at $z = \pm 1$ (dimensionless units). No-slip and no-flux boundary conditions are imposed on the flow field; at the wall the fluid moves with the same velocity of the wall.

$$\begin{cases} \mathbf{u}(x, y, z = \pm 1) = [u_w, v_w, 0] \\ \left. \dfrac{\partial w}{\partial z} \right|_{z=\pm 1} = 0 \end{cases} \tag{2.113}$$

For the shear flow setup u_w and v_w are respectively the x and y direction velocities of the moving wall. From the no-slip condition at the wall the boundary condition for the wall-normal component of the vorticity is obtained:

$$\omega_z(x, y, z = \pm 1) = 0 \, . \tag{2.114}$$

No-flux boundary conditions are enforced for the phase field. As the phase field transport equation is fourth order differential equation, two additional boundary conditions are needed; in particular, a no-flux boundary condition is imposed at the two solid walls also on the phase field chemical potential.

$$\begin{cases} \left.\dfrac{\partial \phi}{\partial z}\right|_{z=\pm 1} = 0 \\ \left.\dfrac{\partial^3 \phi}{\partial z^3}\right|_{z=\pm 1} = 0 \end{cases} \tag{2.115}$$

Solution of the velocity equation

The equation for the wall-normal velocity is fourth-order equation, thus the Chebyshev-Tau method cannot be directly applied. The equation is then split in two second order Helmholtz-like equations, so that the Chebyshev-Tau method can be applied to each of these second order equations.

$$\begin{cases} \dfrac{\partial^2 \theta^{n+1}}{\partial z^2} - \beta^2 \theta^{n+1} = \dfrac{H^n}{\gamma} \\ \dfrac{\partial^2 \hat{w}^{n+1}}{\partial z^2} - k_{i,j}^2 \hat{w}^{n+1} = \theta^{n+1} \end{cases} \tag{2.116}$$

Two separate differential problems are obtained for the wall-normal velocity $\hat{w}^{n+1}$ and the auxiliary variable $\hat{\theta}^{n+1}$; however, the physical boundary conditions apply only to the first problem (boundary conditions on the value of the velocity and its derivative at the wall). As there are no physical boundary conditions for the auxiliary problem, the influence matrix method has to be employed.
Using the influence matrix method, the solutions $\hat{w}^{n+1}$ and θ^{n+1} can be split in three contributions: a first contribution that does not necessarily verify the boundary conditions (w_1 and θ_1) and two contributions that verify the boundary conditions at one boundary (w_2, w_3 and θ_2, θ_3). A linear combination of these three contributions gives the solution $\hat{w}^{n+1}$ and θ^{n+1}.

$$\begin{cases} \hat{w}^{n+1} = w_1 + A w_2 + B w_3 \\ \theta^{n+1} = \theta_1 + A \theta_2 + B \theta_3 \end{cases} \tag{2.117}$$

The coefficients A and B have to be determined to obtain the value of the unknowns; the subproblems denoted by the subscript 1, 2 and 3 are second order differential equations with a unique solution. In particular the first subproblem, subscript 1, has a solution which does not necessarily satisfy the imposed boundary conditions; subproblem 2 verifies the boundary conditions at $z = -1$, while subproblem 3 verifies

the boundary conditions at $z = +1$. In the following the domain will be denoted as Ω, while its boundaries ($z = \pm 1$) as Γ.

$$[P_1] = \begin{cases} \dfrac{\partial^2 w_1}{\partial z^2} - k_{i,j}^2 w_1 = \theta_1 & \text{in } \Omega \\ w_1 = w_\Gamma & \text{in } \Gamma \\ \dfrac{\partial^2 \theta_1}{\partial z^2} - \beta^2 \theta_1 = \dfrac{H^n}{\gamma} & \text{in } \Omega \\ \theta_1 = \theta_\Gamma & \text{in } \Gamma \end{cases} \tag{2.118}$$

$$[P_2] = \begin{cases} \dfrac{\partial^2 w_2}{\partial z^2} - k_{i,j}^2 w_2 = \theta_2 & \text{in } \Omega \\ w_2 = 0 & \text{in } \Gamma \\ \dfrac{\partial^2 \theta_2}{\partial z^2} - \beta^2 \theta_2 = 0 & \text{in } \Omega \\ \theta_2(z=-1) = 1 \qquad \theta_2(z=+1) = 0 & \end{cases} \tag{2.119}$$

$$[P_3] = \begin{cases} \dfrac{\partial^2 w_3}{\partial z^2} - k_{i,j}^2 w_3 = \theta_3 & \text{in } \Omega \\ w_3 = 0 & \text{in } \Gamma \\ \dfrac{\partial^2 \theta_3}{\partial z^2} - \beta^2 \theta_3 = 0 & \text{in } \Omega \\ \theta_3(z=-1) = 0 \qquad \theta_3(z=+1) = 1 & \end{cases} \tag{2.120}$$

The boundary condition on $[P_1]$ is arbitrary; $w_\Gamma = 0$ and $\theta_\Gamma = 0$ were selected. The subproblem $[P_1]$ is time-dependent as the history term H^n changes over time; the solutions to subproblems $[P_2]$ and $[P_3]$ do not depend on time and are calculated only once.

The most general form of the boundary conditions on the wall-normal velocity is:

$$\begin{cases} p_1 \hat{w}^{n+1}(x,y,z=-1) + q_1 \left.\dfrac{\partial \hat{w}^{n+1}}{\partial z}\right|_{z=-1} = r_1 \\ p_2 \hat{w}^{n+1}(x,y,z=+1) + q_2 \left.\dfrac{\partial \hat{w}^{n+1}}{\partial z}\right|_{z=+1} = r_2 \end{cases} . \tag{2.121}$$

The variable $\hat{w}^{n+1}$ can be split in the three contributions, $\hat{w}^{n+1} = w_1 + A w_2 + B w_3$, and substituted in the boundary conditions. This way a linear system for the unknown coefficients A and B is obtained.

$$\begin{bmatrix} p_1 w_2(-1) + q_1 \left.\dfrac{\partial w_2}{\partial z}\right|_{z=-1} & p_1 w_3(-1) + q_1 \left.\dfrac{\partial w_3}{\partial z}\right|_{z=-1} \\ p_2 w_2(-1) + q_2 \left.\dfrac{\partial w_2}{\partial z}\right|_{z=-1} & p_2 w_3(-1) + q_2 \left.\dfrac{\partial w_3}{\partial z}\right|_{z=-1} \end{bmatrix} \begin{bmatrix} A \\ B \end{bmatrix} = \begin{bmatrix} \widetilde{r}_1 \\ \widetilde{r}_2 \end{bmatrix} \tag{2.122}$$

The right hand side is given by:

$$\begin{bmatrix} \widetilde{r}_1 \\ \widetilde{r}_2 \end{bmatrix} = \begin{bmatrix} r_1 - p_1 w_1(-1) - q_1 \left.\dfrac{\partial w_1}{\partial z}\right|_{z=-1} \\ r_2 - p_2 w_1(-1) - q_2 \left.\dfrac{\partial w_1}{\partial z}\right|_{z=-1} \end{bmatrix} . \tag{2.123}$$

Once obtained the unique solutions w_1, w_2 and w_3 from the three subproblems and calculated the unknown parameters A and B, the unknown wall-normal velocity $\hat{w}^{n+1}$ is obtained.

The complete flow field is determined once the wall-normal velocity and vorticity are known; using the continuity equation and the definition of the wall-normal vorticity the values of $\hat{u}^{n+1}$ and $\hat{v}^{n+1}$ are obtained.

$$\begin{bmatrix} -\imath k_{y,j} & \imath k_{x,i} \\ \imath k_{x,i} & \imath k_{y,j} \end{bmatrix} \begin{bmatrix} \hat{u}^{n+1} \\ \hat{v}^{n+1} \end{bmatrix} = \begin{bmatrix} \hat{\omega}_z^{n+1} \\ -\dfrac{\partial \hat{w}^{n+1}}{\partial z} \end{bmatrix} \tag{2.124}$$

This method however fails when the determinant of the matrix of coefficients is zero; this occurs for $k_{i,j}^2 = 0$, so for $k_{x,i} = 0$ and $k_{y,j} = 0$. These wavenumbers correspond to the mean modes in the x and y direction. The solution for the mean mode of u and v can be calculated starting from the fourth order equation Eq. (2.78) and substituting $k_{x,0} = 0$ and $k_{y,0} = 0$. This way, two second order equations for $\hat{u}^{n+1}$ and $\hat{v}^{n+1}$ are obtained.

$$\begin{cases} \dfrac{\partial^2 \hat{u}^{n+1}}{\partial z^2} - \dfrac{\hat{u}^{n+1}}{\gamma} = -\dfrac{H_x^n}{\gamma} \\ \hat{u}(z = \pm 1) = u_w \end{cases} \tag{2.125}$$

$$\begin{cases} \dfrac{\partial^2 \hat{v}^{n+1}}{\partial z^2} - \dfrac{\hat{v}^{n+1}}{\gamma} = -\dfrac{H_y^n}{\gamma} \\ \hat{v}(z = \pm 1) = v_w \end{cases} \tag{2.126}$$

Solution of the vorticity equation

The equation for the wall-normal vorticity is already a one-dimensional second order Helmholtz equation, thus it does not require any particular treatment.

$$\begin{cases} \dfrac{\partial^2 \hat{\omega}_z^{n+1}}{\partial z^2} - \beta^2 \hat{\omega}_z^{n+1} = -\dfrac{\imath k_{x,i} H_y^2 - \imath k_{y,j} H_x^n}{\gamma} \\ \hat{\omega}_z(z = \pm 1) = 0 \end{cases} \tag{2.127}$$

The Chebyshev-Tau method can be readily applied to get the new vorticity value.

Solution of the phase field equation

The fourth order equation for the phase field is split in two subproblems, one for the phase field and one for the auxiliary variable $\hat{\theta}^{n+1}$.

$$\begin{cases} \dfrac{\partial^2 \hat{\phi}^{n+1}}{\partial z^2} - \beta_\phi^2 \hat{\phi}^{n+1} = \theta^{n+1} \\ \left.\dfrac{\partial \hat{\phi}^{n+1}}{\partial z}\right|_{z=\pm 1} = 0 \end{cases} \tag{2.128}$$

$$\begin{cases} \dfrac{\partial^2 \theta^{n+1}}{\partial z^2} - \beta_{\hat{\phi}}^2 \theta^{n+1} = \dfrac{H_\phi^n}{\gamma_\phi} \\ \left.\dfrac{\partial \theta^{n+1}}{\partial z}\right|_{z=\pm 1} = 0 \end{cases} \tag{2.129}$$

Here, as both problems have physical boundary conditions, the influence matrix method is not needed and the two subproblems can be directly solved. First, the problem for $\hat{\theta}^{n+1}$ is solved, then the phase field is calculated.

Solution of the Lagrangian equation of motion

As far as the Lagrangian tracking is concerned, the particle equations of motion are integrated in time using an explicit Euler scheme. Particles are injected into the flow once the surface area of the drops has reached a steady state: Particles are initially placed at random locations within the volume occupied by the carrier fluid, namely in regions of the flow where $\phi_{@p=-1}$ to avoid direct injection inside a drop, with initial velocity $\mathbf{u}_p(\mathbf{x}_p, t_{tr} = 0) = 0$, t_{tr} being the particle tracking time. Interpolation of flow variables (in particular fluid velocity components and phase field) at particle position is performed using 6th-order Lagrange polynomials.

2.6 Code implementation

The numerical algorithm presented has been implemented in a in-house code using Fortran as programming language. The code is parallelized using a pure-MPI (Message Passing Interface) approach. In this parallelization, the global communicator is splitted to 3 sub-communicators:

1. Flow-communicator: A communicator to solve the Eulerian field; the paralleliztion in this communicator is based on MPI distributed memory.

2. Particle-communicator: A communicator to solve the Lagrangian field; the paralleliztion in this communicator is based on MPI shared-memory

3. Comm-communicator: A communicator to communicate between flow-communicator and particle-communicator.

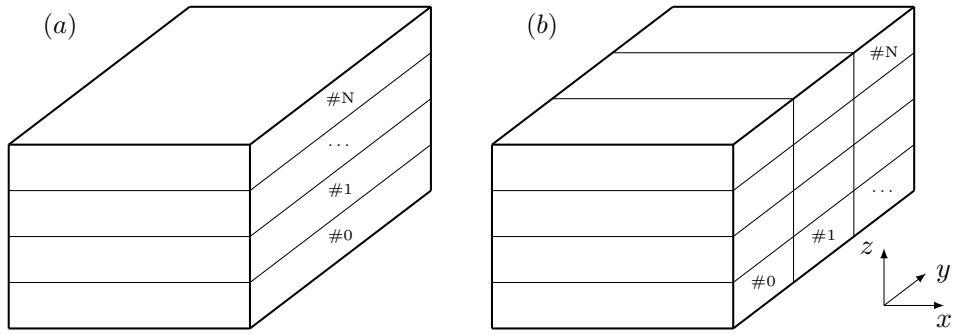

FIGURE 2.7 – Slab, panel (a), and pencil, panel (b), decomposition of the computational domain in physical space. The numbering of the tasks, #0, #1, ..., #N, is reported for reference.

Flow solver in flow-communicator

The overall workload is divided among the MPI tasks using a 2D domain decomposition. With this strategy the whole domain is splitted in so-called pencils: the domain is divided along two out of three directions and each sub-domain is assigned to a different MPI process.

The 2D partitioning constitutes an improvement with respect to the 1D decomposition (slab decomposition), in which the computational domain is partitioned along only one direction out of three; a graphical visualization of these domain partitioning approaches is reported in Fig. 2.7. While on one hand the pencil decomposition increases the volume of data communication among the tasks and slightly increases the replication of data across the variable space of different tasks (parameters, constants, ...), on the other hand it greatly increases the maximum number of tasks that can be used to divide the workload.

The maximum number of tasks is limited by the number of grid points: for a grid with $\mathcal{O}(N^3)$ points, the maximum number of tasks for the slab decomposition is $\mathcal{O}(N)$, while for the pencil decomposition is $\mathcal{O}(N^2)$. This limitation occurs as the minimum size of a slab is $N \times N \times 1$, while for a pencil it is $N \times 1 \times 1$: each subdomain must include at least one grid point in each direction. The pencil decomposition thus overcomes the limitation of the maximum number of tasks that could be employed; in addition it also shows better performances even at low numbers of tasks, Fig. 2.8. A loss of performances for increasing number of MPI tasks can be observed in Fig. 2.8 for the coarse and intermediate grids: in these cases the number of grid points held by each task becomes too low ($\mathcal{O}(8k)$ points per task for the coarse grid and $\mathcal{O}(33k)$ for the intermediate one). As the number of grid points per task is too low, the time spent in communications among tasks overcomes the time spent in actual calculations, reducing the overall performances of the code.

In physical space, the domain is divided along the y and z directions, while in modal space it is divided along the x and y directions. This change in the parallelization is needed when taking the transforms: to compute the Fourier or Chebyshev transforms each process must hold all the point in the transform direction. Therefore, when in physical space, first Fourier transforms are taken along the x direction, second the

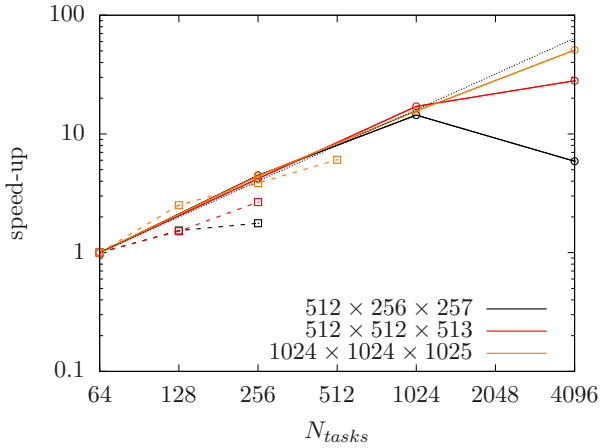

FIGURE 2.8 – Comparison between slab (dashed lines with square markers) and pencil (solid line with circle markers) decomposition for different grid sizes. The speed-up with respect to a reference case on 64 tasks is shown; the ideal scaling is reported with a thin black dotted line. The pencil decomposition achieves better performances than the slab decomposition even at low numbers of tasks. The loss of performances for increasing number of tasks can be appreciated for the coarser grid, $N_x \times N_y \times N_z = 512 \times 256 \times 257$. Performance results were obtained on the Broadwell (BDW) partition of the HPC system Marconi hosted at CINECA (Bologna, Italy).

parallelization changes in order to have all the points in the y direction. The domain is thus divided along the x and z directions when taking the Fourier transforms along y. At this point each $x-y$ plane holds all the Fourier modes at a certain height. Then the parallelization is changed again, switching to a domain division along x and y directions, so that each MPI process handles all the points in z direction at a certain (x, y) location (parallelization in modal space). Finally, Chebyshev transforms are taken in the z direction. Indeed, in modal space the computational domain is divided along the x and y directions (each task holds all the points in the wall-normal direction). The transform from physical to modal space thus requires: (i) one-dimensional Fourier transforms (x direction), (ii) pencil transposition, (iii) one-dimensional Fourier transforms (y direction), (iv) pencil transposition and (v) one-dimensional Chebyshev transforms (z direction). The transform from modal to physical space follows the same path backwards. This process is thus constituted of intensive computation phases (Fourier and Chebyshev transforms) interleaved with MPI communications among the various tasks. A MPI Cartesian communicator is adopted to easily define the communication pattern. Fast Fourier and Chebyshev transforms are taken using the functions provided in the library *FFTW* (version 3.3.8) by Frigo and Johnson [43]. This domain partitioning choice gives the best performances: MPI communications occur only during transforms from physical to modal space (and backwards) and, in modal space, each task solves a series of Helmholtz problems (all Helmholtz problems are independent one from each other). Most of the transforms occur during the calculation of non-linear terms: to avoid the costly calculation of convolution integrals, products of variables are computed in physical space, then the result is transformed in modal space (pseudo-spectral method).

Lagrangian solver in particle-communicator

A standard tracking routine will be used in which different inertial particles are included in a single equation for the time evolution, which is solved in the limit of one-way coupling between the phases. Time integration is explicit Euler scheme. Particle collisions will be treated using a standard deterministic hard sphere collision model, based on the following assumptions; The particles are divided equally among the processes in particle-communicator, each process is responsible for its particles and tracks it from the beginning of the simulation up to the last time-step. After solving the flow filed in "flow-communicator", "particle-communicator" and "flow-communicator" communicate through "comm-communicator" and the Eulerian field is placed on the shared memory of this latter communicator. As a consequence, each rank has direct access to the flow filed and can compute the particle trajectory based on the velocity and phase variable interpolated at the particle position. If the calling process needs the position and velocity of another particle (which belongs to another processes), as may happen in the case of particle-particle collision, instead of data communication (send-receive) to pass the particle data, the calling process has the direct access to the information of the whole particle in the shared memory.
Finally, The input and output of large files (initial fields, restart fields and solution fields) are performed using the MPI I/O subroutines from the MPI library, so that each MPI process reads and writes only its part of the domain, without either writing separate files (one for each process) or communicating all the data to a single process. We believe that this strategy allows for better performances as only one file is written for each process and there are no MPI communications of large chunks of data, which for large simulations could not even fit in the available memory of a node. The performances of the code were measured on several High Performance Computing (HPC) machines.

The outline of the code is as following:

1. MPI initialization
2. Split the global communicator to three sub-communicators and numbering the MPI processes in each
3. Reading of input file, initialization of parameters
4. Creation of Cartesian communicator in flow-communicator, used to communicate through the processes in flow-communicator. Initialization of variables in physical space and transformation to wave space
5. Saving of variables in physical and in wave space
6. Do loop for time advancement with call to flow solver
7. Communicate the flow field between particle-communicator and flow-communicator through comm-communicator
8. Do loop for time advancement with call to particle solver

9. Saving of Eulerian variables in physical and/or in wave space and Lagrangian variable in physical space
10. Deallocation of all allocated arrays, freeing all the communicators
11. MPI finalize

3

Particle capture by drops in turbulent flow

Reproduced in part from:
A. Hajisharifi, C. Marchioli and A. Soldati, *Particle capture by drops in turbulent flow*, Physical Review Fluids **6**, Article N. 024303, 2021

In this chapter, the process of particle capture will be investigated. Particular matters which are generally generated in the combustion of coal and petroleum, construction industry, industrial production and transport assignment causes serious pollution issue due to its perniciousness for the ecological environment and human healthiness. The increasing emission of particular matter encourage us to pay much more attention to the control and removal of these pollutants[25, 81, 156]. This problem is the subject of wide range of industrial and environmental applications, among which wet scrubbing [64, 100, 90], electrostatic scrubbing [31, 132], froth flotation processes [94, 143, 93] This study is motivated by the need of developing the models and correlations predicting the transfer rate across the interface. These models can be then used in industrial-oriented CFD tools to predict the capture efficiency of the full-scale equipment.[48, 107].

Most of the 3-phase models available in the literature were used to study the dynamics of a single particle trapped at a planar fluid interface [89], or the surface stress tensor modification for a pendant drop covered by a monolayer of particles in the low-Reynolds-number limit [50], but do not consider the large swarms of particles and droplets in turbulent flow conditions that affects droplet coalescence/breakup as well as particle spatial distribution that is the focus of our study. The coherent fluid motions bring the particles toward the interface region and deform the drop surface in the same time changing the flow topology surrounding each drop. The change in the topology of flow will play an important role in the particle adhesion process. This role is examined by analysis the fluid motion in the interface vicinity.

We will first characterize the process of particle capture at the drop interface, focusing in particular on the topology of the flow structures that drive particle adhesion. Then, we will discuss the macroscopic outcome of this process, the time accumulation

of particles on the interface and propose a simple model to estimate the rate at which this accumulation takes place.The findings in this chapter confirm that what actually controls the process of particle capture is local turbulent fluctuations in near-interface regions.

3.1 Simulation setup

The flow is driven by a constant pressure gradient imposed along the streamwise direction, at shear Reynolds number $Re_\tau = 150$ (corresponding to a Reynolds number $Re_H \simeq 9,000$ based on the hydraulic diameter). This value of the Reynolds number was chosen in view of the computational cost required to simulate the targeted three-phase system, characterized by a marked separation between the large scales in the bulk of the flow with the small scales generated near the deformable interface. Clearly, the complete and accurate numerical resolution of all the scales down to the interface thickness is beyond the current computational limits. To reproduce these scales with adequate accuracy, the grid resolution has to be much finer than that required by a single-phase flow [127]. Considering also that we must account for a third phase, we decided to choose a relatively low value of Re_τ, yet sufficient to produce a fully-turbulent flow field [32, 73, 86]. Even at this low value of Re_τ, the entire simulation campaign required large amount of cpu-hours on a large scale parallel infrastructure.

In this study we assume the two Eulerian phases, namely the carrier fluid (denoted by subscript f) and the drops (denoted by subscript d), to have matched density ($\rho = \rho_f = \rho_d$) and matched viscosity ($\eta = \eta_f = \eta_d$). From an applicative point of view, the matched-density assumption appears to be fully justified by the fact that we are interested in a liquid-liquid dispersion while the matched-viscosity assumption appears to be relevant for situations in which the two fluids are water and low-viscosity silicone oil. For different combinations of immiscible fluids, the difference in viscosity would influence drop breakup and coalescence, thus introducing an additional complexity into the problem. As shown by [110], drops coalesce and break following a complex dynamics that are primarily controlled by the interplay between turbulence fluctuations (measured by the Reynolds number), surface tension (measured by the Weber number), and the viscosity ratio. Qualitatively, an increase in drop viscosity decreases the break-up rate, very much like an increase of surface tension does. However, a steady-state in the number of drops is always achieved regardless of the viscosity difference.
According to these assumptions, the dimensionless Navier-Stokes equation introduced in previous chapter Eq. (2.62) read as

$$\frac{\partial \mathbf{u}}{\partial t} + \mathbf{u} \cdot \nabla \mathbf{u} = -\nabla p + \frac{1}{Re_\tau} \nabla^2 \mathbf{u} + \frac{Ch}{We} \frac{3}{\sqrt{8}} \nabla \cdot \tau_c \quad , \tag{3.1}$$

The computational domain consists of a closed-channel configuration with dimensions $L_x \times L_y \times L_z = 4\pi h \times 2\pi h \times 2h$ ($L_x^+ \times L_y^+ \times L_z^+ = 1885 \times 942.5 \times 300$ in wall units). This

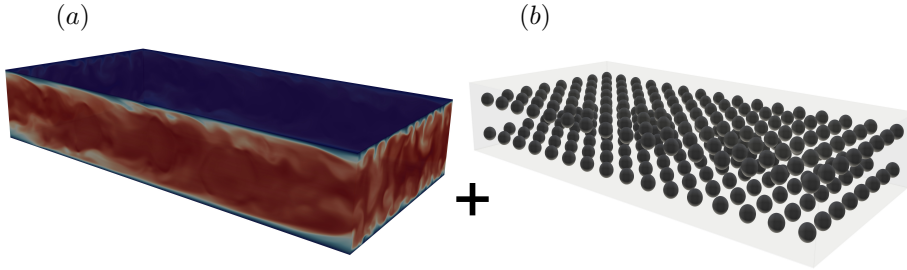

FIGURE 3.1 – Injection of droplets into a single-phase flow system. Panel(a) shows a fully developed turbulent channel flow at $Re_\tau = 150$, a regular array of 256 droplets with diameter $d^+ = 60$, panel(b), is injected in turbulent channel flow.

domain is discretized using $N_x \times N_y \times N_z = 512 \times 256 \times 257$ grid points, which provide an extremely-well resolved turbulent flow field compared to the single-phase case (grid spacings are $\Delta x^+ = \Delta y^+ = 3.7$, $\Delta z^+_{wall} = 0.0113$ and $\Delta z^+_{center} = 1.84 \simeq \eta^+_{K,center}/2$, with $\eta^+_{K,center}$ the Kolmogorov length scale in the channel center) and has proven sufficient to describe the near-interface scales [127].

We considered two different values of the surface tension corresponding to $We_L = 0.75$ and $We_H = 1.5$, respectively. These values match those commonly found in oil-water mixture [139]. In Sect. 3.2, the simulation results are discussed with reference to We_L, which corresponds to less deformable drops. However, we remark here that the effect of the Weber number observed in our simulations is limited to minor quantitative modification of the statistics examined. For the phase field, the value of the Cahn number has been set to ensure that there are at least five grids points across the interfacial layer to resolve accurately all the gradients occurring there [125, 127]. This condition yields $Ch = 0.02$. The Péclet number has been set according to the scaling $Pe_\phi = 1/Ch = 50$ proposed by [84] to achieve the convergence to the sharp interface limit.

At the beginning of the simulations, the phase field was initialized to generate a regular array of 256 spherical drops with normalized diameter $d/h = 0.2$ (corresponding to $d^+ = 60$ in wall units) that are injected in a fully-developed turbulent flow Fig. 3.1.

We remark here that the total mass of the carrier fluid and of the drops is conserved at all times, yet mass conservation of each phase is not guaranteed. To limit inter-phase mass leakage, we adopted the flux-corrected formulation proposed by [79, 154, 126]. In the simulations discussed here, this formulation limits mass leakage to roughly 5% of the drops during the initial time transient. At steady state, namely when the particles are also injected into the flow (Will be explained in detail below), mass leakage vanishes.

A total of five sets of $\mathcal{N}_p = 10^6$ particles at varying Stokes number were tracked individually: Tracer particles ($St = 0$), which are used as markers to sample all flow regions in the carrier fluid domain, and particles with $St = 0.1$, 0.2, 0.4 and 0.8, corresponding to particle diameters much smaller than the drop diameter - $d_p/d \simeq$

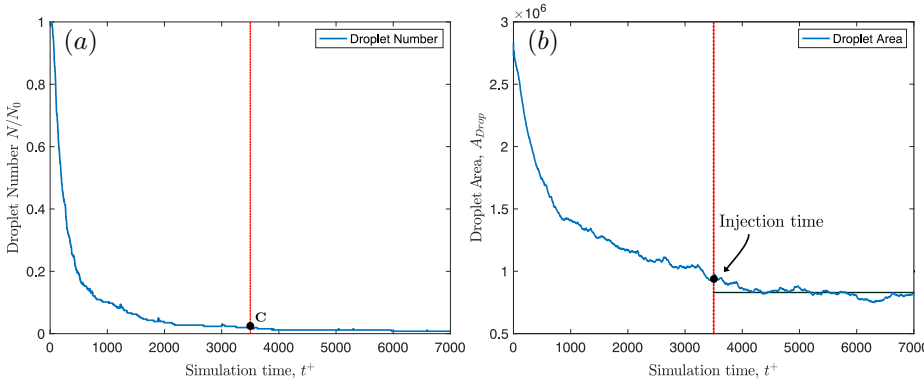

FIGURE 3.2 – Time evolution of droplet area and droplet number for two-phase flow simulation in which 256 spherical droplets are injected to a fully developed turbulent channel flow at shear Reynolds number $Re_\tau = 150$. Panel (a) shows the droplet area in time, panel b demonstrate droplets number in time (N) normalized by the initial droplet numbers(N_0). The droplets tend to coalesce as the consequence of coalescing regime , thus the droplets number and the surface area decrease in time, reach to statistically steady-state after $t+ = 3500$, labeled as **C** in panel (a). This is the point where the particles are injected to the carrier phase and the system becomes three-phase flow.

$\mathcal{O}(10^{-2})$ at least ($d_p^+ = 1.35, 1.9, 2.7, 3.8$ wall unit, respectively).
Before particles are distributed in the flow field, a two-phase flow simulation has been conducted in which 256 droplets are injected to the carrier phase for a period of time $t^+ = 7000$. The particles are then injected into the carrier phase and outside of the droplets, where the phase field sampled at particle position equals to -1 ($\phi_{@p} = -1$), only when the equilibrium condition of the surface area and droplets number is reached. Fig. 3.2a and Fig. 3.2b show the droplets number in time normalized by the initial droplets number $N_0 = 256$ and the surface area of droplets in time, respectively. The droplets may coalesce and breakup due to the effect of turbulence in this flow. In particular, for the Weber number considered in this study, the coalescing regime is dominated and the initial droplets number decreases in time Fig. 3.2a. Roccon et al. [109] have shown that N/N_0 decreases sharply in time for the same Weber number, indicating a strong predominance of coalescence over breakup events with the consequent formation of a few large drops.

But at a certain time it reaches to equilibrium, after $t^+ = 3500$ labeled as C, which results from a balance between coalescence and breakup events; Subsequently, the surface area of the droplets reaches to statistically-steady state Fig. 3.2b.

The reason for this initial condition is that the surface area clearly is an important parameter of the problem. The more surface area there is, the more particle can be adsorbed Fig. 3.3 .

In the following, only results for the smallest and largest Stokes number will be shown since all the observables investigated exhibit a monotonic dependence on St. The initial particle distribution is random in the carrier phase with zero initial velocity .

Since the focus of the present study is on particle capture by turbulence, and given that the average particle volume fraction is $\Phi_V \sim \mathcal{O}(10^{-4})$, the feedback of particles on the flow field is not considered (one-way coupling simulation). Particles are char-

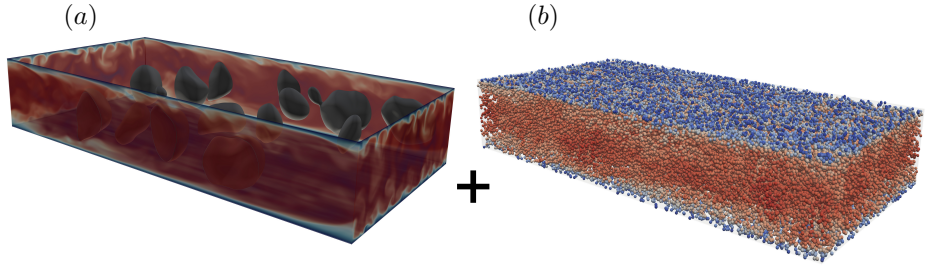

FIGURE 3.3 – Particle injection into a two-phase flow system. Panel(a) shows a fully developed turbulent channel flow with the droplets in equilibrium condition in which $\mathcal{N}_p = 10^6$ particles are injected, panel(b).

acterized by low values of inertia and exhibit a weak tendency to cluster before being captured at the interface: This keeps the volume fraction low also locally, leading to a spatial distribution within the carrier fluid domain that remains dilute over the entire simulation. The neglect of two-way coupling effects is further justified in view of the low momentum that the neutrally-buoyant particles can exchange with the fluid as compared to heavy particles. For the same reasons (low inertia and low volume fraction), particle-particle collisions are not accounted for: these are assumed to be negligible prior to particle adhesion to the drop interface and are expected to play a role only during the subsequent trapping stage, when particles are bound to move on a two-dimensional surface.
As explained in Chap. 2, the value of the parameter $\mathcal{A}$ is chosen to satisfy the condition that the adsorption energy $E_{ads} = \pi\sigma r^2(1 - |\cos\theta|)^2$, balances the desorption energy $E_{des} = \frac{1}{2}\mathcal{A}\pi\sigma r^2$, corresponding to the energy required for particle detachment from the interface [41, 51]. These expressions for E_{ads} and E_{des} are exact for an isolated, chemically homogeneous spherical particle on a flat surface [51]. Assuming a contact angle $\theta = 90^o$, this balance yields $\mathcal{A} = 2$, which is the value used in our simulations. Additional runs for different values of $\mathcal{A}$ (specifically: $\mathcal{A} = 0.01$ and 0.1) were also performed to assess the effect of a change in the magnitude of $\mathbf{F}_c$ on the capture process. As far as the statistical quantities discussed are concerned, no major effect was observed (small quantitative modifications).

3.2 Result and discussion

In this Section, we characterize the process of particle capture at the drop interface, focusing in particular on the topology of the flow structures that drive particle adhesion. we will first analyze this process from a qualitative view point, visualizing the instantaneous flow field in which a capture event is highlighted. The obtained physical intuition will be then verified by statistical tools to characterize the flow topology in

near drop region; using surface divergence in Subsect. 3.2.2 and topology parameter in Subsect. 3.2.3 enables us to demonstrate the mechanism that brings the particles to the drop surface thus leading to particle capture. Then, we will discuss the macroscopic outcome of this process, the time accumulation of particles on the interface. A simple model is proposed in Subsect. 3.2.4 to estimate the capture rate based on the similarity between the process examined here and the process of particle deposition at solid walls in turbulent flow [42, 20, 23]. The aim of this model is to provide a usable tool for industrial CFD codes.

3.2.1 Particle capture and flow topology

A qualitative rendering of the instantaneous flow field is provided in Fig. 3.4, where a close-up view of one capture event is also shown. The carrier phase is rendered by means of the fluid streaklines. Drops are visualized by the $\phi = 0$ iso-surface and are coloured by the local curvature of the surface (concave areas with high negative curvature are shown in blue, convex areas with high positive curvature are shown in red). Particles are represented as blue dots, with size equal to the particle diameter ($St = 0.1$ particles are considered here). Note that, after capture, particles remain trapped on the interface and tend to form filamentary clusters, which result from the action of the capillary force $\mathbf{F}_c$. The mechanisms that lead to the formation of these clusters and their topological characterization is the subject of next chapter focusing on particle dynamics after capture and will be explained in Chap. 4. It suffices to say here that the formation of neat particle filaments is favoured by the neglect of inter-particle collisions, which are expected to smear out densely-concentrated clusters.
Two close-up views are provided: One (marked as I) shows a near-drop region of the flow populated by a swarm of particles that is being pushed toward the drop by the carrier fluid, the other (marked as II) shows one isolated particle approaching the interface with the order parameter distribution in background. On the right end of the inset, this distribution (red line) is qualitatively compared with the distribution of the capillary force over the interaction distance $\mathcal{D}$: This force is zero everywhere except within a distance $\mathcal{D}$ from the interface, where its absolute value follows the blue line.
At this time of the simulation, the total surface area of the drops has reached a statistically-steady state that results from a balance of (now rare) coalescence and breakup events. Drop deformation induced by turbulence is apparent and is associated to a non-uniform distribution of the curvature, which can be computed starting from the phase field as

$$\kappa = -\nabla \cdot \left(\frac{\nabla \phi}{|\nabla \phi|} \right) = -\frac{\nabla^2 \phi}{|\nabla \phi|} + \frac{1}{|\nabla \phi|^2} \nabla \phi \cdot \nabla (|\nabla \phi|) \quad . \tag{3.2}$$

In addition, the local unit vector $\mathbf{n}$ normal to each level-set curve is obtained as

$$\mathbf{n} = -\frac{\nabla \phi}{|\nabla \phi|} \quad , \tag{3.3}$$

where equations (3.2) and (4.5) are valid only if ϕ iso-surfaces are parallel to each other. This property is conserved when advecting ϕ through the Cahn-Hilliard equation using the $Pe \propto Ch^{-1}$ scaling [84].

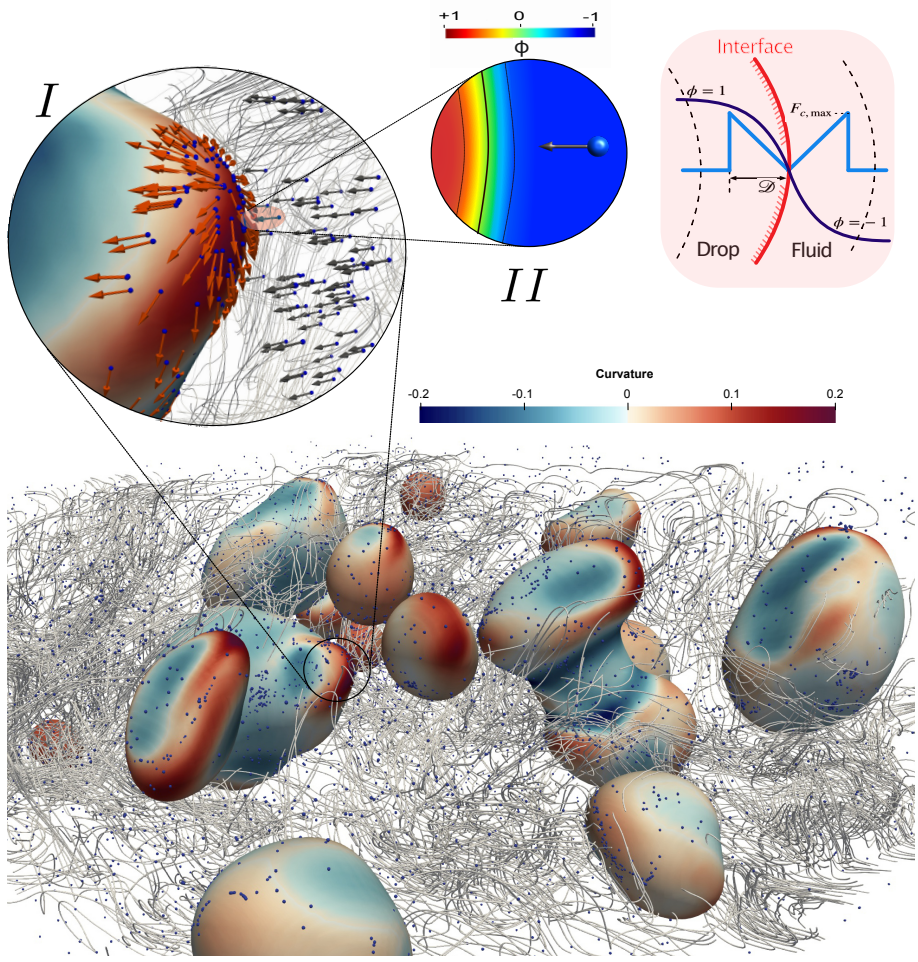

FIGURE 3.4 – Qualitative rendering of the flow configuration. Drops are coloured by the local curvature of the interface, the flow field is rendered by the fluid streaklines and particles are visualized as blue spheres. The insets provide close-up views of one particle capture event (inset I) and of one interface-approaching particle in isolation (inset II), respectively. Grey arrows represent the particle velocity magnitude and render the motion of particles that move towards the interface. Red arrows represent the interfacial stress sampled by the particles at the time of adhesion. The colormap in the top inset shows the spatial distribution of the order parameter ϕ: The interface is located at $\phi = 0$ (thick black line). The thin black lines represent the fluid layer within which Φ transitions from $\phi = -1$ (fluid) to $\phi = +1$ (drop) as shown in the schematic on the right end of the inset, where the distribution of the capillary force F_c over the interaction distance $\mathcal{D}$ is also rendered. Note that $\mathcal{D}$ is shorter than the distance over which $-1 < \phi < +1$.

Focusing on inset I, we observe that particles tend to approach the drop and adhere to its surface in a convex region of the interface where curvature κ reached a local peak. In this region, the flow is impinging on the drop surface and the tangential shear stress is directed from the high-positive curvature region towards the neighbouring, high-negative curvature regions. This anticipates that captured particles, while subject to the action of tangential stresses, will be driven toward such regions as long as they remain attached to the interface.
Fig. 3.4 confirms the physical intuition that particles are brought in close proximity of the drop by coherent fluid motions that interact with the compliant drop surface. This interaction gives rise to highly non-uniform curvature and shear stress distributions. In order to examine these fluid motions in more detail, we consider first the two-dimensional fluid velocity divergence at the interface of the drop, referred to as surface divergence and then, flow topology parameter in the following.

3.2.2 Surface divergence

Surface divergence is a tool allowing us to discriminate the regions of source of velocity and sink of velocity over the interface: sinks are characterized by negative value of surface divergence, while source by positive values. The surface divergence of velocity over the interface is defined as:

$$\nabla_{2D} = \mathbf{n} \cdot \nabla \times (\mathbf{n} \times \mathbf{u}) \quad . \tag{3.4}$$

where $\mathbf{n}$ is the unit-length vector normal to the interface.
According to this definition, particles captured at the surface probe a compressible two-dimensional system where regions of local flow expansion, generated by impinging fluid motions, are characterized by $\nabla_{2D} > 0$ and regions of local compression, generated by outward fluid motions, are characterized by $\nabla_{2D} < 0$ Fig. 3.5.
In Fig. 3.6, we show the probability distribution function (PDF) of the surface divergence computed at the position occupied by the particles when they get captured by the interface. This position is evaluated at the time the particle touches the interface, namely when the particle center is less than one radius away from the nearest zero-level point on the interface.

To allow comparison among the different particle sets, we considered a reference distance equal to the radius of the largest particles ($St = 0.8$), which is equal to about one tenth of the interface thickness and thus corresponds to a phase field $\phi = -0.71$. The PDFs for the $St = 0.1$ and $St = 0.8$ are shown, and compared to the PDF obtained for the case of inertialess tracers uniformly distributed over the $\phi = -0.71$ iso-surface. We remark that, in our simulations, this is also the distance within which the capillary force $\mathbf{F}_c$ starts acting on the particle. Therefore, the PDFs shown in Fig. 3.6 is not affected by the model used for $\mathbf{F}_c$ in the equation of particle motion.
Fig. 3.6 shows that, in the case of the tracers, the PDF exhibits a clear peak at $\nabla_{2D} = 0$ but is also negatively skewed. This indicates that fluid motions directed towards the drop occupy a wider surface area as compared to fluid motions directed away from the drop. The effect can be ascribed to the deformability of the interface,

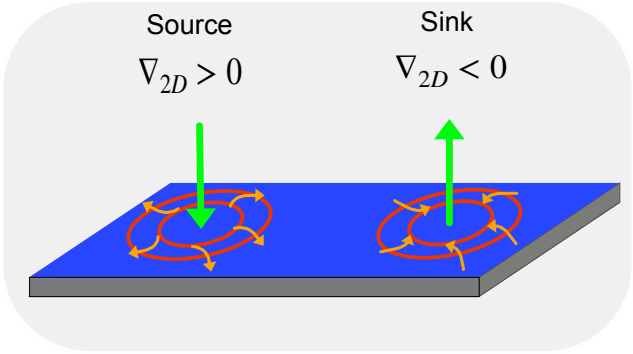

FIGURE 3.5 – schematic visualization of sink and source region on a $2D$ surface. The impinging fluid motions on the surface generate the regions of source of velocity corresponds to positive surface divergence ($\nabla_{2D} > 0$), while the outward motions of the fluid generate the sink regions that is characterized by the negative value of the surface divergence ($\nabla_{2D} < 0$).

which is able to respond and adapt *elastically* to impinging flow events. In the case of particles with tiny inertia, the PDF shifts towards higher positive values of ∇_{2D}: The peak is now located at $\nabla_{2D} \simeq 1$, and inertia appears to play a negligible role for the range of Stokes numbers considered in the study. Overall, Fig. 3.6 corroborates the observation that particles tend to sample preferentially the regions of local flow expansion as they attach to the drop. This provides already a first indication about the topological features of the flow near the interface.

3.2.3 Topology parameter

To provide additional information about mentioned features, we examine next the flow topologies that are sampled by the particles just before being captured. A flow topology analysis near deformable drops has been carried out recently by [39] for the case of decaying isotropic turbulence. Following the classification proposed by [98] (to which the reader is referred to for a detailed discussion of the flow topologies in three-dimensional flow fields), these Authors showed that there is a shift from high-enstrophy/low-dissipation structures favoured outside the near-surface viscous layer to low-enstrophy/high-dissipation structures favoured inside the viscous region and, eventually, to boundary-layer like and vortex-sheet flow topologies at the surface. In close proximity of the surface, the observables examined to characterized the topological structures (the invariants of the velocity-gradients, rate-of-strain and rate-of-rotation tensors) exhibit statistical features that are very similar to those reported inside the viscous sublayer of wall-bounded turbulence [39, 103]. The analysis we propose is thus justified by the expectation that the final particle capture rate will result from particle interaction with all these topological structures.
To infer the local flow structures sampled by the particles, we use standard observables that are related to the invariants of the velocity gradients tensor $\mathcal{A} = \nabla u$, with

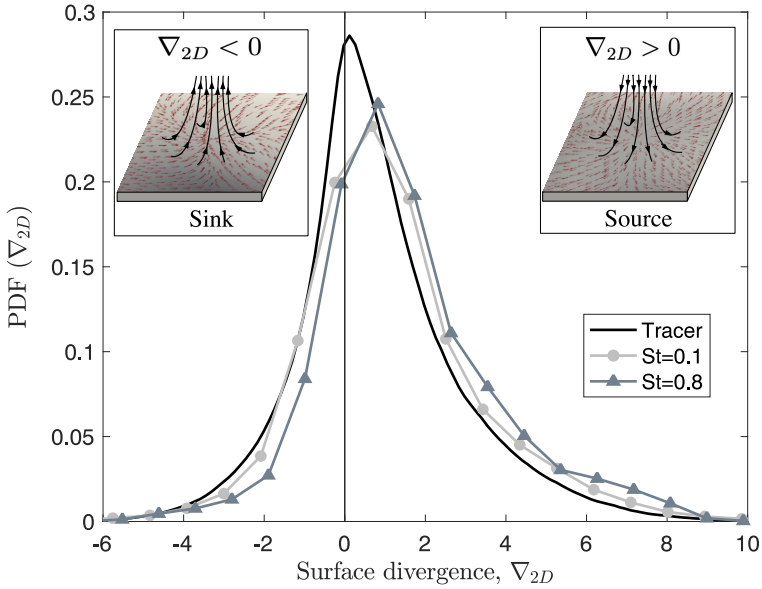

FIGURE 3.6 – PDF of the 2D surface divergence, ∇_{2D}, seen by the particles when they get captured by the interface. Regions of local flow expansion (velocity sources) are characterized by $\nabla_{2D} > 0$, regions of local compression (velocity sinks) are characterized by $\nabla_{2D} < 0$. Symbols refer to simulation results (circles: $St = 0.1$, triangles: $St = 0.8$), whereas the solid line refers to the PDF computed for tracer particles uniformly distributed over the entire interface of each drop. The PDF was computed starting at time $t^+ \simeq 1000$ after particle injection and over a subsequent time interval $\Delta t^+ = 2000$. We see the PDFs of inertial particles are shifted toward the positive surface divergence semi-plane indicating that the captured particles tend to sample the regions of the source of velocity generated by jet-like fluid motion.

Cartesian components $\mathcal{A}_{i,j} = \partial u_j / \partial x_i$ [19, 9].

$$P = -tr[\mathcal{A}] \quad , \tag{3.5}$$

$$Q = \frac{1}{2}(P^2 - tr[\mathcal{A}^2]) \quad , \tag{3.6}$$

$$R = -det[\mathcal{A}] \quad . \tag{3.7}$$

For the present incompressible flow, $P = 0$ and the second invariant can be expressed simply as $Q = -\frac{1}{2}(S : S + \Omega : \Omega) = -\frac{1}{2}(S^2 + \Omega^2)$, where $S = \frac{1}{2}(u_{i,j} + u_{j,i})$ and $\Omega = \frac{1}{2}(u_{i,j} - u_{j,i})$ and the symmetric and asymmetric components of $\mathcal{A}$, respectively. In this case, Q represents the local balance between vorticity (related to Ω) and strain rate (related to S). The flow topology parameter can now be introduced[29, 111, 28, 127]

$$\mathcal{Q} = \frac{S^2 - \Omega^2}{S^2 + \Omega^2} \quad . \tag{3.8}$$

Based on this definition, $\mathcal{Q} = 1$ corresponds to purely elongational flow ($\Omega = 0$), $\mathcal{Q} = 0$ corresponds to shear flow and $\mathcal{Q} = -1$ corresponds to purely rotational flow ($S = 0$) [127]. The topology parameter has been used recently to examine the effect of a compliant interface on the flow field in different regions of the flow domain in two-phase systems [29, 111, 127]. We remark here that the turbulent flow field has lower intensity inside the droplets due to the elastic behavior of the interface, which damps convective effects and limits momentum transport from one fluid phase to the other [115]. This corresponds to smaller, nearly-zero values of S and Ω that lead to frequent changes in the sign of the numerator of Eq. (3.8). In turn, these changes are amplified by the denominator, which is always definite positive and produces values of $\mathcal{Q}$ between -1 and +1 regardless of the specific value of S and Ω, namely regardless of the turbulence intensity associated to these two tensors. To overcome this intrinsic limit of the above definition, we employed spline interpolation over neighbouring grid points to smoothen the spatial distribution of $\mathcal{Q}$.

Fig. 3.7 shows the instantaneous spatial distribution of $\mathcal{Q}$ in the wall-parallel $x^+ - y^+$ plane at the center of the channel. The interface of the drops is represented by the black solid lines. Panel (a) refers to the entire $x^+ - y^+$ plane, whereas the two insets show, for $St = 0.1$ and $St = 0.8$ respectively, a close-up view of particle distribution along the surface of the drop pair highlighted in panel (a). The presence of the interface has a clear influence on the local flow behavior.

The carrier phase appears to be characterized by large areas of shear flow (in green, corresponding to values of $\mathcal{Q}$ close to zero), and smaller fragmented regions of rotational flow (in blue, corresponding to values of $\mathcal{Q}$ close to -1) and elongational flow (in red, corresponding to values of $\mathcal{Q}$ close to +1). The flow inside the drops, on the other hand, is most often characterized by the predominance of both shear and elongational flow regions, as also noted by [127]. The insets show that small changes of particle inertia are sufficient to modify the spatial distribution of the captured particles over the interface. Note that, for the Weber number values considered in this study, only a small number of drops is found at steady state: Therefore, the drop size is large enough to minimize the internal flow confinement effects that are observed at higher Weber numbers [127].

It is not so easy to conclude something about the flow behavior very close to the interface just by visual inspection of Fig. 3.7. To this aim, in Fig. 3.8 we show the PDF of $\mathcal{Q}$ seen by the particles at the time they touch the interface and get captured. As done for Fig. 3.6, $\mathcal{Q}$ is evaluated when the phase field value interpolated at particle position is $\phi = -0.71$, namely at the edge of the capillary force range: This excludes any effect of this force on the motion of the particles in their final stretch to the interface. Lines and symbols are as in Fig. 3.6. For the case of inertialess tracers, the PDF is slightly asymmetric and negatively skewed, indicating that elongational flow events ($\mathcal{Q} > 0$) are slightly more likely than rotational flow events ($\mathcal{Q} < 0$). Interestingly, a small deviation from the $St = 0$ limit is sufficient to produce a significant quantitative change in the shape of the PDF: This change is generated by fact that particles can only reach the interface by following strong, coherent flow events directed towards the droplet; not because they can deviate from the fluid streamlines and touch the surface via a free-flight type of mechanism.

Entrainment into these jet-like flow events, in turn, leads to a non-uniform spatial

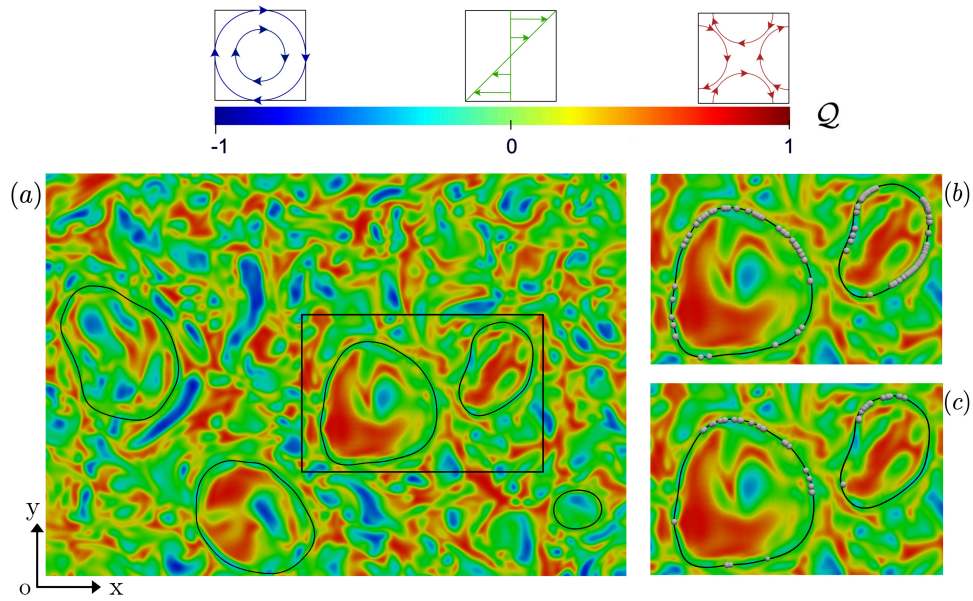

FIGURE 3.7 – (a): Flow topology parameter, $\mathcal{Q}$, on the channel midplane ($x^+ - y^+$ plane); black solid lines identify the position of the drop interface (iso-level $\phi = 0$). (b)-(c): Close-up view of the distribution of captured particles on the interface of the drop pair boxed in panel (a). Insets: (b) $St = 0.1$, (c) $St = 0.8$. The flow is dominated mostly by the shear events (the green regions corresponding to $\mathcal{Q}$ close to zero), but elongational and rotational (in red and blue, respectively, corresponding to values of $\mathcal{Q}$ close to -1 and to +1) dominated flow regions are also seen. Near interface regions are mostly dominated by shear and elongational flow region which is the the clear consequence of the presence of interface on the flow topology. We can appreciate the distribution of captured particles on the surface for two different inertial sets of particle; a very small change on the inertia (from $St = 0.1$ to 0.8) suffices to change the particle distribution.

distribution of capture events on the interface, and to a preferential sampling of the topological structures of the interface. Asymmetry is increased and the likelihood of particles sampling shear-dominated flow events decreases in favour of elongation-dominated events. As particles reach the very-near interface region, the interplay between the impinging fluid motions that are transporting the particles and the blockage effect of the interface generates stronger tangential stresses, which in turn generate localized elongational flows similar to that highlighted in inset *I* of Fig. 3.4. Strong rotational flow events also become slightly more likely, but this seems to be a minor effect.

To conclude the analysis of the flow events that drive particle capture, we examine their topological features by discussing the joint PDF of the second and third invariants of the velocity gradient tensor, Q and R. These invariants are computed at the Eulerian grid points and then interpolated at the instantaneous position of particle capture using fourth-order Lagrange polynomials: Near the interface, a one-sided version of the scheme is used to avoid mixing drop- and carrier-fluid velocities [39]. The time window considered to compute the invariants covers the last 400 viscous units of

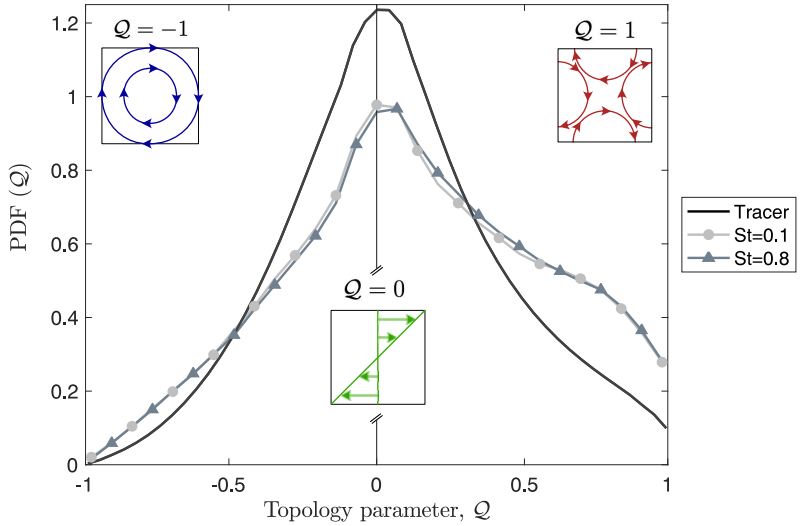

FIGURE 3.8 – PDF of the topology parameter, $\mathcal{Q}$, seen by the particles when they get captured by the interface. Lines and symbols are as in Fig. 3.6. The PDF was computed starting at time $t^+ \simeq 1000$ after particle injection and over a subsequent time interval $\Delta t^+ = 2000$. For the inertial particles, the peaks are decreased at zero compared to tracer but the right tail of the PDF is higher than before indicating that the pure shear regions are still the most probable but there is an increase of finding the captured particle at the pure elongational dominated regions generated by the flow impinging on the surface. This indicates that these are the coherent jet-like fluid structures that bring the particle to the interface.

the simulations. The conditioned joint PDFs so obtained are shown in Fig. 3.9.
For clarity of presentation, in panel (a) of this figure we show first a compact classification of all incompressible flow topologies in the (Q,R)-plane [98, 9]. This classification also involves the discriminant (D) of the velocity gradient tensor, defined as follows

$$D = \frac{27}{4}R^2 + Q^3 \quad . \tag{3.9}$$

If $D > 0$ then the tensor has one real and two complex-conjugate eigenvalues indicating prevalence of enstrophy in the flow, if $D < 0$ then the tensor has three real, distinct eigenvalues indicating prevalence of dissipation in the flow, if $D = 0$ then the tensor has three real eigenvalues, two of which are equal [39].
Based on the sign of D and R, four topological regions can be identified: When $D > 0$ and $R > 0$ (region I), the flow is characterized by predominance of vortex compression over vortex stretching and the opposite is true when $D > 0$ and $R < 0$
(region II); when $D < 0$ and $R < 0$ (region III), the flow is connected to diverging fluid trajectories while being connected to converging trajectories when $D < 0$ and $R > 0$ (region IV).
Fig. 3.9(b) shows the joint PDF conditioned at the position of uniformly-distributed tracers. This PDF is characterized by the same teardrop shape that is typically ob-

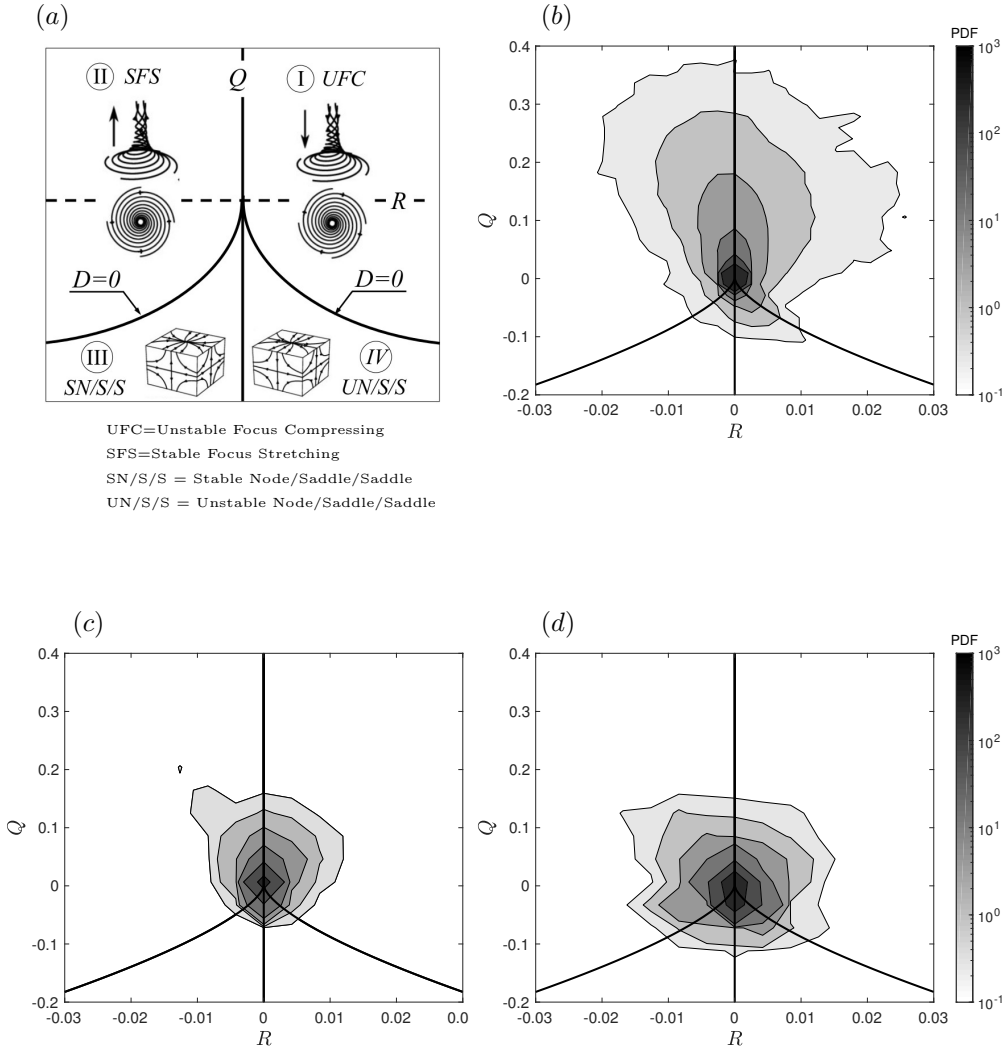

FIGURE 3.9 – Panel (a): Incompressible flow critical point topologies according to the classification scheme by [19]: Topologies falling in region I are called stable focus/compressing while those falling in region II are called unstable focus/stretching; topologies falling in region III are called stable node/saddle/saddle while those falling in region IV are called unstable node/saddle/saddle. Further critical points can be identified along the Q-axis and the $D = 0$ line, but their characterization is beyond the scope of this study. Panels (b)-(d): Joint PDF of Q, R conditionally sampled for fluid at grid points over the entire interface of the drops (b), at the position of the $St = 0.1$ particle when they get captured (c), and the position of the $St = 0.8$ particles when they get captured.

served in wall-bounded flows, and particularly in the viscous sublayer region. There is also evidence of events clustered around $Q = 0$ and $R = 0$, which are indicative of boundary-layer-like flow topologies [39]. This confirms that, at least from a qualitative viewpoint, there are similarities between the flow field near a compliant interface and the flow field near a solid wall. The most probable flow topologies are those falling in regions I and II, as also shown in Table I: These topologies represent vortical motions that contribute to the production of enstrophy via vortex compression or stretching, respectively.
When we consider the joint PDF conditioned at the particle position, there is a clear change of shape. Comparing also the percent values reported in Table I, we observe a non-trivial effect of the Stokes number. For the $St = 0.1$ particles, we find an increased probability associated to unstable focus/compressing topologies and a nearly equivalent decrease of the probability associated to stable focus/stretching topologies with respect to tracers (the sum of the two probabilities being equal to 77%). This indicates that $St = 0.1$ particles sample preferentially fluid motions that contribute to enstrophy production via vortex compression more often than via vortex stretching. Fluid motions characterized by high strain and high dissipation are avoided by these particles. For the $St = 0.8$ particles, probabilities are more evenly distributed with a significant increase for the case of node/saddle/saddle topologies, particularly unstable ones. These are regions with large negative values of Q and represent sites of high dissipation that $St = 0.8$ particles apparently sample just before adhesion.
Overall, Figs. 3.8 and 3.9 indicate that particle capture occurs mostly in regions of local interface stretching produced by turbulent fluctuations normal to the interface within the carrier fluid. These regions correlate well with high-enstrophy flow topologies and are produced by a competition between shear-dominated and elongation-dominated events.

3.2.4 Particle capture rate

The phenomenology of particle capture by the drop is as follows: A flow event, roughly described as a jet, transports the particles towards the interface; near the interface, the jet deflects and particles that are close enough are captured by the interfacial forces. This phenomenology is by no means different than that controlling particle

Quadrant	I	II	III	IV
Topology	Unstable focus/ compressing	Stable focus/ stretching	Stable node/ saddle/saddle	Unstable node/ saddle/saddle
Tracers	35%	45%	7%	13%
$St = 0.1$	42.5%	34.5%	9%	14%
$St = 0.8$	25%	33%	15%	27%

TABLE 3.1 – Probabilities representing the tendency of captured particles to sample the different incompressible topologies near the interface of the drops. Probabilities are averaged over the last 400 viscous time units of the simulations.

deposition at a solid wall [42, 20, 23, 120, 122]. Starting from this similarity, in this section we propose a simple mechanistic model that can be used to obtain a reliable prediction of the capture rate and, at the same time, can easily be implemented in industrially-oriented CFD codes. The model is an adaptation of classical deposition models [42, 23, 120] in which a diffusion-type equation is used to predict particle deposition to a wall by turbulence.
In general, there are three main deposition mechanisms that may act simultaneously: diffusion, impaction and interception. However, at fluid velocities typical of scrubbing devices and for micron-sized particles like those considered in the present study, impaction is known to be the dominant capturing mechanism [63]. In this case, the particle deposition rate is assumed to be proportional to the ratio between the mass flux of particles at the deposition surface, J, and the mean bulk concentration of particles, C. Through the definition of a suitable constant of proportionality, usually referred to as the deposition coefficient k_d, the following turbulent transport equation holds

$$J = k_d C \quad . \tag{3.10}$$

Given the initial number N_0 of particles released in the carrier fluid sub-domain, J and C can be discretized as follows

$$J = \frac{1}{A} \cdot \frac{dN_c(t)}{dt} \quad , \tag{3.11}$$

$$C = \frac{N_0 - N_c(t)}{V} \quad , \tag{3.12}$$

where $N_c(t)$ is the number of particles captured by the interface at time t, A is the total surface area of the drops and V is the volume occupied by the carrier fluid. These definitions yield

$$\frac{dN_c(t)}{dt} = k_d[N_0 - N_c(t)]\frac{A}{V} \quad . \tag{3.13}$$

Once k_d is known, Eq. (3.13) can be integrated to yield $N_c(t)$. In particular, for constant A and V

$$\frac{N_c(t)}{N_0} = 1 - \exp\left(-k_d \frac{A}{V} t\right) \quad . \tag{3.14}$$

where we estimated k_d to scale with the turbulent kinetic energy of the carrier fluid, $\mathcal{K}_T$, based on the observation that capture is driven by the turbulent fluctuations that transport the particles close to the interface. Ideally, it should be $k_d = C \cdot \mathcal{K}_T^{1/2}$ with $C \simeq 1$: Through this scaling, the value of k_d can be easily estimated even when RANS-based commercial flow solvers are used.
In Fig. 3.10, we show the time evolution of N_c obtained from the simulations for the $St = 0.1$ and the $St = 0.8$ particles, and we compare numerical results with those yield by Eq. (3.14). The comparison is proposed for a dimensionless value of the deposition

coefficient that satisfies the $k_d \simeq \mathcal{K}_T^{1/2}$ scaling and for a dimensionless value of $\mathcal{K}_T$ computed within a fluid layer of thickness equal to 2 wall units around the drop (rather than over the entire volume occupied by the carrier fluid). This choice is motivated by the observation that if we take $\mathcal{K}_T$ over the entire domain, we wont reproduce quantitatively the result, whereas, there is a well agreement between the model and results if we compute $\mathcal{K}_T$ in a small layer in near drop region. The physical explanation behind this choice is that this specific thickness is equal to the volume-averaged value of the Kolmogorov length scale and corresponds to a conservative approximation of the stopping distance of the $St = 0.8$ particles set (the particle stopping distance is the length scale on which we base the choice of the volume-averaging thickness) [42, 123]. In this case, we obtain $\mathcal{K}_T^{1/2} \simeq 0.17$ which is physics-based best fit of DNS data; in the sense that the value is not only a best fit on the data, but there is also a physical explanation behind this choice. The mean dimensionless value of A/V, also needed in Eq. (3.14), is equal to $1.3 \cdot 10^{-3}$ at steady state. We readily observe that the increase of N_c is unaffected by particle inertia, as one would expect at such low values of the Stokes number, and follows well the behaviour predicted by the model. We remark here that, for the Reynolds number considered in this study, the turbulent kinetic energy averaged over the entire volume occupied by the fluid is $\langle \mathcal{K}_T \rangle \simeq 1.8$, which yields $\langle \mathcal{K}_T \rangle^{1/2} \simeq 1.34$ instead of 0.17.
This difference can be ascribed to the deformability of the interface, which acts to damp turbulent fluctuations in the final fluid layer travelled by the particles before being captured by the interfacial forces. Clearly, using $\langle \mathcal{K}_T \rangle$ instead of $\mathcal{K}_T$ in Eq. (3.14) would significantly worsen the quantitative agreement with numerical results.

3.3 Conclusions

In this chapter, we examine the process of particle capture by large deformable drops in turbulent channel flow, and provide for the first time a detailed topological characterization of the flow events that control particle adhesion to the drop interface. To simulate the solid-liquid-liquid three-phase flow, we use a state-of-the-art Eulerian-Lagrangian method based on DNS of turbulence coupled with a Phase Field Model to capture the interface dynamics and Lagrangian tracking of neutrally-buoyant, sub-Kolmogorov particles. Drops have same density and viscosity of the carrier liquid, and the two fluid phases are one-way coupled with the particles.
Results discussed in this chapter refer to a shear Reynolds number $Re_\tau = 150$ and values of the Stokes number ranging from $St = 0.1$ to $St = 0.8$. To account for possible modifications due to a change of drop deformability, two values of the Weber number were considered, $We = 0.75$ and 1.5, but no effect of this parameter was observed. Therefore, only results relative to $We = 0.75$ have been discussed. An extensive analysis of the topological features of the flow events that drive particle transport toward the surface of the drops and lead to particle capture has been conducted. By using topology indicators, we were able to show that particle reach (and adhere to) the interface in regions of positive surface velocity divergence, which are generated by turbulent fluid motions directed towards the interface. These regions of local flow expansion appear to be well correlated with high-enstrophy flow topologies whereas fluid motions characterized by high strain and high dissipation are generally avoided by the

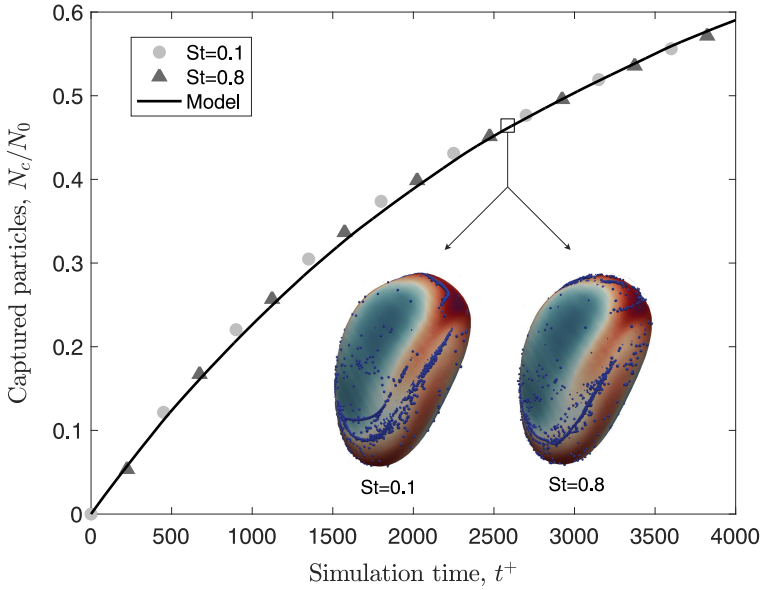

FIGURE 3.10 – Time evolution of the number of particles captured by the interface. Symbols refer to simulation results (circles: $St = 0.1$, triangles: $St = 0.8$), whereas the solid line refers to the model provided by Eq. (3.14). The inset shows the instantaneous distribution of the captured particles over the interface of a drop, shown in isolation from the flow domain and colored using the local interface curvature (red: high positive curvature, blue: low negative curvature): Particles appear to sample the same interfacial regions, confirming the secondary role played by inertia. There is the perfect agreement between the model and the simulation results when the black curve is obtained considering the constant $\gamma = 1$, and computing the turbulent kinetic energy of the carrier fluid, $\mathcal{K}_T$ in a small volume around the droplet surface rather than in entire volume of the domain. Perfect matching confirms that what controls the process of particle capture is indeed the near-droplet turbulent fluctuations.

particles. An important role is played by the ability of the interface to deform upon interaction with the neighbouring fluid motions, thus giving rise to highly non-uniform curvature and shear stress distributions. In particular, strong tangential stresses are produced on the interface, where occurrence of localized elongational flows is favoured.

Based on the topological characterization of the flow seen by the particles during the capture process, a simple mechanistic model to quantify the fraction of captured particles in time is proposed. This model may be regarded as a first attempt to lay useful guidelines for the development of physics-aware predictions of transfer rates in particulate abatement applications, particularly scrubbing. The proposed model is valid in the limit of non-interacting particles and exploits the proportionality between the mass flux of particles that adhere to the interface and the mean concentration of particles that remain afloat in the bulk of the carrier phase: It is therefore based on a single lumped parameter, the constant of proportionality between flux and concentration.

In spite of its simplicity, the model is capable of reproducing the time increase of the

fraction of captured particles with remarkable accuracy when the deposition coefficient is scaled with the square root of the volume-averaged turbulent kinetic energy of the fluid measured within one Kolmogorov length scale from the drop (chosen here because it represents a macroscopic property of the flow that can be directly obtained from single-phase simulations as long as dilute flow conditions apply). This finding can be explained by the fact that, in the present flow configuration, particle capture is driven by the turbulent fluctuations in the vicinity of the drop interface. For a mechanistic model to work it is therefore necessary to incorporate the effect of these near-interface fluctuations on the overall capture coefficient.

In this chapter, we focused primarily on the process of particle capture. Once the particles get captured, their subsequent trapping behavior on the drop surface and analysis of the dynamics that characterize the interface-trapped particles as they are driven by both fluid and interfacial stresses, is an independent study which will be discussed in detail in Chap. 4. To this aim, it is crucial to consider a system in which particle-particle collisions are taken into account (excluded-volume effects) in the regions of particle clustering to reproduce more physically their distribution over the interface. Also, the numerical setup should be able to mimic the potential effect of trapped particles on interface deformability via local modification (reduction) of the surface tension. The behaviour of trapped particles might changes by the presence of Marangoni stresses on the interface generated by the surface tension reduction.

4

Interface topology and evolution of particle patterns on big drops in turbulence

Reproduced in part from:
A. Hajisharifi, C. Marchioli and A. Soldati, *Interface topology and evolution of particle patterns on big drops in turbulence. J. Fluid Mech., (under review), 2021*

In this chapter we will investigated the subsequent process of particle capture; particle trapping on the surface of large deformable drops in turbulence. This process may have important consequences on the surface properties. At the microscale, particles are expected to act in a way similar to soluble surfactant molecules, affecting surface tension in particular [144, 128, 8]. This has important consequences at the macroscale, influencing drop deformability and hence coalescence and breakup processes. While the effect of soluble surfactants on local modifications of the surface tension has been widely investigated [12, 127, 85, 76], the effect of particles has received comparatively little attention, in particular as far as particle loading and spatial distribution at the interface are concerned [51]. Most of the available studies focus on heterogeneous systems in which the flow conditions are dominated by viscous forces [112, 80, 27]. Examples include foam and emulsion stabilisation problems, where particles are adsorbed at an air-water interface and are found to increase its surface dilational elasticity [144] In many industrial and environmental applications, however, a key factor is represented by turbulence. The interaction between small solid particles and fluid interfaces under the action of an underlying turbulent flow is crucial, for instance, in scavenging by raindrops or in scrubbing processes, where the overall abatement efficiency depends on the ability of the drop to trap particles for very long times [142]. Up to now, a detailed physical understanding of particle-interface interactions under turbulent conditions is missing. A primary reason is the wide range of length scales involved, from the particle microscale to the drop mesoscale [105, 29]. This scale separation makes it hard to establish a clear link between particle attachment, surface tension and

drop deformability, either experimentally or numerically [128]. Our study represents a first step towards the establishment of such a link by proposing a novel combination of computational models to examine the complex dynamics produced by a moving, deformable interface covered by tiny particles in a turbulent system accounting for the multiscale nature of the process. The presence of a compliant interface is crucial as it modulates the overall energy and momentum transfer between the carrier fluid and the drops [127], but also controls the efficiency with which particles are removed from the fluid. In Chap. 3 and in [52] , We investigated the process of particle removal by deformable drops, showing that particles are transported towards the interface by jet-like turbulent motions and, once close enough, are captured by interfacial forces in regions of positive velocity divergence. In this chapter, we build on this knowledge to examine the physical mechanisms that govern particle dynamics during the trapping stage, when particles interact with the drop surface. In particular, we focus our attention on the preferential distribution of the particles and its correlation with the interface topology.

To this aim, we rely on original simulations in which Excluded-Volume Effects (referred to as EVE hereinafter) are accounted for by enforcing inter-particle collisions. Albeit computationally expensive, EVE allow us to explore the evolution of realistic patterns that stem from the interaction of sub-Kolmogorov, quasi-inertialess spherical particles with super-Kolmogorov drops. Knowledge of particle distribution and of the driving mechanisms is crucial to determine its effect on the surface tension modification.

We will first characterize the process of particle trapping at the drop interface, focusing in particular on the correlation between particle distribution and specific regions of the drop interface and on the particle trapping rate to characterize particle behavior during the trapping stage, when particles are driven by both fluid and interfacial stresses. Then, we will investigate the effect of EVE on this process and the particle trapping rate which measures the efficiency of the abatement process.

We are able to show that particle spatial distribution correlates with specific interface topologies, which we characterize via the divergence of the velocity field on the surface. At later times, however, particles are observed to move away from these regions under the action of the tangential stresses acting on the interface to the regions vanishing surface divergence. The particle clusters are correlated with the local interface curvature, in view of the potential modulation that trapped particles may produce on the surface tension and, hence, on the drop deformability. This finding is important since the presence of tiny particles at the interface is known to affect locally the surface tension, particularly in the presence of concentration gradients: present results suggest that particle-induced modifications of the surface tension should be stronger where the curvature of the interface is higher.

4.1 Modelling and importance of occupied volume effects

Occupied volume effects are modelled considering particle-particle collisions. The proactive collision algorithm proposed by Sundaram and Collins [136] is used. Please refer to Appendix A for more detail on collision algorithm. These effects allow us to

reproduce a spatial distribution of particles at the drop interface that is more physical and close to a real flow instance.
The importance of modelling such effects is related to the capability of the particles to modify locally the surface tension. These changes can be incorporated in the surface tension equation of state via a concentration-dependent term. Providing a physics-based concentration distribution and concentration gradients over the interface of the drop is thus crucial to reproduce surface tension changes with quantitative accuracy, and clearly requires particle-particle interactions to be taken into account, otherwise particles would produce unphysical high concentration peaks that would lead to over-estimated changes of surface tension in some regions of the interface while producing underestimated changes of surface tension in those interfacial regions depleted of particles. Note that, for the present problem, particle collisions in the bulk of the carrier fluid are negligible and therefore the computational cost of the collision algorithm is $\mathcal{O}(\mathcal{N}_t \log \mathcal{N}_t)$, with $\mathcal{N}_t$ the number of particles trapped on the drop surface. In addition, the collision frequency scales with the local volumetric concentration of the particles, here inversely proportional to the surface area covered by the particles times the particle diameter.
Fig. 4.1 shows the total number of collision, N_{col}, in each time step for the particles with $St = 0.1$. The presence of drop surface leads to particle capturing; The interfacial stresses drive the particles to the specific region of the interface where the particles concentrate and form the clusters. Such concentration is much higher than the concentration one would typically find in a drop-less flow at the same volume fraction. The Fig. 4.1 demonstrates that about half of the total number of particles collide ($N_{col} = 2.4 \times 10^5$) in each time step after $t^+ = 3000$.
The number of collision increases significantly in time and it has not reached to a steady-state yet after $3000\, t^+$. The reason is that there are too many particles left in the bulk of the fluid that are still being captured by the drop surface. Therefore, the particle number increases within the clusters in time. The clusters become dense and denser and consequently the collision number increases in time. We would have expected to see the steady-state plateau with time if we had continued the simulations. In our opinion, nothing would have changed for the trapping mechanism, from statistical point of view, for longer time simulation but the more samples in the statistics. As a result, the collision algorithm becomes increasingly expensive as the simulation time increases, amounting up to about 80% of the computational cost of one time step.

4.2 Simulation setup

The setup adopted for investigation of trapping mechanism is a close channel configuration (no slip conditions for the flow field at both walls); Periodicity is imposed on all variables in streamwise (x) and span wise (y) direction.
The channel, with dimensions $L_x \times L_y \times L_z = 4\pi h \times 2\pi h \times 2h$, is discretized with $N_x \times N_y \times N_z = 512 \times 256 \times 257$ grid points. The grid spacings ($\Delta x^+ = \Delta y^+ = 3.7$, $\Delta z^+_{wall} = 0.0113$ and $\Delta z^+_{center} = 1.84$ is enough to resolve well the turbulent multiphase flow system.

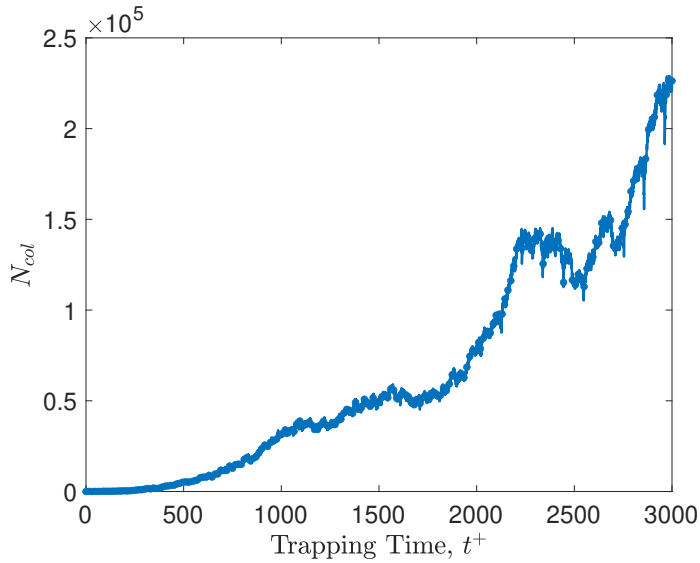

FIGURE 4.1 – Number of Collision, N_{col}, in time for $St = 0.1$; Increases significantly in time and it takes up to 80% of the computational cost of each time step. The number of particles captured by the surface of the drops increases in time, they concentrate and form the clusters. The more particles and the closer they are to each other, the greater the number of collision such that about half of the total particles collide at the end of simulation.

A constant pressure gradient is imposed along the streamwise direction to drive the flow at a constant shear Reynolds number $Re_\tau = 150$. The Cahn number, setting the thickness of the interfacial layer, has been set according grid resolution, $Ch = 0.02$. This value allows us to resolve accurately the interface with the current grid resolution; a minimum of 5 grid points is required to correctly capture the phase filed and its steep gradient across the interface [125, 127]. The Péclet number is set to $Pe_\phi = 1/Ch = 50$ according to the scaling proposed by [84] for the sharp interface limit. We considered two different values for Weber number is considered, $We = 0.75, 1.5$. These values are typical for oil-water mixture [139]. In Sect. 4.3, the simulation results are discussed with reference to lower Weber number $We = 0.75$ (less deformable drops). The effect of the Weber number observed in our simulations appears to produce minor quantitative modifications of the statistics.

At the beginning of the simulations, the phase field was initialized to generate

A regular array of 256 spherical drops with diameter $d = 0.2h$ (corresponding to $d^+ = 60$ in wall units) is initialized in a fully-developed turbulent flow; this flow is obtained from a preliminary DNS of single phase flow at $Re_{tau} = 150$. The phase field is initialized with its equilibrium profile; the phase filed is constant in the bulk of the phases ($\phi = +1$ in the droplet and $\phi = -1$ in the carrier phase) and goes under smooth transition across the interfacial layer.

At the first glance the phase field initial condition, injecting a swarm of spherical droplets to a turbulent flow field, may seems to be unrealistic. To ensure that the choice of initial condition does not effect the steady-state results, another initial condition

was tested; a liquid film has been injected to the channel center (the result is not reported here). The same statistically steady-state result (coalescence and breakage rates and number of droplet) has been seen; verifying that the initial condition memory will be lost after the initial transient.

Particles were released into the flow only after the surface area of the drops had reached a steady state, which results from a balance between coalescence and breakup events for the range of Weber numbers considered in this study (The very same condition discussed in Chap. 3). Two sets of $\mathcal{N}_p = 5 \times 10^5$ particles were tracked, with$St = 0.1$ and $St = 0.8$, corresponding to particle diameters much smaller than the drop diameter - $d_p/d \simeq \mathcal{O}(10^{-2})$ at least. Particles have zero initial velocity and are released randomly only outside of the droplets where the phase indicator, ϕ, interpolated at particle position equals to -1; $\phi_{@p} = -1$.

The simulation parameters are reported in Tab. 4.1.

Re_τ	150	150	150	150
We	0.75	0.75	1.5	1.5
St	0.1	0.8	0.1	0.8
EVE	YES—NO	YES—NO	YES—NO	YES—NO

TABLE 4.1 – Table 1: Summary of simulation parameters. Cases with and without Excluded-Volume Effects (EVE) are reported in the last row of the table. Results discussed in Sect. 4.3 refer to the simulations highlighted in light gray. The presented statistics refer to the case of $St = 0.1$ and $We = 0.75$ by considering and neglecting the particle-particle collision, EVE.

4.3 Results and discussion

The dynamic of the three-phase turbulent flow is first analyzed from a qualitative point of view, visualizing the distribution of the dispersed phases and how the EVE affect the distribution of non-interacting and interacting particles on the drop surface. The correlation between particle trapping and interface topology are then investigated to examine the cluster type via Correlation Dimension ,D_2, first and characterize the interface topology then by the mean of surface divergence to correlate the regions where these clusters are formed ,trapping regions, to the specific topological regions of the drop surface where the sink of velocity is observed; unlike the capture regions which are characterized by the source of velocity when the surface divergence is positive. These regions are found to be in the specific zone of the interface where the interface curvature is higher than mean. Using these statistics enables us to explain the particle behavior and its motion on the drop surface after they get captured. The analysis will then focus on the effect of EVE on particle trapping rate; the time evolution of the particle trapped at the interface will be investigated and trapping rate of interacting and non-interacting particle will be computed and compared to each other to highlight the fact that number of trapped particles increases in time at a rate that is almost independent of particle interaction and it is controlled mostly by the carrier fluid motion.

All the statistics presented in the following refer to a steady-state condition for the surface area of the drops. Unless otherwise stated, the statistics will be presented for the reference case of the $St = 0.1$ particles only: This choice is motivated by the marginal effect of particle inertia on the dynamics of trapped particles, which produces similar statistics (with just minor quantitative deviations) between the particle sets considered in this study. Note that a particle is classified as trapped if ϕ at its location is zero, ($\phi_{@p} = 0$).

4.3.1 Particle trapping and interface topology

In Fig. 4.2, we show the instantaneous spatial distribution of the trapped $St = 0.1$ particles at the final simulation time step ($t^+ = 3000$) when 50% of the particles have been trapped covering about 15% of the total surface of the drops. For visualization purposes, only a portion of the entire computational domain is rendered: Drops are visualized by the $\phi = 0$ iso-surface , the flow field is rendered by the fluid streaklines and particles are visualized as small black dots. Two different situations are compared: Particle distribution without Excluded Volume Effects (referred to as EVE), shown in panel (a), and particle distribution with EVE, shown in panel (b). In accordance with physical intuition, filamentary clusters characterized by high concentration of particles are observed to form when particles do not interact with each other and are allowed to overlap.

On the other hand, particle distribution over the drop surface becomes more even when occupied volume effects are accounted for, as can be well appreciated by looking at the two insets of the figure. Isolated particles are seldomly found. It is also apparent that, even at very long times after capture, particle clusters tend to form in the same ans particular portions of the interface. This observation implies that the dynamics of trapped particles is driven by flow phenomena that are unaffected by the mutual interactions (collisions) occurring in the accumulation regions of the interface, at least from a qualitative point of view. It also suggests that particle distribution correlates with specific topological features of the interface.

To elaborate on the above mentioned aspects and to investigate numerically the qualitative observation in Fig. 4.2, we examine in the following the changes in the morphology of the clusters that are produced in the case of interacting particles via Correlation dimension in Subsect. 4.3.2 and we try then to characterize the correlation between the particles and the interface topology.

4.3.2 Correlation Dimension

To examine the clusters that are formed upon particle accumulation in specific areas of the drop surface, we examine the correlation dimension [75, 49], which measures the fractal dimension of the clusters.

This observable was examined both experimentally [74, 75] and numerically [82, 87] to investigate the clustering of passive buoyant floaters or motile inertialess swimmers in free-surface turbulence, and can therefore be adapted to the present physical problem. In its most general (three-dimensional) formulation, the correlation dimension is computed by choosing one base particle and counting the fraction $n_p(r)$ of particles located

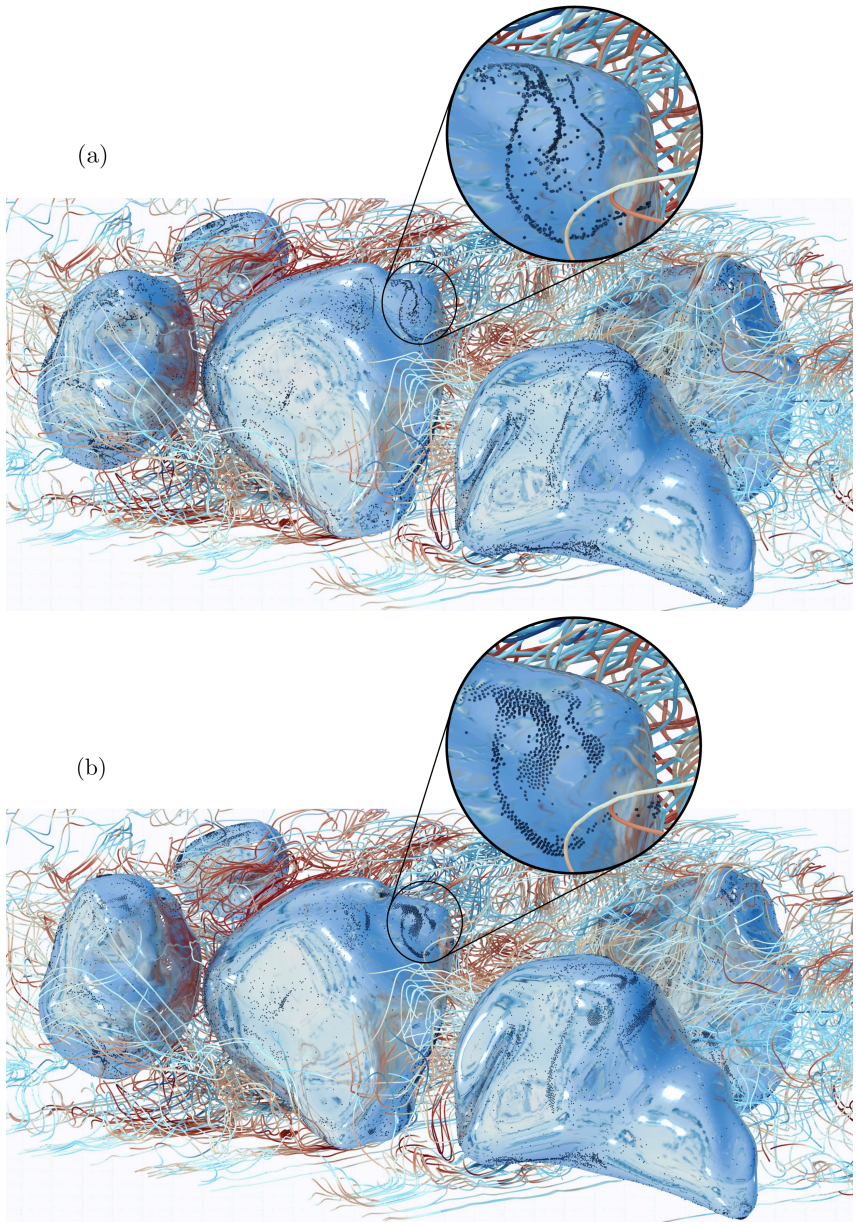

FIGURE 4.2 – Snapshot of qualitative rendering of particle distribution on the drop surface for the case of $St = 0.1$. The flow field is rendered by the mean of fluid streaklines and they are colored by their velocity, the droplet are visualized by the iso-surface of $\phi = 0$ and the particle are presented by the small black point. panel (a) refers to the distribution of non-interacting trapped particles on the drop surface. They do not see each other and they are allowed to overlap. Therefore, they form highly-concentrated filamentary clusters in the specific region of the interface, as highlighted in the insets. While when excluded-volume effects are accounted in the simulations, panel (b), the particles appear to distribute more evenly and sample the wider range of the drop surface.

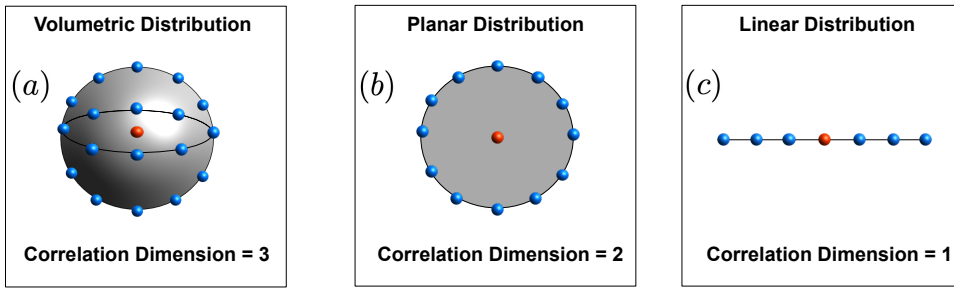

FIGURE 4.3 – Schematic of particle distribution and characterization of its clustering via Correlation Dimension (D_2). This parameter quantify how is the fractality over a cluster of particles inside a sphere centered on a sample particle. The red dot is the base particle and the blue ones are the cluster around the base particle. $D_2 = 3$ means the cluster is uniformly distributed in $3D$ space , i.e volumetric distribution panel (a), $D_2 = 1$ corresponds to the cluster uniformly distributed on $2D$ surface , i.e planar distribution panel (b) whereas, $D_2 = 1$ corresponds to a uniform distribution along a line, so to a filamentary particle cluster panel (c) .

within a sphere of radius r surrounding the base particle: The value of the correlation dimension is then equal to the slope of $n_p(r)$ as a function of r in a log-log plot. Since we are interested in the clusters that form on the drop surface, we computed $n_p(r)$ considering only the trapped particles: For this reason, we refer to the correlation dimension as D_2 hereinafter. In addition, we removed any length-scale dependence of D_2 by repeating the count of $n_p(r)$ for all possible values of r in order to obtain the probability distribution of the distance between the neighbouring particles and the base particle. Finally, we repeated the procedure for many randomly-chosen base particles, averaging the results to obtain converged statistics. By definition, $n_p(r)$ scales with r^{D_2} such that smaller values of D_2 indicate stronger preferential concentration and segregation.

In particular, if particles are uniformly distributed in the volume surrounding the base particle, then $n_p(r)$ scales with r^3, namely with the volume of the sphere centered on the base particle, and $D_2 = 3$, Fig. 4.3(a) ; In the case of particles that are uniformly distributed over a surface around the base particle, $n_p(r)$ scales with r^2, namely with the area of the circle centered on the base particle, so $D_2 = 2$, Fig. 4.3(b). In the case of particles that are distributed along a filament, namely along a line centered on the base particle, $n_p(r)$ scales with r and $D_2 = 1$ Fig. 4.3(c).

In Fig. 4.4, we show the time behaviour of the correlation dimension, $D_2(t)$, for the $St = 0.1$ particles, and we compare again the case in which excluded volume effects are accounted for (blue line with symbols) with the case in which these effects are neglected (red line with symbols). To visualize the effect of We and Stmodification on $D_2(t)$, we have also computed the the instantaneous standard deviation from $D_2(t)$, for the reference case when $We = 0.75$ and $St = 0.1$, as:

$$\zeta(t) = \sqrt{E[\mathcal{X}(t)^2] - (E[\mathcal{X}(t)])^2} \tag{4.1}$$

Where $\mathcal{X}(t)$ is defined as

$$\mathcal{X}(t) = D_2(We, St, t) - D_2(0.75, 0.1, t) \tag{4.2}$$

Where the $D_2(We, St, t)$ is the instantaneous correlation dimension computed for different simulations. In fact, we have computed D_2 for each of the simulations mentioned in Tab. 4.1 and the standard deviations respect to the reference case are computed and plotted as red shaded area for the non-interacting particles, while the blue shaded area is used to show the standard deviation for interaction particles, when EVE are accounted.

It can be seen that both curves start from $D_{2,0} = D_2(t = 0) \simeq 1.5$ where $t = 0$ indicates the time of the simulation at which the first capture event is recorded. The expected initial value of $D_{2,0}$ is a number between 1 and 2. $D_{2,0}$ can not be neither one nor two exactly because the particles can be captured anywhere on the drop surface and they don't follow any particular order in this stage. As a result, we don't expect to see any particular distribution, either linear ($D_{2,0} = 1$) or planar ($D_{2,0} = 2$), and the value $D_{2,0} \simeq 1.5$, seems to be a reasonable for correlation dimension at $t = 0$. Moreover, at this early stage of the capture process, not many particles are available for the computation of D_2 and, therefore, some variability is observed in the initial value of $D_{2,0}$ for the different cases simulated and the initial value may not be the very exact value.
As time progresses and clustering takes place, the value of D_2 can be computed over a larger ensemble of particles and is found to decreases significantly in the absence of excluded volume effects. Eventually, a value well below unity is reached. This trend indicates that particles tend to concentrate in filamentary clusters, like those observed in Fig. 4.2(a), but also that particles are non-uniformly distributed within a cluster. Non interacting particles do not see each other and they are allowed to overlap leading to value below unity.
When excluded volume effects are accounted for, the time evolution of D_2 changes dramatically and the correlation dimension increases up to saturation values just below the upper boundary, $D_{2,max} = 2$. This indicates that engulfment of interacting particles cannot continue indefinitely and that the clusters so generated tend to occupy a wider proportion of the drop interface, as highlighted in Fig. 4.2(b). Such more homogeneous sampling of the interface has a consequence on the correlation that can be established between the trapped particles and the interface topology.

4.3.3 Surface Divergence

The two-dimensional fluid velocity divergence at the interface of the drop, referred to as surface divergence, is used to describe the correlation between the regions of the trapped particle clusters and the topology of the interface.
The same definition for surface divergence,∇_{2D}, is used as described in Chap. 3

$$\nabla_{2D} = \mathbf{n} \cdot \nabla \times (\mathbf{n} \times \mathbf{u}) \quad . \tag{4.3}$$

According to this definition, particles moving on the drop interface probe a compressible 2-dimensional system in which regions of local flow expansion, generated by im-

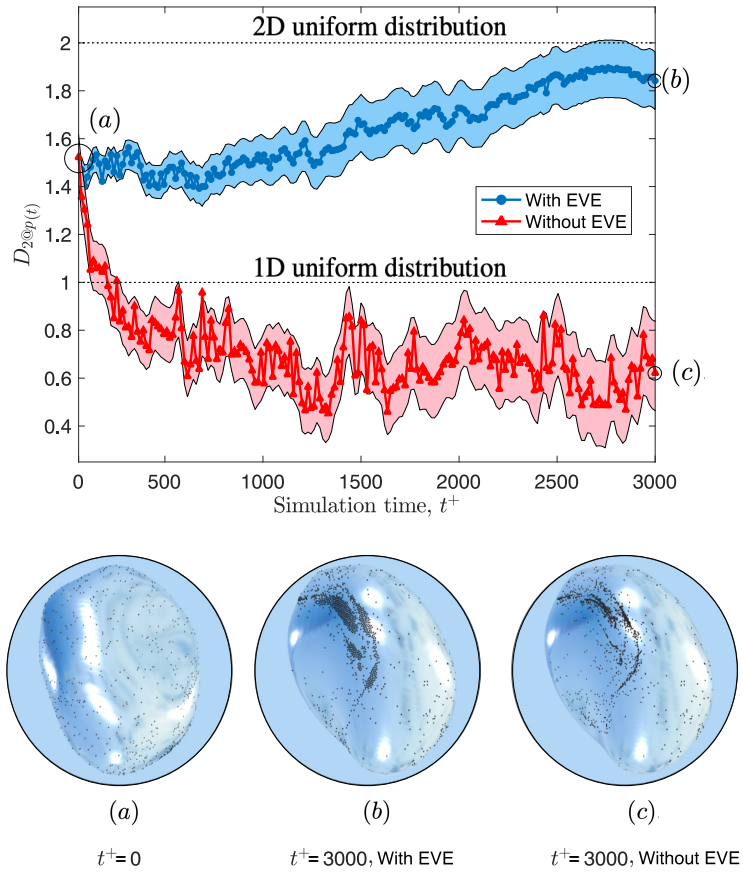

FIGURE 4.4 – Time evolution of the correlation dimension, $D_2(t)$, sampled at the instantaneous position of the trapped particles. The red curve with Symbols: $-\blacktriangle-$ refer to the case without considering EVE, while the blue curve with Symbols: $-\bullet-$ shows the case when EVE are accounted. The shaded area for both curves are the instantaneous standard deviation from $D_2(t)$ for the reference case with $We = 0.75$ and $St = 0.1$ to visualize the effect of We and St modification on the correlation dimension. The upper black dashed line demonstrate the value of $2D$ uniform particle distribution on drop surface , $D_2 = 2$; whereas the lower dashed line refers to the particle distribution along a line, filamentary distribution, when D_2 is one. Both curves start from $D_2(t = 0) \simeq 1.5$. At this stage, since there are not many particles available on the surface and the interface is just being loaded by the particles, there is no preferential particle concentration or accumulation, inset (a). The value of $D_2(t)$ decreases significantly in time for non-interacting particles due to the fact that they are allowed to overlap and form filamentary clusters as shown in inset (c), while the time evolution of correlation dimension changes significantly and increases close to 2, showing the quasi-uniform surface distribution. This indicates that the clusters occupy a wider portion of the interface , as highlighted in the inset (b).

pinging fluid motions, are characterized by $\nabla_{2D} > 0$ and regions of local compression, generated by outward fluid motions, are characterized by $\nabla_{2D} < 0$.
In Fig. 4.5, we show the time evolution of the surface divergence sampled at the instan-

taneous position occupied by the trapped particles on the drop surface, $\nabla_{2D@p}$. The two curves refer to the case with (blue) and without (blue) excluded-volume interactions, respectively. These curves are obtained by computing $\nabla_{2D@p}$ for each trapped particle over the entire time spent on the drop surface (which we call *trapping time* and start counting from the moment a given particle is captured by the drop surface), and then by ensemble-averaging the results over all available trapped particles. The shaded areas render the effect of We and St on $\nabla_{2D@p}(t)$, visualized again by means of the standard deviation, computed defining by

$$\mathcal{X}(t) = \nabla_{2D@p}(We, St, t) - \nabla_{2D@p}(0.75, 0.1, t) \tag{4.4}$$

Hajisharifi et al. [52] have shown that particles tend to get captured in regions of the fluid-drop interface where $\nabla_{2D} > 0$, being driven there by jet-like turbulent motions directed towards the interface. Because of the negligible inertia of the particles, the physical process leading to particle approach and adhesion to the drop surface is expected to depend marginally on particle-particle interaction. Indeed, this is what we observe in Fig. 4.5, where the initial value of $\nabla_{2D@p}$ is the same for the two cases compared. From a qualitative point of view, the evolution of $\nabla_{2D@p}$ is characterized by an initial transient in which the surface divergence decreases, followed by a steady state in which the $\nabla_{2D@p}$ oscillates around a mean value. This behavior indicates that trapped particles tend to move away from the capture regions, driven by both fluid and interfacial stresses. When particles do not interact with each other (red curve), however, the initial decrease is more accentuated and continues until $\nabla_{2D@p}$ attains a negative saturation value: This indicates that particles reach and accumulate in the flow compression regions of the drop surface, where filamentary clusters are found. This dynamics is prevented when EVE are accounted for (blue curve): The decrease is observed to occur over a shorter time transient and the steady state value of $\nabla_{2D@p}$ oscillates around zero, indicating that particles sample the drop surface topologies in a more homogeneous fashion. Clearly, not all trapped particles can accumulate in the $\nabla_{2D} < 0$ regions and (being unable to escape) are forced to occupy the neighbouring portions of the surface. This finding is relevant for the understanding of the potential effects that trapped particles may have on the interface deformability via local modification (reduction) of the surface tension: Excluded-volume interactions lead to lower peaks and smoother gradients of particle concentration, suggesting that surface tension modifications will be less abrupt than those predicted in the case of non-interacting particles, and distributed over a wider proportion of the drop surface. In Fig. 4.6, we show a qualitative rendering of the instantaneous particle distribution on the surface of the same drop at simulation time $t^+ = 1500$. The drops are visualized by the $\phi = 0$ iso-surface and they are colored by the local surface divergence; The positive surface divergence regions, $\nabla_{2D} > 0$, correspond to source of velocity are colored in red, The regions with the zero surface divergence ,$\nabla_{2D} = 0$ are in white and the regions of sink of velocity correspond to the negative value of the ∇_{2D} are colored in blue. Fig. 4.6(a) and (b) refer to the point (1) and (2) in Fig. 4.5, respectively. In this qualitative observation we can appreciate again the uniform and even particle distribution when particle-particle collision is considered, while they concentrate on a clusters when they do not see each other. What is new in Fig. 4.6 is the difference between particle distribution in white regions in panel a and dark blue regions in

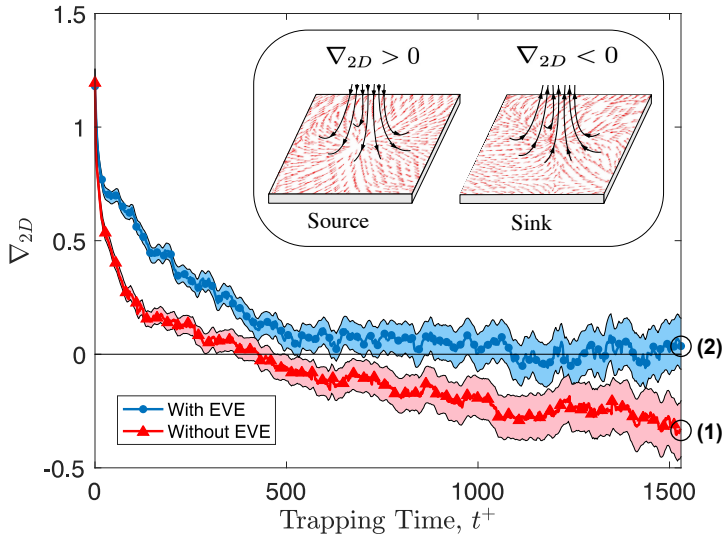

FIGURE 4.5 – Time evolution of the surface divergence, $\nabla_{2D@p}$, sampled at the position of the trapped particles. The red curve with Symbols: $-\blacktriangle-$ refer to the case of non-interacting particles, while the blue curve with Symbols: $-\bullet-$ demonstrate the case when EVE are accounted for the simulations. The shaded area for both curves correspond to the instantaneous standard deviation ζ, obtained considering all simulated cases to see the effect of We and St modification on the surface divergence. The point (1) and (2) are surface divergence at the position occupied by the particles, $\nabla_{2D@p}$, at the final time step of the simulation for the case of without and with EVE, respectively. These two point will be explain in more detail in Fig. 4.6. The inset shows the sink and the source of velocity on a portion of the interface, qualitatively. The direction of the fluid velocity vectors on the surface demonstrates how the fluid moves into/away from the sink/source regions. Both curve start almost from the same point, indicating that the particle-particle collision does not play an important role on particle adhesion to the surface, where the $\nabla_{2D@p}$ is positive. This is in agreement to what we have seen in Chap. 3 that the particle get captured in the sink regions. They decrease in time and reach to a steady-state value where they oscillate there. This behavior specifies that the particles tend to move away from the source regions and move toward to the region characterized by negative value of ∇_{2D}. The difference between two curves is that the decrease for the case without EVE is more accentuated showing that the filamentary clusters are found in the sink regions of the interface.

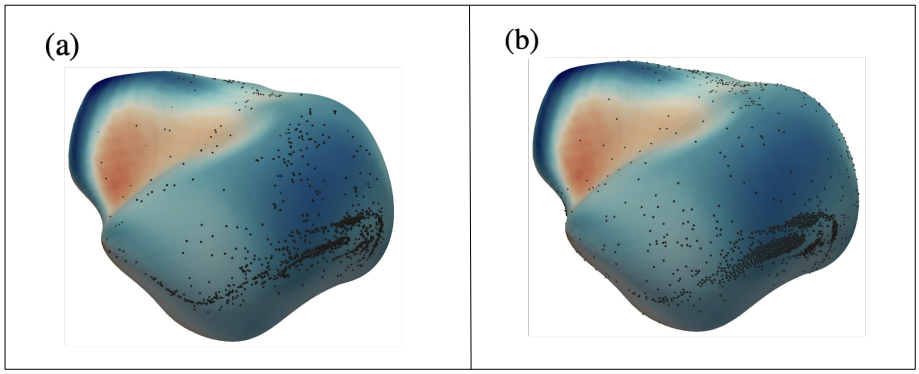

FIGURE 4.6 – Qualitative rendering of the particle distribution over the surface of the same drop at simulation time $t^+ = 1500$. The drop is visualized by the iso-surface of $\phi = 0$ and it is colored by the surface divergence, ∇_{2D}. The source regions with the positive surface divergence are colored in red, the white regions correspond to the zero surface divergence,$\nabla_{2D} = 0$, and the negative surface divergence, sink regions, are colored in blue. Panel (a) and (b) refer to points (1), non-interacting particles, and (2),interacting particles, in Fig. 4.5, respectively. The particle clustering is expected for the case of non EVE and the more uniform particle distribution when EVE are considered in accordance with the previous results. In panel (a) more particles observed in the dark blue regions, correspond to $\nabla_{2D} < 0$, compare to panel (b). In panel (b) there are more particles on the white regions, where $\nabla_{2D} = 0$. These observations confirm the negative and zero values for points (1) and (2) in Fig. 4.5, respectively.

panel b. It can be seen that the non-interacting particles tend to sample the negative surface divergence regions correspond to the sink of velocity whereas the interacting particles prefer to stay more in the white regions where the ∇_{2D} is zero. These observation confirm qualitatively what we have seen in Fig. 4.5 and highlight the differences between two cases compared.

To corroborate the observations made in the discussion of Fig. 4.5, in Fig. 4.7 we show the PDF of $\nabla_{2D@p}$ computed at the following trapping times: $t^+ = 0$ and $t^+ = 1500$. From Fig. 4.7(a), it is apparent that the two PDFs overlap almost perfectly, with a peak in the positive $\nabla_{2D@p}$ semi-plane. This indicates that the inclusion of excluded volume effects has no impact on the capture process and on the specific regions of the drop surface where capture preferentially occurs.

Hajisharifi et al. [52] have shown that these are regions of local flow expansion correlated with high-enstrophy flow topologies and that the resulting capture rate can be predicted using a model based on a single turbulent transport equation in which the only parameter scales with the turbulent kinetic energy of the fluid measured in the vicinity of the drop interface. Present results provide further evidence of the validity and applicability of this simple model. Fig. 4.7(b) shows that the PDFs depart from each other at large trapping times. In the absence of EVE (red line with symbols), the PDF shifts toward the negative $\nabla_{2D@p}$ semi-plane and exhibits a peak at values that are close to the steady-state saturation value observed for the red curve in Fig. 4.5. On the other hand, the PDF obtained when considering EVE is much less positively skewed and exhibits a peak at $\nabla_{2D@p} = 0$, which is the steady-state value observed for

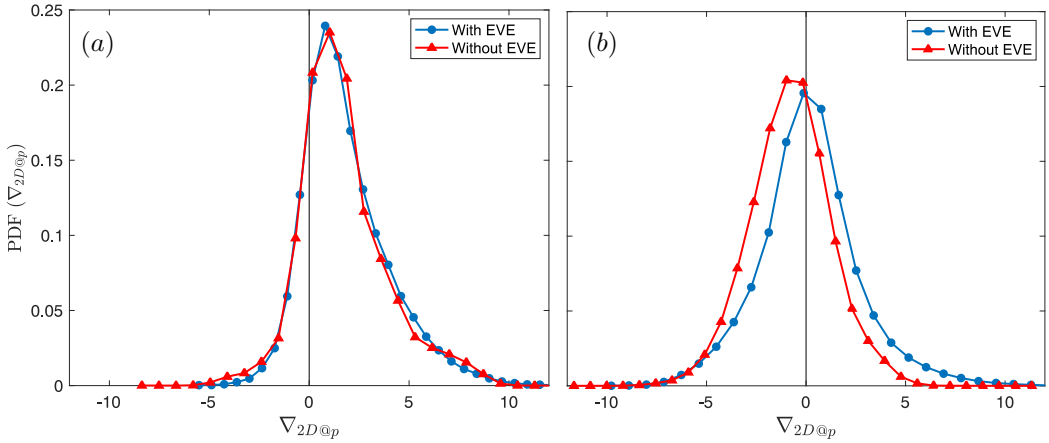

FIGURE 4.7 – Instantaneous PDF of the surface divergence, $\nabla_{2D@p}$, sampled at the position of the trapped particles (for the case $St = 0.1$). Panels: (a) PDF computed at trapping time $t^+ = 0$, corresponding to the the time instant at which one particle gets captured at the interface; (b) PDF computed at trapping time $t^+ = 1500$. At trapping time $t^+ = 0$, two PDFs overlap indicating EVE do not affect the capture process. while at trapping time $t^+ = 1500$, both PDFs shifted toward the negative region. The PDF has a peak around zero in the absence of EVE and the peak shifted toward the negative values when considering EVE. These observations are in agreement to the values observed in Fig. 4.5 for two cases.

the blue curve in Fig. 4.5: Particles are more likely to sample regions of positive surface divergence while the probability of sampling the strongest flow compression regions (characterized by the lowest negative values of $\nabla_{2D@p}$) remains unchanged. Note that the probability of sampling the strongest flow expansion regions (characterized by the largest positive values of $\nabla_{2D@p}$) is reduced after long trapping times, especially for non-interacting particles: This is an obvious consequence of the tendency of particles to be driven away from the capture region while subject to the action of tangential shear stresses [52].

4.3.4 Curvature

To complete the analysis of correlation between particle distribution, we first investigate the behavior of two trapped particle that are captured at the same time by the interface, computing their trajectory and visualizing their motion on the surface for an interval of $\Delta t^+ = 20$. Then, to characterize further the motion of trapped particle, the cos of the angle between normal to the interface and velocity vector is computed for the two time instants, $t^+ = 0$ and $t^+ = 1500$. Finally the PDF of curvature sampled at particle position has been computed for the same two time instant to finalize this analysis.

To do this, we need to determine the mean curvature of the interface which is the semi-sum of the two principal curvature κ_1 and κ_2. It is defined, in the framework of the phase field method, as the divergence of the normal vector to the interface, $\mathbf{n}$, and

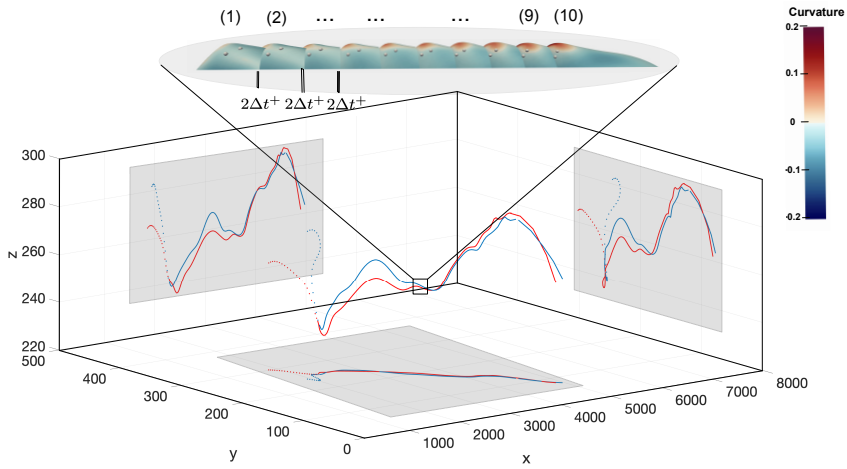

FIGURE 4.8 – Trajectory of two particles for $\Delta t^+ = 150$ in the presence of EVE. The axes show the traveling distance in wall unit scaling system in streamwise, spanwise and wall normal directions. The blue and red curves refer to the trajectory of each particles; The dotted lines refer to the particle trajectory before adhesion to the interface and the solid lines show their trajectory when they are on the surface. These two particles captured in the same time by the surface of drop but the adhesion occur in the different regions; The particles are far away at the initial stage of adhesion and they get close then to each other. Inset shows the time evolution of the interface and the particle distribution on the surface for an interval of $\Delta t^+ = 20$, qualitatively. The drop interface is colored by the local mean curvature and the particles are represented by the small white dots. The convex regions with the highest positive curvature are shown in red and the negative curvatures correspond to concave regions are in blue(saving frequency of each part is every $\Delta t^+ = 2$). Trapped particles getting close to each other while they are also moving toward the red region corresponding to highest positive curvature. The motion of these particles confirm the observation in PDF of Fig. 4.10(b).

can be computed as :

$$\mathbf{n} = -\frac{\nabla \phi}{|\nabla \phi|} \tag{4.5}$$

The minus sign is needed to obtain the outward-pointing normal ($\phi = +1$ in the droplet and $\phi = -1$ in the carrier fluid. The mean curvature defined as:

$$\kappa = \nabla \cdot \mathbf{n} = -\nabla \cdot \left(\frac{\nabla \phi}{|\nabla \phi|}\right) \tag{4.6}$$

Fig. 4.8 shows the $3D$ trajectory of two interacting particles for an interval of $\Delta t^+ = 150$. To make it more clear , the $3D$ trajectory is then mapped to $2D$ planes of $x - y$, $x - z$ and $y - z$. Time evolution of particles with the portion of the interface on which they move, is reported in the inset for a period of $\Delta t^+ = 20$ and is is depicted every $\Delta t^+ = 2$ (the time intervals are numbered from 1 to 10). For this statistics, 2 particles were selected that are captured at the same time by the drop surface and they

wont leave the interface. The blue and red curves refer to the trajectory of first and second particle, respectively. They are in the carrier phase and apart when we started computing the trajectories (the dotted lines refer to time when they are still inside the carrier fluid). They adhere to the interface at the same instant and start traveling on/with the surface in domain (the solid lines show the particle trajectory when they are on the surface). They move on the surface for a while and start getting close to each other. This was when we highlighted their behaviors in the inset. The interface is visualized by the $\phi = 0$ iso-surface and it is colored by the mean local curvature. The red region corresponds to the highest positive curvature, convex regions, while the concave region with the highest negative curvature is colored in blue. In the first time interval, the particles are apart and they are in the negative curvature region colored by blue. They start getting close to each other and move toward to white regions where the mean curvature is about zero (in 5th, 6th intervals); continue their motion to the convex regions with the positive surface curvature (red zone). These observations show that the particles do not have preferences where to adhere to the interface, but they tend to move toward the positive curvature regions. In these regions interfacial stresses are higher, suggesting that the particle motion is probably controlled by these stresses on the interface rather than the carrier phase when they are trapped.

To characterize more the particle motion on the surface, we analyze the alignment between the velocity vector $\mathbf{u}$ (evaluated at the interface) and the interface normal$\mathbf{n}$. In particular, we compute the cosine of the angle θ , where θ is the angle between the velocity vector (evaluated at the interface) and the interface normal; The results are reported in Fig. 4.9.

The interface normal $\mathbf{n}$ in the phase field approach is computed through 4.5. The scalar product between the interface normal and the velocity, normalized by its magnitude, to obtain the cosine of the angle θ

$$\cos\theta = \mathbf{n} \cdot \frac{\mathbf{u}}{|\mathbf{u}|} \tag{4.7}$$

The cosine of θ varies from $\cos\theta = -1$ (interface normal and velocity opposed) to $\cos\theta = 0$ (interface normal and velocity perpendicular) up to $\cos\theta = +1$ (interface normal and velocity concordant). To characterize the alignment between these two quantities at the interface of drop, we computed the PDF of $\cos\theta$ for two different time instants; The blue curve refers to the time when particles get captured and adhere to the interface, trapped time $t^+ = 0$ and the red curve to the trapped particle at trapping time $t^+ = 1500$ (at the same two instants of Fig. 4.7) and it is computed for the case of interacting particle.

We start by considering the case at trapping time $t^+ = 0$. We see that there is a peak very close to $\cos\theta = -1$, while the larger value of $\cos\theta$ (in magnitude) are very unlikely to be found. This indicates that there is a strong probability that the interface normal and the velocity vector are opposed. Conversely, there is a much lower probability that the interface normal and the velocity vector are perpendicular or aligned along the same direction. The larger probability of finding velocity opposed to the interface can be attributed to the direction of normal always pointing outward and the particle motion when the jet-like coherent fluid motion push the particle toward the interface and confirms the mechanism of particle capture process [52].

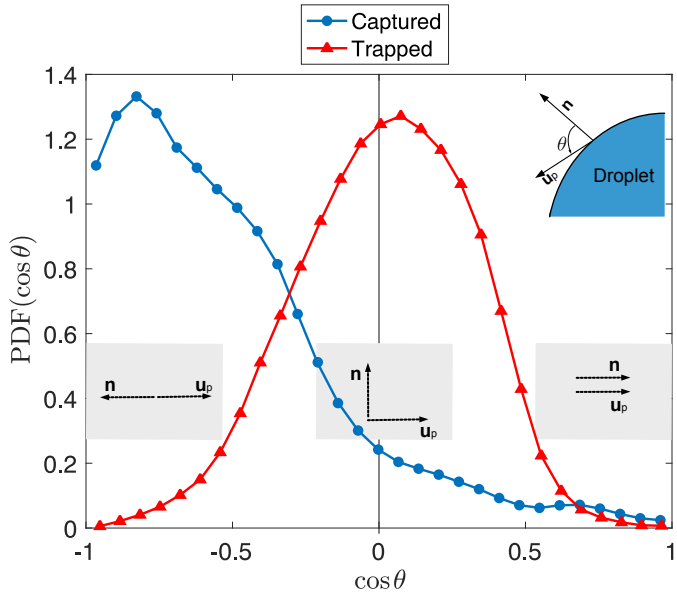

FIGURE 4.9 – Probability density function of $\cos\theta$ computed at the interface, with θ the angle between normalized velocity $\mathbf{u}/|\mathbf{u}|$ and interface normal n (see the inset). We can distinguish among three different reference configurations: $\cos\theta = -1$ (interface normal and vorticity opposed), $\cos\theta = 0$ (interface normal and vorticity perpendicular), and $\cos\theta = +1$ (interface normal and vorticity concordant). The blue curve refers to the PDF of $\cos\theta$ for the trapping time $t^+ = 0$, when the particles captured by the interface while the red curve shows the PDF of $\cos\theta$ for the trapped particles at trapping time $t^+ = 1500$. The blue PDF show that the velocity and normal are opposed when the particle adhere to the surface confirming that the fluid motion is perpendicular to the interface when pushes the particle . Once they trapped, they move tangentially on the surface to get away from the capture region via the tangential stresses. In this case the probability of finding normal and velocity vector perpendicular is much higher (red PDF).

We can appreciate a clear modification of the PDF shape taken at trapping time $t^+ = 1500$(red curve). This PDF is more symmetric and exhibit a peak around $\cos\theta = 0$ and the possibility of finding the positive and negative values of $\cos\theta$ is lower.

This indicates that it is more probable to find the interface normal and the velocity vector perpendicular while there is much lower probability that the normal and velocity vector are aligned in the same/opposite direction. This can be explained by the tangent motion of the particles on the surface to the higher curvature regions either negative or positive by the interfacial stresses. When the normal and velocity vector of trapped particles are perpendicular, they move mostly tangential on the surface. In a better word, they move in the same direction as the interfacial stresses; suggesting that these stresses move the particles away from the capture region to the zones characterized by the negative value of surface divergence.

In Fig. 4.10 we show the PDF of the fluid-drop interface curvature sampled at the position of the trapped particles, $\kappa_{@p}$. The PDFs shown in Fig. 4.10 refer to values

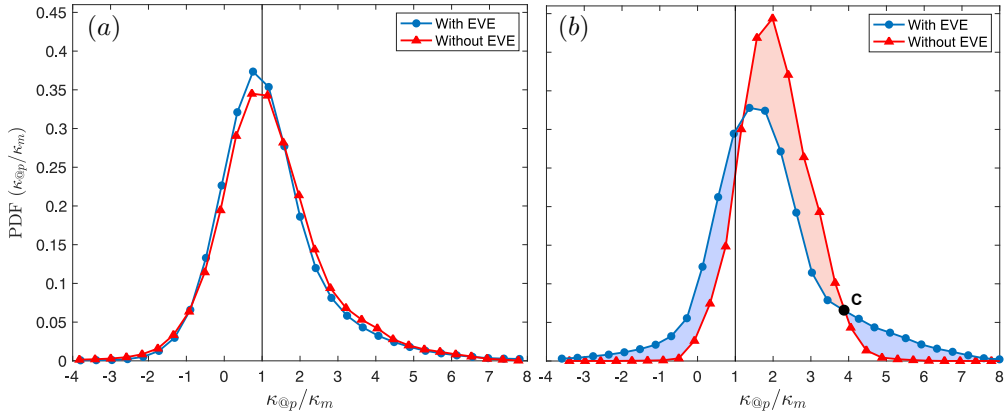

FIGURE 4.10 – Instantaneous PDF of the normalised interface curvature, $\kappa_{@p}/\kappa_m$, sampled at the position of the trapped particles (for the case $St = 0.1$). Panels: (a) PDF computed at trapping time $t^+ = 0$; (b) PDF computed at trapping time $t^+ = 1500$. Two PDFs in panel (a) overlap, confirming again the particle capture is independent of particle interaction and it is mostly controlled by the carrier phase. The peaks are around 1, indicating that there is no correlation between the regions where particle gets captured and the corresponding interface curvature. The PDFs in panel (b) are shifted toward the positive curvature semi-plane showing that the trapped particles tend to sample the regions of higher positive curvature.

of $\kappa_{@p}$ computed at the same two time instants of Fig. 4.7, and normalised by the instantaneous mean value of the curvature computed over the entire surface of the drops, κ_m. Note that the value of κ_m is not constant and tends to decrease in time due to the occurrence of breakup and coalescence events: For the specific Weber numbers considered here, the net outcome is a reduction of the number of drops in time until a steady state is reached. We also remark here that the ability of the interface to deform upon interaction with the neighbouring fluid motions gives rise to a highly non-uniform curvature distribution: Hence the need to examine a normalized statistical observable. Fig. 4.10(a), taken at trapping time $t^+ = 0$, shows that the PDFs with and without EVE are almost perfectly overlapping at the moment a particle gets captured by the drop surface, as could be expected from the discussion of Fig. 4.7(a). In addition, the PDFs exhibit a peak at values of $\kappa_{@p}/\kappa_m$ that are very close to unity, suggesting the absence of a correlation between the location of particle capture and the corresponding interface curvature.

Fig. 4.10(b), taken at trapping time $t^+ = 1500$, shows that both PDFs have shifted towards the positive $\kappa_{@p}/\kappa_m$ semi-plane, indicating that trapped particles sample preferentially high curvature regions of the drop surface. When excluded-volume effects are considered (blue curve with symbols), however, the shift is less evident and the PDF is less negatively skewed compared to the case of non interacting particles (red curve with symbols). Also, the PDF becomes flatter and broader, with a peak at lower values of $\kappa_{@p}/\kappa_m$ (from 2 to 1.5, roughly) and non-zero probability associated to the highest positive and lowest negative curvature values. These observations lead to the conclusion that interacting particles sample a wider range of interface curvatures,

which is in line with the more even particle distribution highlighted in the previous figures. This finding is relevant for the modelling of local surface tension modifications, hinted to when discussing Fig. 4.5. The engulfment of particles will affect mostly the portions of the drop surface where the curvature is higher than the instantaneous mean (namely the convex regions), especially above $\kappa_{@p}/\kappa_m \simeq 4$ where the cross-over point between the two PDFs, labelled as C in Fig. 4.10(b), is located. Additionally, particles will determine a change of deformability in regions of lower-than-mean curvature as well as negative curvature (corresponding to the concave regions), which appear to be unaffected by non-interacting particles.

4.3.5 Excluded volume effects on particle trapping rate

Physical intuition suggests that excluded-volume effects play a marginal role in determining the particle dynamics as long as the particles, which are quasi-inertialess, are confined within the carrier fluid. In addition, since particle adhesion to the drop surface is controlled by specific carrier fluid motions (discussed in Chap. 3), one might expect excluded-volume effects to be of secondary importance for determining the rate at which particles are captured by the surface. When trapped particles are not allowed to overlap, however, the overall coverage of the drop surface will be higher than that predicted in the case of non-interacting particles and the resulting particle engulfment might prevent the occurrence of some capture events (a particle reaching the drop surface at a location already occupied by another particle will either bounce back into the carrier fluid domain or detach the trapped particle). To quantify the actual excluded volume effects on the particle trapping rate, in Fig. 4.11 we show the time evolution of the number N_t of $St = 0.1$ trapped particles, normalised by the total number of tracked particles N_0, with and without EVE (blue and red curve with symbols, respectively). The inset shows the ratio of the area A_p covered by the particles when excluded-volume effects are considered in the simulations to the instantaneous total area of the drops, A_d: This ratio would be equal to unity if the drop surface was entirely covered by the particles. Note that the particles are injected into the flow when the time average of A_d has reached a statistically-steady value, but the instantaneous value of A_d (which we used to compute the ratio) changes.
It can be observed that the number of trapped particles increases in time at a rate that is independent of particle interactions up to $t^+ \simeq 1500$, when the interface area covered by the particles is nearly 10 % of the total drop surface. At later times, the number of trapped particles in the simulations without EVE increases at a slightly higher rate: By the end of the simulation, half of the particles released into the flow have been trapped. Hajisharifi et al. [52] have demonstrated that the time increase of N_t/N_0 can be predicted with very good accuracy with a model that, exploiting the similarity between the particle capture process and the process of particle deposition at a solid wall, is based on a single turbulent transport equation in which the only parameter scales with the turbulent kinetic energy of the fluid measured in the vicinity of the drop interface. If excluded-volume effects are turned on, however, the evolution of N_t/N_0 changes from a quantitative point of view and yields a lower final percentage of trapped particles (46% roughly). On the one hand, this result suggests that the model proposed by Hajisharifi et al. [52] may be less accurate in quantitatively predicting

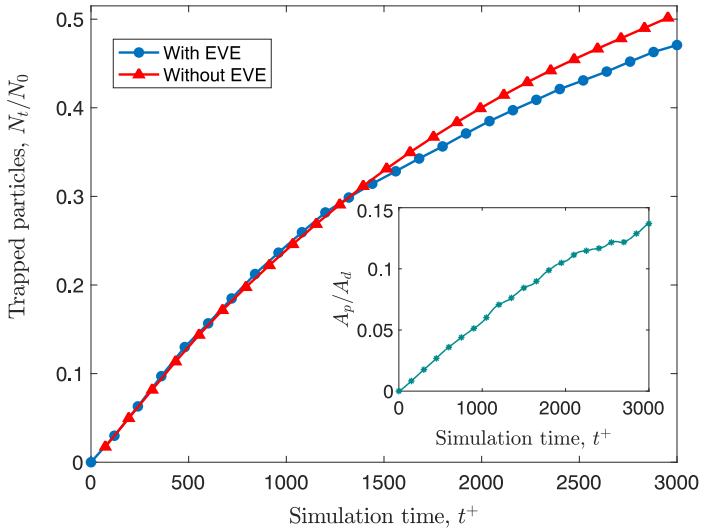

FIGURE 4.11 – Time-evolution of the number of $St = 0.1$ particles trapped at the interface. Symbols: –▲– without excluded-volume effects; –●– with excluded-volume effects. The inset shows the increase in time of the interface area covered by the trapped particles, A_p, normalised by the total interface area of the drops, A_d. The comparison between blue and red curves shows that the increase rate of the number of trapped particle is nearly independent of the particle-particle interaction effect. The slight difference occurs when the particles cover around 10% of the surface area.

the overall trapping efficiency. On the other hand, however, the deviations observed in Fig. 4.11 are limited to a few percents and, therefore, the error incurred when using such model may still be acceptable, considering that it would provide a (conservative) overestimation of the trapping efficiency and that the model is extremely simple to apply.

4.4 Conclusions

In this study, we examine the dynamics of neutrally-buoyant, sub-Kolmogorov particles trapped at the interface of large deformable drops in turbulent channel flow. To investigate this problem, we use an Eulerian-Lagrangian approach based on direct numerical simulation of the turbulent flow coupled with a Phase Field description of the interface dynamics and a Lagrangian tracking of individual particle trajectories. The approach also accounts for excluded-volume interactions between particles, modelled as inter-particle collisions. We focus on a solid-liquid-liquid flow configuration, with physical parameters corresponding to the case of water as carrier fluid, low-viscosity silicone oil drops and tiny colloidal particles. Drops have same density and viscosity of the carrier liquid, and all three phases are one-way coupled with each other. Results discussed in the paper refer to simulations with shear Reynolds number $Re_\tau = 150$, Stokes number $St = 0.1$ and Weber number $We = 0.75$. Additional simulations

carried out at different Stokes number (up to $St = 0.8$) and different Weber number (up to $We = 1.5$) show that the behavior of trapped particles is not affected by their inertia, which is always very small, and by the drop deformability, at least within the range of values examined. We provide for the first time a detailed characterization of particle behavior during the trapping stage, when particles are driven by both fluid and interfacial stresses. We observe a clear tendency of the particles to move from areas of the interface characterized by positive surface divergence (which are preferentially sampled at the time of capture and adhesion to the interface) to areas of vanishing surface divergence that are also characterized by high interface curvature.

5

Conclusions

The dynamics of particle capture and subsequent trapping by large deformable droplets in turbulent flow has been characterized throughout this thesis. This solid-liquid-liquid three-phase flow system is simulated using an Eulerian-Lagrangian method based on Direct Numerical Simulation of turbulence coupled with a Phase Field Model to capture the interface dynamics and Lagrangian approach to track each neutrally-buoyant, sub-Kolmogorov particles individually. To isolate the effect of turbulence on this study, drops and carrier liquid have the same density and viscosity and the two fluid phases are one-way coupled with the particles.

A numerical approach for the simulation of particle-laden interfaces has been presented, Chap. 2. In particular, a capillary force based on liquid-liquid tension is introduced to model particle-interface interaction for small spherical particles adsorbed at a fluid interface; This model has then been extensively tested.

The process of particle capture by surface of drops in turbulent flow has been investigated first, Chap. 3. The near drop regions is characterized via the statistical tools to provide the detailed topological feature of the flow events, specially those control particle adhesion to the interface. Topology indicators show that the regions of positive surface velocity divergence generated by the coherent jets are, where the particles adhere to the interface. The carrier phase appears to be characterized mainly by pure shear flow regions with some fragmented regions of rotational and elongational flow whereas the dispersed phase seems to be characterized by the strong presence of both shear and elongational flow regions due to the influence of the interface. The particles sample mostly the pure elongational dominated regions generated by the flow impinging on the surface. Therefor, these are the coherent jet structures that bring the particle to the interface.

A model is proposed to quantify the particle capture rate in time based on the flow characterization and the similarity to the process of particle deposition at solid wall in which a diffusion-type equation is used to predict the deposition by turbulence[42, 23, 120]. In this model, the mass flux of the captured particles is proportional to the mean particle concentration; the constant of this proportionality is a single parameter that should be determined somehow. We proposed to scale it with the turbulent kinetic energy due to the fact that the particles are driven toward the drop surface by the turbulent fluctuation. Indeed, it is scaled with the square root of the volume-averaged turbulent kinetic energy of the fluid measured within one Kolmogorov length scale from the drop rather than the entire volume of the domain. This indicates that the

particle capture is driven by the turbulent fluctuation in near-drop region; in other words local fluctuations.

Once the particles get captured, their subsequent behavior of trapped particles on the interface and analysis of the their dynamics has been investigated Chap. 4. The particles in this stage are driven by both fluid and interfacial stresses and tend to form clusters; it is crucial to consider particle-particle collisions in this study (excluded-volume effects) in the regions of particle clustering to reproduce more realistic particle behavior and their distribution over the interface is more physical. Within the range of values examined in this chapter, the particle inertia is very small and their behavior is not affected only by their inertia. We observe a clear tendency of the particles to move away from the regions of the source of velocity, where they get captured and adhere to the interface, under the action of the tangential stresses acting on the interface. Eventually, excluded-volume interactions bring particles into regions of vanishing surface divergence, where two-dimensional clusters are formed. Clustering into one-dimensional, highly-concentrated filaments is less likely to occur and this hampers particle accumulation into regions of negative surface divergence, which correlate with jet-like fluid motions directed away from the interface. Regions of long- term trapping and high particle concentration correlate well with portions of the interface characterized by higher-than-mean curvature.

Limitations and future developments

Spherical particles are only considered in this work; as long as point-particles are concerned it would be easy to extend this work to include also non spherical particles like small rods or disks. However, the shape of particles is not expected to play an important role in capture processes since particles have little inertia and the capture process is dominated by turbulence. Trapping mechanism may be influenced by shape modification as it has an effect on the drag. Particles are assumed to be neutrally-buoyant and have the same density as fluid ($\rho_p = \rho_f$, no effect of gravity), but it can be extended to the non-matched density.

The drops and carrier phase are considered to be matched density and viscosity. The same density could be a reasonable choice for liquid-liquid dispersion whereas the matched-viscosity appears to be relevant for situations in which the two fluids are water and low-viscosity silicone oil. The density and/or viscosity differences among the phases, which were neglected in our simulations, may induce local modifications of the flow topology in the near-interface regions. Viscosity variation produces different coalescence or breakage event dominated regimes which can modify the particle capture rate. When the drop viscosity is smaller than the carrier fluid, breakage is favored [109]; The final droplets number increases and consequently more surface areas are available for capture process leading to an increase of the number of captured particle in the same time window. By contrast, when the drop viscosity is larger, coalescence is favored. In this case we expect less particle captured by the drop surface due to the less available surface area.

The local interactions of particles with drop surfaces and particle trapping are not considered explicitly. In the sense that we were not able to model explicitly the interface deformation, due to the presence of the particles, or contact angle which is

assumed to be a fixed value of 90 degree for all simulations, but they are considered implicitly in the value of parameter $\mathcal{A}$ in the capillary force equation Eq. (2.42).
The modification of surface tension is not considered in this study. In order to do this, the model should include the modified equation of state for the surface tension in which the dependency of the local surface tension value on the local particle concentration is considered in a way similar to what was done by Soligo et al. [125, 128]. The next step of this work is to include the potential effect of trapped particles on interface deformability via local modification (reduction) of the surface tension by adding a Laplace pressure to the drops [50]. This increases the drop deformability leading to increase of the probability of rapture or breakup events. The surface tension gradients so generated might produce additional Marangoni stresses on the interface, which might change further the behaviour of trapped particles.
The particle attachment model used in this study does not prevent detachment events and we have seen some particles detached from the surface due to the effect of turbulence. It is known that gently shaking a bubble coated with hydrophobic particles led to significant detachment rates [3]. The effect of turbulence is qualitatively similar to shaking the bubble. However, we can not validate the detachment rate against the experimental results because there is not experimental work, to the best of our knowledge, available in literature for this setup.
Finally, we have chosen Phase field Method to model the interface in our study because compared to the other methods, its main advantages are: (i) automatically handling and description of coalescence and/or breakage phenomena (ii) accurate description of the interface shape and curvature (iii) specific advection schemes are not necessary.

A

Inter-particle collision

In the following an overview of the method used to detect the colliding pairs and collision events will be briefly reviewed. The first step is creating the searching lattices according to the criteria discussed in Sect. 2.3.2; Nxc, Nyc and Nzc are the number of uniform grid points in x, y and z, respectively. So. the cell numbers are

$$Cellx = Nxc - 1\,, \quad Celly = Nyc - 1\,, \quad Cellz = Nzc - 1\,,$$

$$Nct = Cellx * Celly * Cellz$$

Where $Cellx$, $Celly$ and $Cellz$ are the number of cells in x, y and z, respectively and Nct is the total number of created cells.
The next step is to identify and number each cell according to the following formula

$$\begin{aligned} Icell(ix, iy, iz) = 1 &+ \mathrm{mod}(ix - 1 + cellx, cellx) \\ &+ \mathrm{mod}(iy - 1 + celly, celly) * cellx \\ &+ \mathrm{mod}(iz - 1 + cellz, cellz) * cellx * celly \end{aligned} \tag{A.1}$$

Where $Icell$ is the $3D$ number of each cell, ix, iy and iz are the index of the lattices, goes from 1 to the total cell numbers in each direction. The cells are numbered first in x then in y direction thus having the full plane and finally in the z direction. having the cell number, makes possible for each cell to knows its neighbors, thus restricts the search for possible collision within the same cell and the 26 neighboring cells of the one containing the particle Fig. A.1.
For each cell a list with the numbers of 26 neighboring cells is then created. Special attention is given to the lists for the first and the last cells on xy plane due to the periodicity in the x and y directions, so that the possibility of collision between two particles residing at the two opposite sides of the domain is preserved. Once the searching lattices are created and numbered, it is the necessary to link each of the cells to particles dispersed in it. Each particle is sorted in its cell according to its position in the domain and a list of particles associated to each cell is then created. To find the cell number containing the particle, the same formula previously used to compute the cell number, $Icell$, is used.

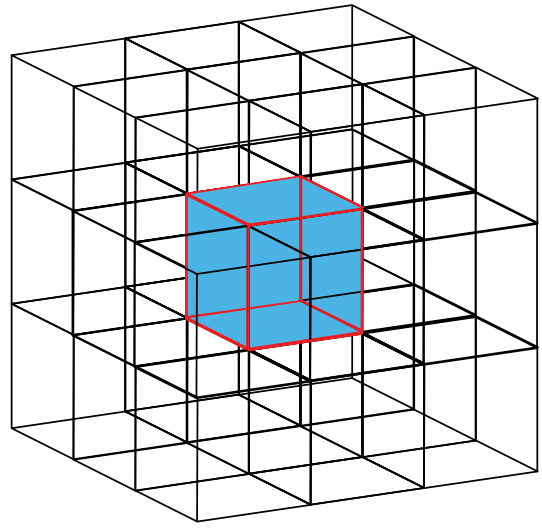

FIGURE A.1 – Created Searching lattices using uniform grid points in all directions. The cell with the red boundaries colored in blue is the one containing the particle and the other cells are its neighbors. The search for possible collision is restricted within the same cell and the 26 neighboring cells.

$$\begin{aligned} Icell(ix, iy, iz) = 1 &+ \mathrm{mod}(i_p - 1 + cellx, cellx) \\ &+ \mathrm{mod}(j_p - 1 + celly, celly) * cellx \\ &+ \mathrm{mod}(k_p - 1 + cellz, cellz) * cellx * celly \end{aligned} \tag{A.2}$$

Where i_p, j_p and k_p are the closet grid point to the particle position in stream-wise, x, span-wise, y and wall normal direction, z, respectively.

$$\begin{aligned} i_p < x_p < i_p + 1 \\ j_p < y_p < j_p + 1 \\ k_p < z_p < k_p + 1 \end{aligned}$$

Two arrays are used to control the lists; $Head(Icell)$ and $List(N_p)$. The former contains the number of first particle in that cell and the latter, the number of subsequent particles in the same cell. When the value of $List$ for a particle is zero, means this is the last particle and there is no more particle in that cell. An example of how these two arrays work is shown in in Fig. A.2 for cell number 24. In this example the way to access all the particles in a specific cell is depicted, ($Icell = 24$), via having the first particle of that cell.
In Fig. A.2, a schematic of one lattice of the searching lattices used to detect the colliding pair has been shown. The first particle or $Head$ of this cell is colored in

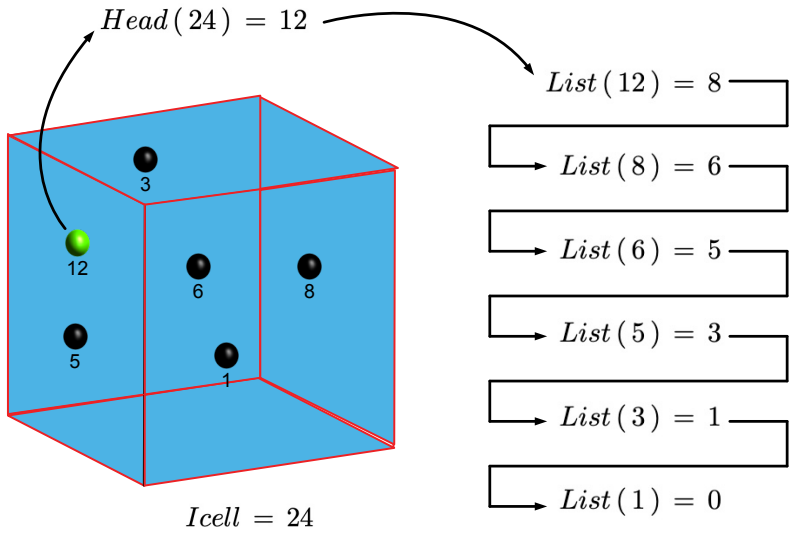

FIGURE A.2 – Schematic of access method to all the particle in a cell using the first particle or *Head* of that cell. The blue cube with red boundaries is one lattice of the uniform grid points used to detect collision in which the numbered spheres are the particles within this cell with their index. The green sphere is the first particle of the cell and the black ones are the rest of them. Particle number 1 is the last particle because its *List* value is zero.

green to which also particles 8, 6, 5, 3, 1 are belonged. The *List* value of particle number 1 is zero therefore, this is the last particle in the cell. Summing up, there are 6 particles in the in the $24th$ cell that can collide together or with the particles in the 26 neighboring cells.
If a particle is located close to the wall, the possibility of collision after bouncing at the wall must be taken into the account to avoid possible overlaps between particles. This is done by considering fictitious particles, called *mirror* particles hereinafter, placed outside of the wall boundaries. The idea of the *mirror* particles is the following; if jth particle after bouncing back to domain at $t = t_{i+1}$, overlaps with kth particle, jth and $mirror(k)$ also collide outside of the boundaries.

The mirror particle has the same x and y of the real particles, but a wall normal position equals to the value of the boundary height or minus (depending on which boundary is considered, lower or upper wall) the distance of the real particle from the boundary. The search for possible collision is extended also to these particles and taken into the account during the creation of the lists.
These are the tools to speed up the collision algorithm; When they are ready it is possible to proceed the collision. The algorithm can be divided to four steps:

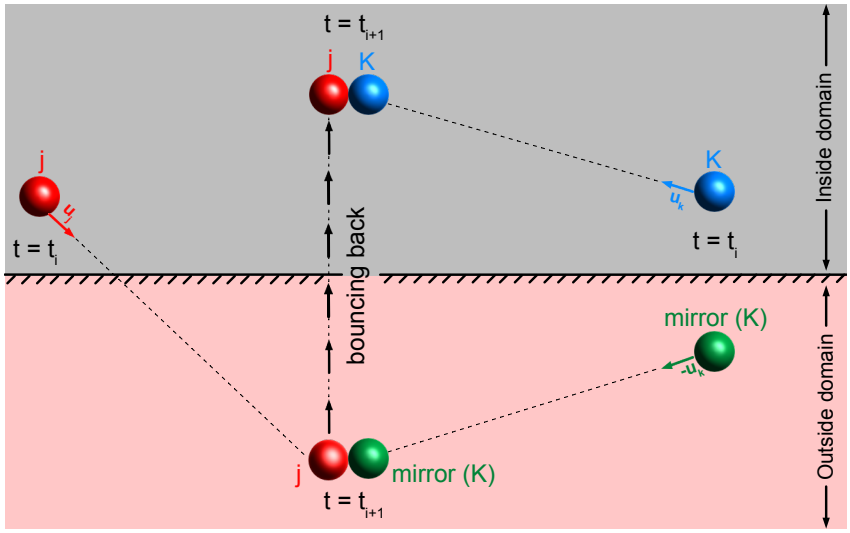

FIGURE A.3 – A schematic of using *mirror* particles to avoid possible overlaps for the particles close to the wall. The light red area is outside and the grey area is inside the domain. *jth* particle and the *kth* particle are colored in red and blue, respectively. The green spheres are the mirror of *kth* particle outside of the domain. *jth* and *kth* will overlap at $t = t_{i+1}$ if *jth* and $mirror(k)$ collide outside of the domain. As a result, to find the possible collision for the particles close to wall, the possibility of colliding between calling particle and the mirror of the other particles should be also taken into account.

1. Identify the colliding pairs that will collide within the global time step, Δt.
2. Compute the time to collision,t_{ij}, for all the pairs and the minimum time is then selected as the advancement time for all the particles.
3. Enact the elastic collision for the corresponding colliding pair.
4. Update particle position after each collision by integrating the equation of particle motion.
5. Control particle rebounds at the walls.
6. When all the collisions occurred in the order of their t_{ij} and the particles are in their final positions after the global time step Δt, Compute the net force on each to obtain particle velocity.

We also remark here that each particle maintain the same velocity during whole global time step. To compute the time to collision, t_{ij}, a formula for the distance has been used. t_{ij} equals to the time required by the particles to become separated by a distance equal to the sum of their radii or a particle diameter D_p as:

$$|r_{ij}\,(t + t_{ij})| = |r_{ij} + v_{ij} t_{ij}| = D_p \tag{A.3}$$

Where r_{ij} and t_{ij} are the relative distance and velocity between *ith* and *jth* particle. Defining b_{ij} as $r_{ij} \cdot v_{ij}$ and substitute in Eq. (A.3) we obtain

$$v_{ij}^2 t_{ij}^2 + 2b_{ij}t_{ij} + r_{ij}^2 - D_p^2 = 0$$

$$t_{ij} = \frac{-b_{ij} - \sqrt{b_{ij}^2 - v_{ij}^2(r_{ij}^2 - D_p^2)}}{v_{ij}^2} \tag{A.4}$$

If t_{ij} is a negative or complex value, the collision does not occur between particle i and j. If t_{ij} is a positive value but greater than global time step, Δt, these two particles wont collide during this time step. To sum up, the collision only when t_{ij} is positive and lower than Δt. The colliding pair with the minimum t_{ij} is the one colliding first and all the particles are advanced in time by integration the equation of particle motion with the $\min(t_{ij})$.

The post-collisional velocities of the colliding pair are calculated in the specific reference system centered in the mess center of one of the two particles. The following $\mathcal{R}$ matrix is used to transform the velocity from global coordinate system xyz to the one centered at the mass center of the particle.

$$\mathcal{R} = \begin{pmatrix} \cos\theta\cos\phi & \cos\theta\sin\phi & -\sin\theta \\ -\sin\theta & \cos\theta & 0 \\ \sin\theta\cos\phi & \sin\theta\sin\phi & \cos\theta \end{pmatrix}$$

Where ϕ and θ are the solid angles of rotation with respect to the global reference system xyz. A hard sphere model has been chosen in the present study; the main assumption of this model is that the particles can not be deformed, thus the restitution coefficient equals to 1. There are 2 main assumption behind a perfectly elastic collision; first, the total kinetic energy is the same before and after collision. Then, the total momentum remains constant thorough the collision. In other word, both momentum and kinetic energy are conserved; using this conservation, the post colliding velocity of the particles can be derived in the soldial reference system.

$$m_i v_{i1} + m_j v_{j1} = m_i v_{i2} + m_j v_{j2} \tag{A.5}$$

$$\frac{1}{2}m_i v_{i1}^2 + \frac{1}{2}m_j v_{j1}^2 = \frac{1}{2}m_i v_{i2}^2 + \frac{1}{2}m_j v_{j2}^2 \tag{A.6}$$

Where i and j refer to the two particles. The numbers 1 and 2 refer to the pre and post-colliding velocities, respectively. In the present study the particles are not allowed to change their mass ($m_i = m_j$) thus, Eq. (A.5) and Eq. (A.6) can be simplified by eliminating the masses. The obtained velocities are in the solidal reference system and they are needed to be converted back to the global reference system using the inverse of $\mathcal{R}$ matrix, $\mathcal{R}^{-1}$.

Before proceeding to the next collision, a check for possible rebounds at the wall and periodicity in x and y direction is performed. The algorithm is then repeated within the same time step until the summation of the time to collisions, t_{ij}, becomes higher than the global time step, $\sum t_{ij} > \Delta t$. At this point, there is no more collision within this time step.

B

Wall units scaling

The reference quantities for the wall units scaling system are:

$$\widetilde{\mathbf{x}} = \frac{\nu}{u_\tau}\mathbf{x}^+ , \quad \widetilde{\mathbf{u}} = u_\tau \mathbf{u}^+ , \quad \widetilde{t} = \frac{\nu}{u_\tau^2} t^+ , \quad \widetilde{\phi} = \sqrt{\frac{\beta}{\alpha}}\phi^+ , \quad \widetilde{\psi} = \psi^+ , \tag{B.1}$$

where the $\widetilde{\ }$ symbol denotes dimensional quantities, the $^+$ superscript denotes dimensionless quantities (wall units) and $\nu = \eta_c/\rho_c$ is the kinematic viscosity.
The dimensional analysis from dimensional units to outer units (no superscript) has been introduced in Sect. 2.4. From the dimensional analysis for outer and wall units, the following relations can be obtained:

$$\mathbf{x}^+ = Re_\tau \mathbf{x} , \quad \mathbf{u}^+ = \mathbf{u} , \quad t^+ = Re_\tau t , \quad \phi^+ = \phi , \quad \psi^+ = \psi . \tag{B.2}$$

In this thesis all results presented are either in outer units (no superscript), either in wall units ($^+$ superscript). Superscripts have been dropped for the velocity and the phase field as they have the same definition in both outer and wall units (superscripts, however, are kept for both time and length scales).

C

Publications and projects

C.1 Refereed journals

J1 **A. Hajisharifi**, C. Marchioli and A. Soldati. Particle capture by drops in turbulent flow. *Phys. Rev. Fluids*, **6**, Article N. 024303, 2021

J2 **A. Hajisharifi**, C. Marchioli and A. Soldati. Interface topology and evolution of particle patterns on big drops in turbulence. *J. Fluid Mech.*, (under review), 2021.

C.2 Conferences

C1 **A. Hajisharifi**†, C. Marchioli and A. Soldati, Direct Numerical Simulation of Particle-Droplet Laden Flow , *30th ERCOFTAC ADA Pilot Centre Meeting*, Vienna (Austria), November 15, 2019.

C2 **A. Hajisharifi**, C. Marchioli † and A. Soldati, Particle-droplet interaction in turbulent channel flow, *APS-DFD Annual Meeting*, Seattle (USA), November 23–26, 2019.

C3 **A. Hajisharifi**†, C. Marchioli and A. Soldati, Particle capture by drops in Turbulence , *APS-DFD Annual Meeting*, Chicago (USA), November 22–24, 2020.

C4 **A. Hajisharifi**†, C. Marchioli and A. Soldati, Turbulence-controlled evolution of particle patterns on the interface of large deformable drops , *BICTAM-CISM Symposium on Dispersed Multiphase Flows: from Measuring to Modeling*, March 2–5, 2021.

† Presentation speaker.

C.3 HPC projects

P1 **DNS of particle-droplet interaction in turbulent three phase flow (PartDrop)** (ISCRA grant), project ID: HP10CNT8LI, 300 thousands CPU

hours on Marconi Knights Landing hosted at CINECA, Casalecchio di Reno (Italy), 2019.

P2 **Direct numerical simulation of turbulent three-phase flow (TUR3PH)** (ISCRA grant), project ID: HP10B4Z9S2, 1.5 millions CPU hours on Marconi M100 hosted at CINECA, Casalecchio di Reno (Italy), 2020.

P3 **Double diffusive convective in shear-driven flow (DODICOS)** (PRACE grant), 10 millions CPU hours on TGCC Joliot Curie at CEA, Chemin du Ru, Bruyères-le-Châtel, (France), 2020.

Bibliography

[1] Wet scrubbers. `https://www.nedermanmikropul.com/en-gb/products/wet-scrubbers/mikro-vane-scrubber`. Accessed: June 12, 2021.

[2] D.M. Anderson, G.B. McFadden, and A.A. Wheeler. Diffuse interface methods in fluid mechanics. *Annu. Rev. Fluid Mech.*, 30(1):139–165, 1998.

[3] Nozomi Arai, Satoshi Watanabe, Minoru T Miyahara, Ryoichi Yamamoto, Uwe Hampel, and Gregory Lecrivain. Direct observation of the attachment behavior of hydrophobic colloidal particles onto a bubble surface. *Soft matter*, 16(3): 695–702, 2020.

[4] R. Aris. *Vectors, Tensors and the Basic Equations of Fluid Mechanics*. Dover Publications, 1989.

[5] V.E. Badalassi, H.D. Ceniceros, and S. Banerjee. Computation of multiphase systems with phase field models. *J. Comput. Phys*, 190(2):371–397, 2003.

[6] G. K. Batchelor. *An introduction to fluid dynamics*. Cambridge University Press, 1967.

[7] T. Biben and C. Misbah. Tumbling of vesicles under shear flow within an advected-field approach. *Phys. Rev. E*, 67(3):031908, 2003.

[8] Bernard P Binks. Particles as surfactants—similarities and differences. *Current opinion in colloid & interface science*, 7(1-2):21–41, 2002.

[9] H.M. Blackburn, N.N. Mansour, and B.J. Cantwell. Topology of fine-scale motions in turbulent channel flow. *J. Fluid Mech.*, 310:269–292, 1996.

[10] J.U. Brackbill, D.B. Kothe, and C. Zemach. A continuum method for modeling surface tension. *J. Comput. Phys.*, 335354, 1992.

[11] B. Bunner. Direct numerical simulations of three-dimensional bubbly flows. *Phys. Fluids*, 11(8), 1999.

[12] Bryan R Bzdek, Jonathan P Reid, Jussi Malila, and Nønne L Prisle. The surface tension of surfactant-containing, finite volume droplets. *Proceedings of the National Academy of Sciences*, 117(15):8335–8343, 2020.

[13] J.W. Cahn and J.E. Hilliard. Free Energy of a Nonuniform System. I. Interfacial Free Energy. *J. Chem. Phys.*, 28:258–267, 1958.

[14] J.W. Cahn and J.E. Hilliard. Free Energy of a Nonuniform System. II. Thermodynamic Basis. *J. Chem. Phys.*, 30(5):1121–1124, 1959.

[15] J.W. Cahn and J.E. Hilliard. Free Energy of a Nonuniform System. III. Nucleation in a Two-Component Incompressible Fluid. *J. Chem. Phys.*, 31:688, 1959.

[16] C. Canuto, M.Y. Hussaini, A.M. Quarteroni, and T.A. Zang. *Spectral Methods in Fluid Dynamics*. Springer-Verlag, 1988.

[17] Xumeng Chen and Yongjun Peng. Managing clay minerals in froth flotation—a critical review. *Mineral Processing and Extractive Metallurgy Review*, 39(5): 289–307, 2018.

[18] Kai Leong Chong, Yanshen Li, Chong Shen Ng, Roberto Verzicco, and Detlef Lohse. Convection-dominated dissolution for single and multiple immersed sessile droplets. *Journal of Fluid Mechanics*, 892, 2020.

[19] M.S. Chong, A.E. Perry, and B.J. Cantwell. A general classification of three-dimensional flow fields. *Phys. Fluids A: Fluid Dyn.*, 2:765–777, 1990.

[20] J. Cleaver and B. Yates. A sub layer model for the deposition of particles from a turbulent flow. *Chem. Eng. Sci.*, 30:983–992, 1975.

[21] Carolina Costa, Bruno Medronho, Alexandra Filipe, Isabel Mira, Björn Lindman, Håkan Edlund, and Magnus Norgren. Emulsion formation and stabilization by biomolecules: The leading role of cellulose. *Polymers*, 11(10):1570, 2019.

[22] Pedro Costa, Bendiks Jan Boersma, Jerry Westerweel, and Wim-Paul Breugem. Collision model for fully resolved simulations of flows laden with finite-size particles. *Physical Review E*, 92(5):053012, 2015.

[23] L. B. Cousins and G. F. Hewitt. Liquid phase mass transfer in annular two-phase flow. *UKAEA Report*, AERE-R 5657, 1968.

[24] Christopher Blair Crawford and Brian Quinn. *Microplastic pollutants*. Elsevier Limited, 2016.

[25] Cliff I Davidson, Robert F Phalen, and Paul A Solomon. Airborne particulate matter and human health: a review. *Aerosol Science and Technology*, 39(8): 737–749, 2005.

[26] Gary B Davies, Timm Krüger, Peter V Coveney, and Jens Harting. Detachment energies of spheroidal particles from fluid-fluid interfaces. *The Journal of chemical physics*, 141(15):154902, 2014.

[27] Robert H Davis and Alexander Z Zinchenko. Particle collection by permeable drops. *Physical Review Fluids*, 3(11):113601, 2018.

[28] S. De, J. Kuipers, E.A.J.F. Peters, and J.T. Padding. Viscoelastic flow simulations in random porous media. *J. Non-Newton. Fluid*, 248:50–61, 2017.

[29] F. De Vita, M.E. Rosti, S. Caserta, and L. Brandt. On the effect of coalescence on the rheology of emulsions. *J. Fluid Mech.*, 880:969–991, 2019.

[30] O. Desjardins, V. Moureau, and H. Pitsch. An accurate conservative level set/ghost fluid method for simulating turbulent atomization. *J. Comput. Phys.*, 227:8395–8416, 2008.

[31] F. Di Natale, C. Carotenuto, L. D'Addio, A. Jaworek, A. Krupa, M. Szudyga, and A. Lancia. Capture of fine and ultrafine particles in a wet electrostatic scrubber. *J. Environ. Chem.*, 3:349–356, 2015.

[32] M Di Renzo, PL Johnson, M Bassenne, L Villafañe, and J Urzay. Mitigation of turbophoresis in particle-laden turbulent channel flows by using incident electric fields. *Physical Review Fluids*, 4(12):124303, 2019.

[33] E. Dickinson. Food emulsions and foams: Stabilization by particles. *Curr. Opin. Colloid. Interface Sci.*, 15:40–49, 2010.

[34] Eric Dickinson. Exploring the frontiers of colloidal behaviour where polymers and particles meet. *Food Hydrocolloids*, 52:497–509, 2016.

[35] H. Ding and C. Yuan. On the diffuse interface method using a dual-resolution cartesian grid. *J. Comput. Phys.*, 273:243 – 254, 2014.

[36] H. Ding, P.D.M. Spelt, and C. Shu. Diffuse interface model for incompressible two-phase flows with large density ratios. *J. Comput. Phys.*, 226(2):2078–2095, 2007.

[37] A.D. Dinsmore, M.F. Hsu, M.G. Nikolaides, M. Marquez, A.R. Bausch, and D.A. Weitz. Colloidosomes: selectively permeable capsules composed of colloidal particles. *Science*, 298:1006–1009, 2002.

[38] M.S. Dodd and A. Ferrante. On the interaction of Taylor length scale size droplets and isotropic turbulence. *J. Fluid Mech.*, 806:356–412, 2016.

[39] M.S. Dodd and L. Jofre. Small-scale flow topologies in decaying isotropic turbulence laden with finite-size droplets. *Phys. Rev. Fluids*, 4:064303, 2019.

[40] S. Elghobashi. Direct numerical simulation of turbulent flows laden with droplets or bubbles. *Annu. Rev. Fluid Mech.*, 51:217–244, 2019.

[41] Rammile Ettelaie and Sergey V Lishchuk. Detachment force of particles from fluid droplets. *Soft Matter*, 11(21):4251–4265, 2015.

[42] S. Friedlander and H. Johnstone. Deposition of suspended particles from turbulent gas streams. *Ind. Eng. Chem.*, 49:1151–1156, 1957.

[43] M. Frigo and S.G. Johnson. The design and implementation of FFTW3. *Proceedings of the IEEE*, 93(2):216–231, 2005. Special issue on "Program Generation, Optimization, and Platform Adaptation".

[44] Masahiro Fujita, Osamu Koike, and Yukio Yamaguchi. Direct simulation of drying colloidal suspension on substrate using immersed free surface model. *Journal of Computational Physics*, 281:421–448, 2015.

[45] Ya Gao, Geoffrey M Evans, Erica J Wanless, and Roberto Moreno-Atanasio. Dem simulation of single bubble flotation: implications for the hydrophobic force in particle–bubble interactions. *Advanced Powder Technology*, 25(4):1177–1184, 2014.

[46] Ya Gao, Geoffrey M Evans, Erica J Wanless, and Roberto Moreno-Atanasio. Dem modelling of particle-bubble capture through extended dlvo theory. *Colloids and Surfaces A: Physicochemical and Engineering Aspects*, 529:876–885, 2017.

[47] Allan Gomez-Flores, Stephen Kayombo Solongo, Graeme W Heyes, Sadia Ilyas, and Hyunjung Kim. Bubble- particle interactions with hydrodynamics, xdlvo theory, and surface roughness for flotation in an agitated tank using cfd simulations. *Minerals Engineering*, 152:106368, 2020.

[48] C. Goniva, Z. Tuković, C. Feilmayr, and S. Pirker. Direct numerical simulation of turbulent flows laden with droplets or bubbles. *Prog. Comput. Fluid Dy.*, 10: 265–275, 2010.

[49] Peter Grassberger and Itamar Procaccia. Characterization of strange attractors. *Physical review letters*, 50(5):346, 1983.

[50] Chuan Gu and Lorenzo Botto. Direct calculation of anisotropic surface stresses during deformation of a particle-covered drop. *Soft matter*, 12(3):705–716, 2016.

[51] Chuan Gu and Lorenzo Botto. Fipi: A fast numerical method for the simulation of particle-laden fluid interfaces. *Computer Physics Communications*, 256: 107447, 2020.

[52] Arash Hajisharifi, Cristian Marchioli, and Alfredo Soldati. Particle capture by drops in turbulent flow. *Physical Review Fluids*, 6(2):024303, 2021.

[53] Helen Hassander, Beatrice Johansson, and Bertil Törnell. The mechanism of emulsion stabilization by small silica (ludox) particles. *Colloids and surfaces*, 40:93–105, 1989.

[54] C.W. Hirt and B.D. Nichols. Volume of fluid (VOF) method for the dynamics of free boundaries. *J. Comput. Phys.*, 39(1):201–225, 1981.

[55] RTWDW Hogg, To Wo Healy, and Douglas W Fuerstenau. Mutual coagulation of colloidal dispersions. *Transactions of the Faraday Society*, 62:1638–1651, 1966.

[56] Tommy S Horozov and Bernard P Binks. Particle-stabilized emulsions: a bilayer or a bridging monolayer? *Angewandte Chemie*, 118(5):787–790, 2006.

[57] Robert J Hunter. *Foundations of colloid science*. Oxford university press, 2001.

[58] M.Y. Hussaini and T.A. Zang. Spectral methods in fluid dynamics. *Annu. Rev. Fluid Mech.*, 19(1):339–367, 1987.

[59] Gianluca Iaccarino and Roberto Verzicco. Immersed boundary technique for turbulent flow simulations. *Appl. Mech. Rev.*, 56(3):331–347, 2003.

[60] D. Jacqmin. Calculation of two-phase Navier–Stokes flows using phase-field modeling. *J. Comput. Phys.*, 155(1):96–127, 1999.

[61] D. Jamet, D. Torres, and J.U. Brackbill. On the theory and computation of surface tension: the elimination of parasitic currents through energy conservation in the second-gradient method. *J. Comput. Phys.*, 182(1):262–276, 2002.

[62] JF Joanny and Pierre-Gilles De Gennes. A model for contact angle hysteresis. *The journal of chemical physics*, 81(1):552–562, 1984.

[63] H.T. Kim. Particle removal efficiency of gravitational wet scrubber considering diffusion, interception and impaction. *Environ. Eng. Sci.*, 18:125–136, 2001.

[64] H.T. Kim, C.H. Jung, S.N. Oh, and K.W. Lee. Particle removal efficiency of gravitational wet scrubber considering diffusion, interception, and impaction. *Environ. Eng. Sci.*, 18:125–136, 2001.

[65] J. Kim. A continuous surface tension force formulation for diffuse-interface models. *J. Comput. Phys*, 204(2):784–804, 2005.

[66] J. Kim. A generalized continuous surface tension force formulation for phase-field models for multi-component immiscible fluid fows. *Comput. Method Appl. M.*, 189:3105–3112, 2009.

[67] J. Kim. Phase-Field Models for Multi-Component Fluid Flows. *Commun. Comput. Phys.*, 12(3):613–661, 2012.

[68] J. Kim and J. Lowengrub. Phase field modeling and simulation of three-phase flows. *Interfaces and free boundaries*, 7(4):435, 2005.

[69] Yongsam Kim and Charles S Peskin. Numerical study of incompressible fluid dynamics with nonuniform density by the immersed boundary method. *Physics of Fluids*, 20(6):062101, 2008.

[70] D.J. Korteweg. Sur la forme que prennent les equations du mouvements des fluides si l'on tient compte des forces capillaires causées par des variations de densité considérables mais continues et sur la théorie de la capillarité dans l'hypothèse d'une variation continue de la densité. *Archives Néerlandaises des Sciences Exactes et Naturelles*, 6:1–24, 1901.

[71] Bengt Kronberg and B Lindman. *Surfactants and polymers in aqueous solution*. John Wiley & Sons Ltd., Chichester, 2003.

[72] Bengt Kronberg, Krister Holmberg, and Bjorn Lindman. *Surface chemistry of surfactants and polymers*. John Wiley & Sons, 2014.

[73] Johannes GM Kuerten and AW Vreman. Effect of droplet interaction on droplet-laden turbulent channel flow. *Physics of fluids*, 27(5):053304, 2015.

[74] Jason Larkin, MM Bandi, Alain Pumir, and Walter I Goldburg. Power-law distributions of particle concentration in free-surface flows. *Physical Review E*, 80(6):066301, 2009.

[75] Jason Larkin, Walter Goldburg, and MM Bandi. Time evolution of a fractal distribution: Particle concentrations in free-surface turbulence. *Physica D: Nonlinear Phenomena*, 239(14):1264–1268, 2010.

[76] L G Lealz. The effects of surfactants on drop deformation and breakup. 1990.

[77] G. Lecrivain, R. Yamamoto, U. Hampel, and T. Taniguchi. Direct numerical simulation of a particle attachment to an immersed bubble. *Phys. Fluids*, 28: 083301, 2016.

[78] Q. Li, M. Abbas, and J. F. Morris. Particle approach to a stagnation point at a wall: Viscous damping and collision dynamics. *Phys. Rev. Fluids*, 5:104301, 2020.

[79] Y. Li, J. Choi, and J. Kim. A phase-field fluid modeling and computation with interfacial profile correction term. *Commun. Nonlinear Sci.*, 30(1-3):84–100, 2016.

[80] Haihu Liu, Jinggang Zhang, Yan Ba, Ningning Wang, and Lei Wu. Modelling a surfactant-covered droplet on a solid surface in three-dimensional shear flow. *Journal of Fluid Mechanics*, 897, 2020.

[81] Zhengwei Long and Qiang Yao. Evaluation of various particle charging models for simulating particle dynamics in electrostatic precipitators. *Journal of Aerosol science*, 41(7):702–718, 2010.

[82] Salvatore Lovecchio, Cristian Marchioli, and Alfredo Soldati. Time persistence of floating-particle clusters in free-surface turbulence. *Physical Review E*, 88(3): 033003, 2013.

[83] F. Magaletti, F. Picano, M. Chinappi, L. Marino, and C.M. Casciola. The sharp-interface limit of the Cahn–Hilliard/Navier–Stokes model for binary fluids. *J. Fluid Mech.*, 714:95–126, 2013.

[84] F. Magaletti, F. Picano, M. Chinappi, L. Marino, and C.M. Casciola. The sharp-interface limit of the cahn-hilliard/navier-stokes model for binary fluids. *J. Fluid Mech.*, 714:95, 2013.

[85] Harishankar Manikantan and Todd M Squires. Surfactant dynamics: hidden variables controlling fluid flows. *Journal of Fluid Mechanics*, 892, 2020.

[86] Ch Marchioli, A Soldati, JGM Kuerten, B Arcen, A Taniere, G Goldensoph, KD Squires, MF Cargnelutti, and LM Portela. Statistics of particle dispersion in direct numerical simulations of wall-bounded turbulence: Results of an international collaborative benchmark test. *International Journal of Multiphase Flow*, 34(9):879–893, 2008.

[87] Cristian Marchioli, H Bhatia, G Sardina, Luca Brandt, and A Soldati. Role of large-scale advection and small-scale turbulence on vertical migration of gyrotactic swimmers. *Physical Review Fluids*, 4(12):124304, 2019.

[88] Gisela Ablas Marques and Jorge Alberto Soares Tenório. Use of froth flotation to separate pvc/pet mixtures. *Waste Management*, 20(4):265–269, 2000.

[89] Harting J. Mehrabian, H. and J.H. Snoeijer. Soft particles at a fluid interface. *Soft Matter*, 12:1062–1073, 2016.

[90] B.C. Meikap, G. Kundu, and M.N. Biswas. Scrubbing of fly-ash laden so2 in modified multistage bubble column scrubber. *AIChE J.*, 48:2074–2083, 2002.

[91] T. Menard, S. Tanguy, and A. Berlemont. Coupling level set / VOF / ghost fluid methods : Validation and application to 3D simulation of the primary break-up of a liquid jet. *Int. J. Multiphas. Flow*, 33:510–524, 2007.

[92] Rajat Mittal and Gianluca Iaccarino. Immersed boundary methods. *Annu. Rev. Fluid Mech.*, 37:239–261, 2005.

[93] AV Nguyen and GM Evans. Attachment interaction between air bubbles and particles in froth flotation. *Experimental Thermal and Fluid Science*, 28(5): 381–385, 2004.

[94] CW Nutt. Froth flotation: The adhesion of solid particles to flat interfaces and bubbles. *Chemical Engineering Science*, 12(2):133–141, 1960.

[95] S. Osher and J. Sethian. Fronts Propagating with Curvature-Dependent Speed: Algorithms Based on Hamilton-Jacobi Formulations. *J. Comput. Phys.*, 49:12–49, 1988.

[96] S. Osher and J. Sethian. A Level Set Approach for computing solutions to incompressible Two-Phase Flow. *J. Comput. Phys.*, 114:12–49, 1994.

[97] B.J. Park and D. Lee. Particles at fluid-fluid interfaces: From single-particle behavior to hierarchical assembly of materials. *MRS Bulletin*, 39:1089, 2014.

[98] A.E. Perry and M.S. Chong. A description of eddying motions and flow patterns using critical-point concepts. *Annu. Rev. Fluid Mech.*, 19:125–155, 1987.

[99] Charles S Peskin. Flow patterns around heart valves: a digital computer method for solving the equations of motion. *IEEE Transactions on Biomedical Engineering*, (4):316–317, 1973.

[100] W. Peukert and C. Wadenpohl. Industrial separation of fine particles with difficult dust properties. *Powder Technol.*, 118:136–148, 2001.

[101] R. Peyret. *Spectral Methods for Incompressible Viscous Flow*, volume 148. Springer Science+Business Media, 2002.

[102] Francesco Picano, Wim-Paul Breugem, and Luca Brandt. Turbulent channel flow of dense suspensions of neutrally buoyant spheres. *Journal of Fluid Mechanics*, 764:463–487, 2015.

[103] M. Picciotto, C. Marchioli, and A. Soldati. Characterization of near-wall accumulation regions for inertial particles in turbulent boundary layers. *Phys. Fluids*, 17:098101, 2005.

[104] Stéphane Popinet. Numerical models of surface tension. *Annu. Rev. Fluid Mech.*, 50:1–28, 2018.

[105] G. Pozzetti and B. Peters. A multiscale dem-vof method for the simulation of three-phase flows. *Int. J. Multiphase Flow*, 99:186–204, 2018.

[106] A. Prosperetti and G. Tryggvason. *Computational Methods for Multiphase Flow*. Cambridge Press, 2009.

[107] N. Rafidi, F. Brogaard, L. Chen, R. Håkansson, and A. Tabikh. Cfd and experimental studies on capture of fine particles by liquid droplets in open spray towers. *Sustain. Environ. Res.*, 28:382–388, 2018.

[108] W.J. Rider and D.B. Kothe. Reconstructing volume tracking. *J. Comput. Phys.*, 141(2):112–152, 1998.

[109] A. Roccon, M. De Paoli, F. Zonta, and A. Soldati. Viscosity-modulated breakup and coalescence of large drops in bounded turbulence. *Phys. Rev. Fluids*, 2: 083603, 2017.

[110] A. Roccon, M. De Paoli, F. Zonta, and A. Soldati. Viscosity-modulated breakup and coalescence of large drops in bounded turbulence. *Phys. Rev. Fluids*, 2: 083603, 2017.

[111] M.E. Rosti, F. De Vita, and L. Brandt. Numerical simulations of emulsions in shear flows. *Acta Mech.*, 230:667–682, 2019.

[112] Gesse A Roure and Robert H Davis. Modelling of particle capture by expanding droplets. *Journal of Fluid Mechanics*, 912, 2021.

[113] JL Salager, A Forgiarini, and J Bullón. Progress in designing emulsion properties over a century: Emerging phenomenological guidelines from generalized formulation and prospects to transmute the knowledge into know-how. *Surfactant Science and Technology: Retrospects and Prospects; Romsted, LS, Ed*, pages 459–487, 2014.

[114] G Sardina, Philipp Schlatter, Luca Brandt, F Picano, and Carlo Massimo Casciola. Wall accumulation and spatial localization in particle-laden wall flows. *Journal of Fluid Mechanics*, 699(1):50–78, 2012.

[115] L. Scarbolo and A. Soldati. Turbulence modulation across the interface of a large deformable drop. *J. Turbul.*, 14:27–43, 2013.

[116] L. Schiller and A. Naumann. A drag coefficient correlation. *Zeit. Ver. Deutsch. Ing.*, 77:318–320, 1933.

[117] Laurier L Schramm. *Emulsions, foams, and suspensions: fundamentals and applications*. John Wiley & Sons, 2006.

[118] Hiroyuki Shinto. Computer simulation of wetting, capillary forces, and particle-stabilized emulsions: From molecular-scale to mesoscale modeling. *Advanced Powder Technology*, 23(5):538–547, 2012.

[119] P Singh and DD Joseph. Fluid dynamics of floating particles. *Journal of Fluid Mechanics*, 530:31, 2005.

[120] A. Soldati and P. Andreussi. The influence of coalescence on droplet transfer in vertical annular flow. *Chem. Eng. Sci.*, 51:353–363, 1996.

[121] A. Soldati and S. Banerjee. Turbulence modification by large-scale organized electrohydrodynamic flows. *Phys. Fluids*, 10(7):1742–1756, 1998.

[122] A. Soldati and C. Marchioli. Physics and modelling of turbulent particle deposition and entrainment: Review of a systematic study. *Int. J. Multiphase Flow*, 35:827–839, 2009.

[123] Alfredo Soldati and Cristian Marchioli. Physics and modelling of turbulent particle deposition and entrainment: Review of a systematic study. *International Journal of Multiphase Flow*, 35(9):827–839, 2009.

[124] G. Soligo, A. Roccon, and A. Soldati. Mass-conservation-improved Phase Field Methods for turbulent multiphase flow simulation. *Acta Mech.*, 230(2):683–696, 2019.

[125] G. Soligo, A. Roccon, and A. Soldati. Coalescence of surfactant-laden drops by phase field method. *J. Comput. Phys.*, 376:1292–1311, 2019.

[126] G. Soligo, A. Roccon, and A. Soldati. Mass-conservation-improved phase field methods for turbulent multiphase flow simulation. *Acta Mech.*, 230:683–696, 2019.

[127] G. Soligo, A. Roccon, and A. Soldati. Effect of surfactant-laden droplets on turbulent flow topology. *Phys. Rev. Fluids*, 5:073606, 2020.

[128] Giovanni Soligo, Alessio Roccon, and Alfredo Soldati. Breakage, coalescence and size distribution of surfactant-laden droplets in turbulent flow. *Journal of Fluid Mechanics*, 881:244–282, 2019.

[129] Vamsi Spandan, Valentina Meschini, Rodolfo Ostilla-Mónico, Detlef Lohse, Giorgio Querzoli, Marco D de Tullio, and Roberto Verzicco. A parallel interaction potential approach coupled with the immersed boundary method for fully resolved simulations of deformable interfaces and membranes. *Journal of computational physics*, 348:567–590, 2017.

[130] Vamsi Spandan, Detlef Lohse, Marco D de Tullio, and Roberto Verzicco. A fast moving least squares approximation with adaptive lagrangian mesh refinement for large scale immersed boundary simulations. *Journal of computational physics*, 375:228–239, 2018.

[131] K. Stratford, R. Adhikari, I. Pagonabarraga, J.C. Desplat, and M.E. Cates. Colloidal jamming at interfaces: A route to fluid-bicontinuous gels. *Science*, 309:2198–2201, 2005.

[132] L. Su, Y. Zhang, Q. Du, X. Dai, J. Gao, P. Dong, and H. Wang. An experimental study on the removal of submicron fly ash and black carbon in a gravitational wet scrubber with electrostatic enhancement. *RSC Advances*, 10:5905–5912, 2020.

[133] Andrew P Sullivan and Peter K Kilpatrick. The effects of inorganic solid particles on water and crude oil emulsion stability. *Industrial & engineering chemistry research*, 41(14):3389–3404, 2002.

[134] Xiaosong Sun and Mikio Sakai. Three-dimensional simulation of gas–solid–liquid flows using the dem–vof method. *Chemical Engineering Science*, 134:531–548, 2015.

[135] Y. Sun and C. Beckermann. Sharp interface tracking using the phase-field equation. *J. Comput. Phys.*, 220(2):626–653, 2007.

[136] Shivshankar Sundaram and Lance R Collins. Numerical considerations in simulating a turbulent suspension of finite-volume particles. *Journal of Computational Physics*, 124(2):337–350, 1996.

[137] Shivshankar Sundaram and Lance R Collins. Collision statistics in an isotropic particle-laden turbulent suspension. part 1. direct numerical simulations. *Journal of Fluid Mechanics*, 335:75–109, 1997.

[138] Tharwat Tadros. *Encyclopedia of Colloid and Interface Science.* Springer, 2013.

[139] P. Than, L. Preziosi, D. Josephl, and M. Arney. Measurement of interfacial tension between immiscible liquids with the spinning road tensiometer. *J. Colloid Interface Sci.*, 124(2):552–559, 1988.

[140] G. Tryggvason, B. Bunner, A. Esmaeeli, D. Juric, W. Tauber, J. Han, S. Nas, and Y. Jan. A front-tracking method for the computations of multiphase flow. *J. Comput. Phys.*, 759:708–759, 2001.

[141] S. Unverdi and G. Trygvasson. A Front-Tracking Method for Viscous , Incompressible , Multi-fluid Flows. *J. Comput. Phys.*, 100(1), 1992.

[142] Ao Wang, Qiang Song, and Qiang Yao. Study on inertial capture of particles by a droplet in a wide reynolds number range. *Journal of Aerosol Science*, 93: 1–15, 2016.

[143] Guichao Wang, Anh V Nguyen, Subhasish Mitra, JB Joshi, Graeme J Jameson, and Geoffrey M Evans. A review of the mechanisms and models of bubble-particle detachment in froth flotation. *Separation and Purification Technology*, 170:155–172, 2016.

[144] H Wang and PR Brito-Parada. The role of microparticles on the shape and surface tension of static bubbles. *Journal of Colloid and Interface Science*, 587: 14–23, 2021.

[145] Lian-Ping Wang, Anthony S Wexler, and Yong Zhou. Statistical mechanical description and modelling of turbulent collision of inertial particles. *Journal of Fluid Mechanics*, 415:117–153, 2000.

[146] Zhen Wang and Yapei Wang. Tuning amphiphilicity of particles for controllable pickering emulsion. *Materials*, 9(11):903, 2016.

[147] Charles Ernest Weatherburn. *Differential geometry of three dimensions*, volume 1. Cambridge University Press, 2016.

[148] D.L. Youngs. Time-dependent multi-material flow with large fluid distortion. *Numerical Methods for Fluid Dynamics*, pages 273–285, 1982.

[149] P. Yue, J.J. Feng, C. Liu, and J. Shen. A diffuse-interface method for simulating two-phase flows of complex fluids. *J. Fluid Mech.*, 515(1):293–317, 2004.

[150] P. Yue, C. Zhou, and J.J. Feng. Spontaneous shrinkage of drops and mass conservation in phase-field simulations. *J. Comput. Phys.*, 223(1):1–9, 2007.

[151] P. Yue, C. Zhou, and J.J. Feng. Sharp-interface limit of the Cahn–Hilliard model for moving contact lines. *J. Fluid Mech.*, 645(8):279, 2010.

[152] W Zhang, R Honaker, and J Groppo. Concentration of rare earth minerals from coal by froth flotation. *Minerals & Metallurgical Processing*, 34(3):132–137, 2017.

[153] Y. Zhang and W. Ye. A Flux-Corrected Phase-Field Method for Surface Diffusion. *Commun. Comput. Phys.*, 22(2):422–440, 2017.

[154] Y. Zhang and W. Ye. A flux-corrected phase-field method for surface diffusion. *Commun. Comput. Phys.*, 22:422–440, 2017.

[155] L. Zhao, M.C. Boufadel, J. Katz, G. Haspel, K. Lee, T. King, and B. Robinson. A new mechanism of sediment attachment to oil in turbulent flows: Projectile particles. *Env. Sci. Tech.*, 51:11020–11028, 2017.

[156] Yong Zhu, Mengxiang Gao, Mingxia Chen, Jianwei Shi, and Wenfeng Shangguan. Numerical simulation of capture process of fine particles in electrostatic precipitators under consideration of electrohydrodynamics flow. *Powder Technology*, 354:653–675, 2019.